FINITE ELEMENT MODELLING OF TBC FAILURE MECHANISMS BY USING EXTENDED FINITE ELEMENT METHOD AND COHESIVE ZONE METHOD

A THESIS SUBMITTED TO
THE GRADUATE SCHOOL OF NATURAL AND APPLIED SCIENCES
OF
MIDDLE EAST TECHNICAL UNIVERSITY

BY

SAFA MESUT BOSTANCI

IN PARTIAL FULFILLMENT OF THE REQUIREMENTS
FOR
THE DEGREE OF MASTER OF SCIENCE
IN
AEROSPACE ENGINEERING, METU

DECEMBER 2019

Approval of the thesis:

FINITE ELEMENT MODELLING OF TBC FAILURE MECHANISMS BY USING EXTENDED FINITE ELEMENT METHOD AND COHESIVE ZONE METHOD

submitted by **SAFA MESUT BOSTANCI** in partial fulfillment of the requirements for the degree of **Master of Science in Aerospace Engineering, METU Department, Middle East Technical University** by,

Prof. Dr. Halil Kalıpçılar
Dean, Graduate School of **Natural and Applied Sciences** ______________

Prof. Dr. İsmail H. Tuncer
Head of Department, **Aerospace Engineering, METU** ______________

Assoc. Prof. Dr. Ercan Gürses
Supervisor, **Aerospace Engineering, METU** ______________

Examining Committee Members:

Prof. Dr. Altan Kayran
Aerospace Engineering, METU ______________

Assoc. Prof. Dr. Ercan Gürses
Aerospace Engineering, METU ______________

Assoc. Prof. Dr. Demirkan Çöker
Aerospace Engineering, METU ______________

Assist. Prof. Dr. Tuncay Yalçınkaya
Aerospace Engineering, METU ______________

Assoc. Prof. Dr. Cihan Tekoğlu
Mechanical Engineering, TOBB ______________

Date:

I hereby declare that all information in this document has been obtained and presented in accordance with academic rules and ethical conduct. I also declare that, as required by these rules and conduct, I have fully cited and referenced all material and results that are not original to this work.

Name, Surname: Safa Mesut Bostancı

Signature :

ABSTRACT

FINITE ELEMENT MODELLING OF TBC FAILURE MECHANISMS BY USING EXTENDED FINITE ELEMENT METHOD AND COHESIVE ZONE METHOD

Bostancı, Safa Mesut
M.S., Department of Aerospace Engineering, METU
Supervisor: Assoc. Prof. Dr. Ercan Gürses

DECEMBER 2019, 96 pages

Thermal Barrier Coatings have been widely used in modern turbine engines to protect the nickel based metal substrate from the high temperature service conditions, 1600-1800 K. In this study, failure mechanisms of typical Air Plasma Sprayed Thermal Barrier Coatings (TBC) used in after-burner structures composed of three major layers: Inconel 718 substrate, NiCrAlY based metallic bond coat (BC) and Yttria Stabilized Zirconia (YSZ) based ceramic top coat (TC) are investigated. Investigation of the cracking mechanism of TBC in terms of design and performance is very important because the behavior of TBCs on ductile metallic substrates is brittle. To this end, four-point bending experiments reported in [1] are analyzed by using the Extended Finite Element Method (XFEM) and the Cohesive Zone Method (CZM). All the analyses are conducted with the commercial finite element software ABAQUS. Three different models with varying TC and BC thicknesses are studied. It is observed that multiple vertical cracks are initiated in the TC. Cracks initiate at the top of YSZ and propagate through the whole TC until they reach the interface between the TC and the BC. Then, delaminations at the interface between the TC and the BC start.

It is observed that the average spacing of cracks in TC increases with the increasing thickness of the TC and the delamination becomes prominent with the increasing TC thickness. Numerical results are found to be consistent with the experimental [1] results.

Keywords: thermal barrier coatings, extended finite element method, cohesive zone method, fracture mechanics

ÖZ

ISIL BARİYER KAPLAMALARDAKİ GÖÇME MEKANİZMALARININ GENİŞLETİLMİŞ SONLU ELEMANLAR YÖNTEMİ VE YAPIŞKAN ALAN METODU İLE MODELLENMESİ

Bostancı, Safa Mesut
Yüksek Lisans, Havacılık ve Uzay Mühendisliği, ODTÜ Bölümü
Tez Yöneticisi: Doç. Dr. Ercan Gürses

Aralık 2019 , 96 sayfa

Termal bariyer kaplamalar(TBK), nikel bazlı metal alt tabakayı 1600-1800 K mertebesindeki yüksek sıcaklık servis koşullarından korumak için modern türbin motorlarında yaygın olarak kullanılmaktadır. Bu çalışmada, Inconel 718 alt tabaka, NiCrAlY bazlı metalik yapıştırıcı ara kaplama ve Yttria Stabilize Zirkonya (YSZ) bazlı seramik üst kaplama ile birlikte üç ana katmandan oluşan brülör sonrası yapılarda kullanılan tipik Hava Plazma Püskürtmeli Termal Bariyer Kaplamalarının (TBK) kırılma mekanizması incelenmiştir. TBK'lar sünek metalik alt tabakalar üzerinde kırılgan bir davranış gösterdiklerinden dolayı tasarım ve performans açısından kırılma mekanizmalarının incelenmesi oldukça önemlidir. Bu amaçla, literatürde yer alan [1] dört-nokta bükme deneyleri genişletilmiş sonlu elemanlar yöntemi ve yapışkan alan metodu kullanılarak analiz edilmiştir. Tüm analizler ticari sonlu elemanlar yazılımı ABAQUS ile gerçekleştirilmiştir. Üst ve yapışkan kaplama kalınlıklarının değiştiği üç farklı model incelenmiştir. Analizler sonucunda, üst kaplamada çoklu dikey kırıkların başladığı görülmüştür. Çatlaklar YSZ'nin en üst kısmında başlamakta ve YSZ

ile ara tabaka arasındaki arayüze ulaşana kadar tüm üst tabaka boyunca ilerlemektedir. Kırıklar üst tabaka ile yapıştırıcı tabaka arasında yer alan arayüze ulaştığında, bu arayüzde delaminasyonlar başlamaktadır. Yapılan çalışmada deney sonuçlarındaki [1] gibi, artan üst tabaka kalınlığı ile ortalama kırıklar arası mesafenin azaldığı ve üst tabaka ile ara tabaka arasında gerçekleşen delaminasyonun daha belirgin olduğu gözlemlenmiştir. Başka bir deyişle; nümerik sonuçların deneysel sonuçlarla [1] tutarlı olduğu görülmüştür.

Anahtar Kelimeler: termal bariyer kaplamalar, genişletilmiş sonlu elemanlar yöntemi, yapışkan alan metodu, kırık mekaniği

to my family and friends

ACKNOWLEDGMENTS

First of all, my deepest gratitude goes to my supervisor Assoc. Prof. Dr. Ercan Gürses for his continuous support, motivation, interesting cues, guidance, enthusiasm, patience, wisdom and for giving me the possibility to work with him. I could not complete my thesis successfully without his guidance and support.

I would also like to present my truthful thanks to Assoc. Prof. Dr. Demirkan Çöker for his advices and contributions to this study.

This study has been a long journey with a lot of uncertainties and opportunities for me to advance my knowledge. I can't thank enough to all my friends for making this journey bearable. Starting with my dearest friend Ahmet Arda Akay, he was always there for me whenever I needed help ever since the day I met with him and he did not withhold his support during my graduate study as well.

I would also like to acknowledge my dear friends, Can Baloğlu, Ozan Güler, Anıl Alan, Emre Yılmaz, Talha Köse, Bahadır Yılmazer, Utku Göreke. I am very fortunate to have their friendships.

I also appreciate all my colleagues and managers in ASELSAN A.Ş. for providing a comfortable and supporting work environment.

I wish to thank to my parents, Nesrin Bostancı and İbrahim Bostancı, for all the opportunities they provided me throughout my life. Nothing would be possible without them on my back.

Last but not least, I thank to Esra for being the greatest sister ever and her unlimited support, patience and advices.

TABLE OF CONTENTS

LIST OF TABLES

TABLES

LIST OF FIGURES

FIGURES

LIST OF ABBREVIATIONS

2D	2 Dimensional
3D	3 Dimensional
TC	Top Coat
BC	Bond Coat
TBC	Thermal Barrier Coating
YSZ	Yttria Stabilized Zirconia
TGO	Thermally Grown Oxide
APS	Air Plasma Spraying
EB-PVD	Electron Beam Vapor Deposition
XFEM	Extended Finite Element Method
CZM	Cohesive Zone Model
MAXPS	Maximum Principal Stress
MAXS	Maximum Nominal Stress

CHAPTER 1

INTRODUCTION

In this chapter aero jet engines and their working principle are briefly explained and the main motivation of using thermal barrier coatings (TBCs) in the jet engine parts is given. The typical TBC system, the materials used in the TBC layers and the historical evolution of them are presented. The deposition techniques of the TBCs are also explained and the main failure sources depending on the deposition technique from the literature are summarized. At the end of the chapter, a literature review about numerical studies of the TBC failure are presented and the scope of this study is given.

1.1 Thermal Barrier Coatings (TBCs)

From past to present, in recent decades, studies have been trying to find answers in order to increase the efficiency of the hot section components, such as vanes and blades, of an advanced turbine or an engine in modern aerospace applications. At this point, thermal barrier coating systems (TBCs) are now of a great interest for many researchers since these coatings under optimum conditions enable all kinds of components to operate even at higher gas temperatures [18]. Besides, TBCs also improve the lifetime of the parts and they prevent the hot corrosion failures during operation [8].

As can be seen from Figure 1.1, an engine basically works with a fan at the front through sucking the air. Then, the pressure of the air increases with the help of a compressor made by many blades attached to a shaft. When blades spin at considerably high speeds, they squeeze the air and then the compressed air is sprayed with the fuel and an electric spark light. The burnt gasses expand and spark through the noz-

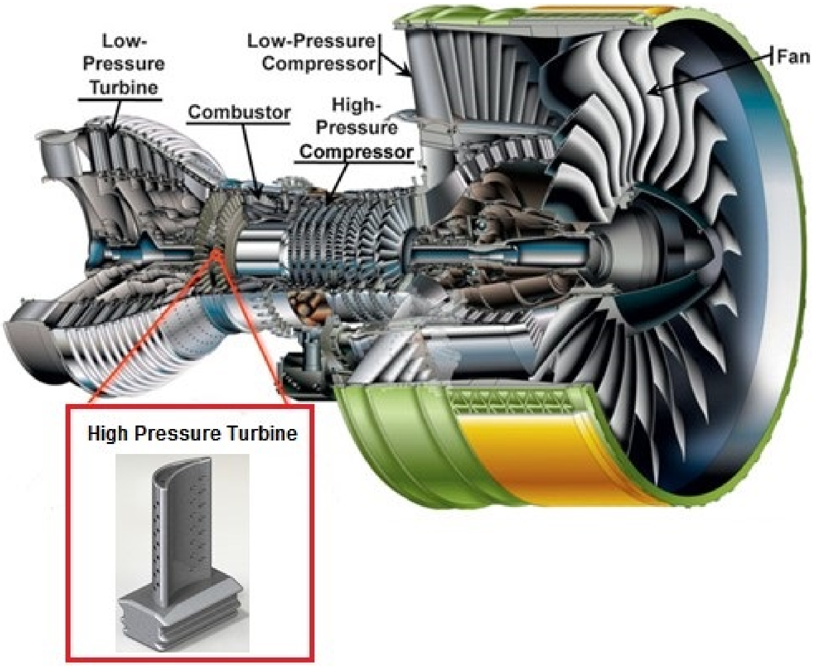

Figure 1.1: Representation of an Engine Alliance GP7200 aircraft engine [2]

zle at the back of the engine. This results in a momentum where jets of gas shooting backward on the reverse side of the engine and creates a thrust force which pushes the aircraft forward. During the travel of the hot air going through the nozzle, it also passes through the blades, in other words turbine which is attached to the same compressor. Therefore, fuel-to-power efficiency is strongly related with the temperature level at which the engine operates, meaning higher temperatures generally mean higher efficiencies. A typical engine can reach temperature levels around 1260°C. However, the metal parts in the engine can only withstand temperatures around 815°C to 927°C. Therefore, in such conditions metallic parts become rubbery and failures are expected to occur. It is now known that introduction of TBCs on that high pressure and high temperature sections of the engine can help to protect the metallic parts, hence high temperatures can be reached and the efficiency can be increased. Due to this reason, up to a certain point, at lower operating temperatures TBC application reduces the temperature of the metal part and therefore, the engine component becomes more durable. Based on this, fuel economy and cleaner exhaust gases can also be obtained according to the developing investigations [3]. Therefore, coming to 1950s and starting from this date, TBCs laid the foundation as the very first ceramic coatings [2]. The first ceramic coatings for the aviation industry and hence aerospace applications were frit enamels that were developed by the National Advisory Committee for Aeronautics (NACA) in cooperation with National Bureu of Standards (NBS) [19, 20]. After 10 years from this date, first flame sprayed ceramic coatings that have NiAl as a bond coat were used for commercial aero engines [21]. During this period of time zirconia-calcia was also found to be an effective ceramic coating for such thermal barrier applications [19]. Then by, in 1980s the importance of TBC systems significantly increased and during this decade, standard interest turned into yttria stabilized zirconia (YSZ) as a topcoat metarial for TBCs [21, 22]. When a 100 to 150 μm thickness TBC applied together with the internal cooling of the underlying superalloy component, the surface temperature of the substrate superalloy can be reduced around 100-300°C which also provides a great efficiency of performance for a jet engine as mentioned previously. TBCs, must ensure to maintain thermal protection for prolonged thermal cycles and also service times without any failure [2]. Hence, the lifetime and the firing temperature of the engine or turbine increases resulting with the increase in efficiency [21]. Figure 1.2 presents the increasing efficiency by the use of TBCs extending to years and proves an improvement by developing advanced superalloys.

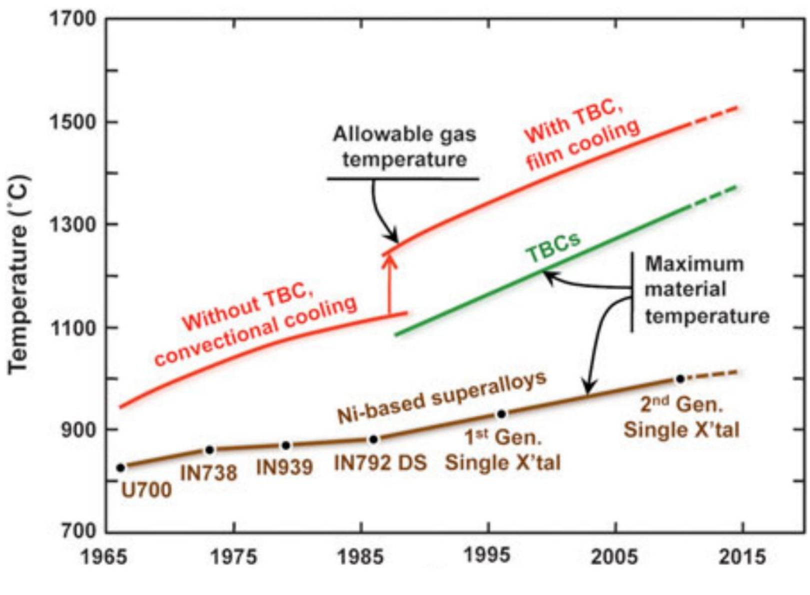

Figure 1.2: Improvement of the capabilities of superalloys by using TBCs depending extending to years [2]

Further investigations additionally proved that for cooling the parts in the interior regions, the heat transfer through the TBC must be kept as low as possible. According to the studies of several research groups [23, 7] it was found possible to obtain a temperature drop around 170°C between the topcoat and the substrate with around 300 μm YSZ topcoat. Therefore, basically the heat insulation can be utilized by applying TBCs for the metallic engine parts [24, 25]. Schematically, the process can be represented in Figure 1.3 which will be mentioned later in detail.

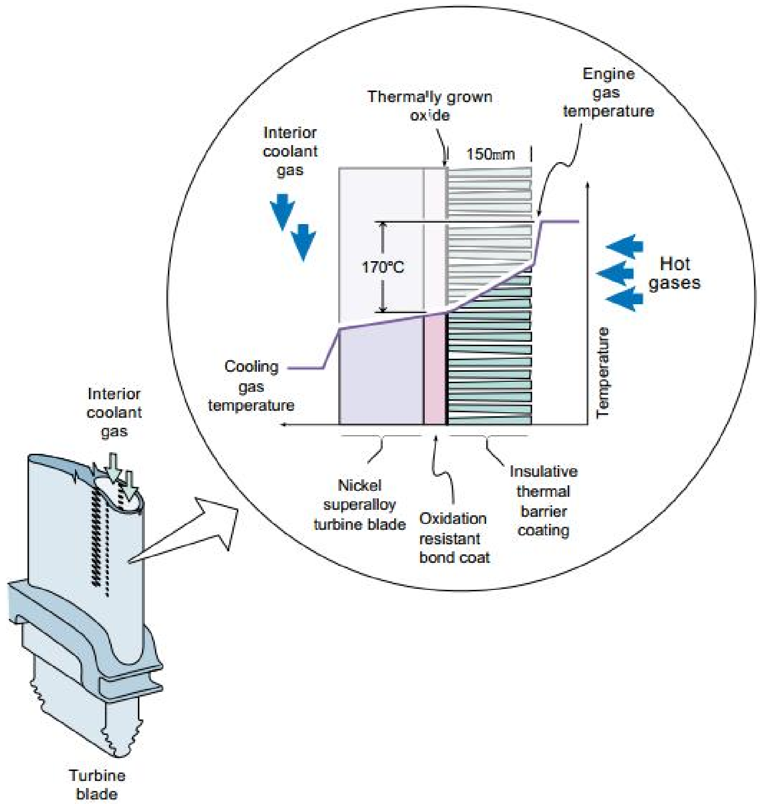

Figure 1.3: Conventional methods in order to produce TBC system [3]

As shown in Figure 1.3, TBCs, basically, are ceramic coating materials [26] that are mostly a duplex-type consisting of a metallic bond coat (BC) and a ceramic topcoat (TC) [21]. The first application of TBCs were the rotating blades and today they are still the most critical component. Even though the failure of the TBCs, depending on coupled interaction of mechanical property difference and the diffusional effects between the top coat and the superalloy, can hazard the substrate material, TBCs are still evolving and their use is vital [2].

In order to imagine the structrure of TBCs, a schematic representation is given in

Figure 1.4 with the thermally grown oxide layer (TGO) formed during service operations. Considering the major functions of each coat, the bond coat (BC) mainly protects the substrate material from the tough oxidative and corrosive environment and further it plays a role as improving the bonding between the ceramic topcoat and the substrate. The functions of each coat will be mentioned in subsequent sections. As shown in Figure 1.4, the BC layer is more resistant to oxidation than the metal substrate and owing to oxidation of the BC during in-service conditions the TGO forms, as an effective barrier to oxygen diffusion [2, 27].

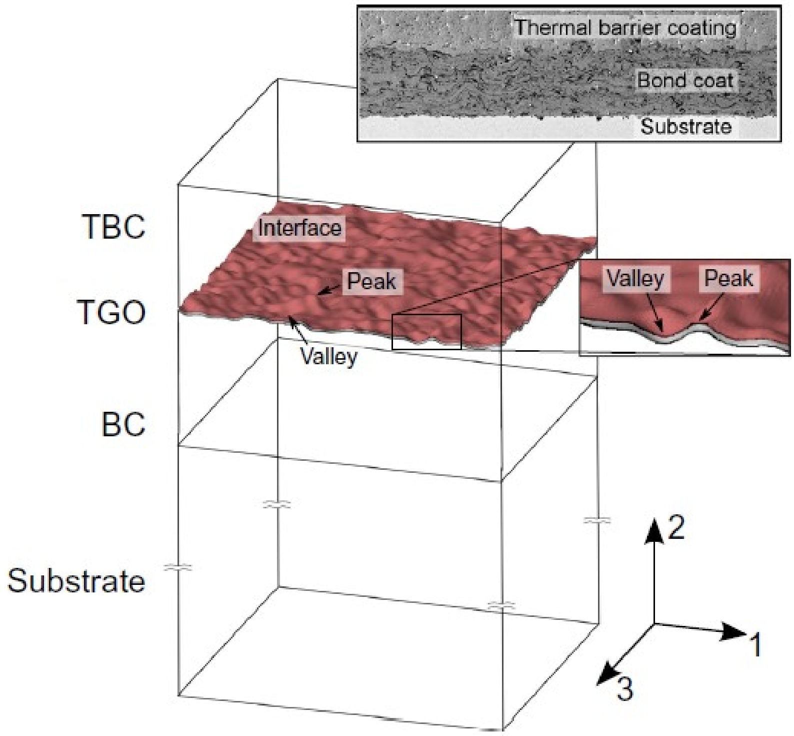

Figure 1.4: Schematic representation of a TBC system consisting of substrate coated with a BC and TBC in which during service conditions a TGO is seen, [4].

1.1.1 Bondcoat (BC) and Formation of Thermally Grown Oxide (TGO) Layer

The BC is the first layer that is in contact with the substrate material, the metallic part has two major functions that are being an interlayer between the TC and the substrate by increasing the adherence and protecting the substrate from chemical attacks since the TC has a porous structure [25, 28]. The first step for a proper BC is to select the correct materials having the thermal expansion coefficient close to the substrate material and the TC. Hence in this way, the stresses forming during in-service conditions via shrinkage or expansion while heating and cooling can be kept minimum [7]. BCs are commonly produced from metal alloys and TCs are ceramic materials as will be mentioned in 1.1.2. Therefore, there is relatively large expansion mismatch between bondcoat and ceramic layer this imposes a tension stress in the ceramic on heating. the tension on ceramic film layer can be decreased by decreasing the thermal expansion coefficient between these two layers [29]. As a result of porous structure of the TC itself, oxygen has a chance to diffuse through this layer and this enables a formation of an oxide layer between the TC and the BC that protects the substrate against the chemical attacks. This layer is called as the thermally grown oxide (TGO) layer having thickness between 1-10 μm [25, 30] which acts as an excellent diffusion barrier having a low oxygen diffusivity. Most of the time, the inward diffusion of the oxygen through TGO plays an important role for TGO growth however, in some cases, TGO growth can also be controlled by the outward diffusion which Al causes a TGO formation at the TGO/TC interface [11]. It is very critical to understand the properties of the TGO while understanding the performance and the failure of the TBCs. It is known that the TGO is slowly growing at high temperatures with perfect mechanical integrity. Hence, TBC failure can occur when the TGO exceeds the previously mentioned critical thickness values. This failure mechanism has the same background with the critical thickness for the loss of coherency of epitaxial thin films depending on the mismatch between the elastic strain energy in the growing films [2]. Hence, the TGO, should be homogeneously distributed to the surface with a continuous and a dense structure. According to the year-to-date applications and the studies conducted by Richer et.al. [31], the TGO can be made of α-α-Al_2O_3 and if so, there is also some other metallic oxides apart from alumina [31]. In Figure 1.5, the formation and followed by thickening of TGO can be seen according to the studies of Heeg and colleagues [5].

As mentioned before in order to understand the failure mechanism of TBCs, it is important to know the geometry of the TGO. Aktaa and coworkers hence, simulated the volume growth of the TGO which it is in the perpendicular direction to the interface [6]. In their research the interface is modelled by a sinusoidal wavy interface which

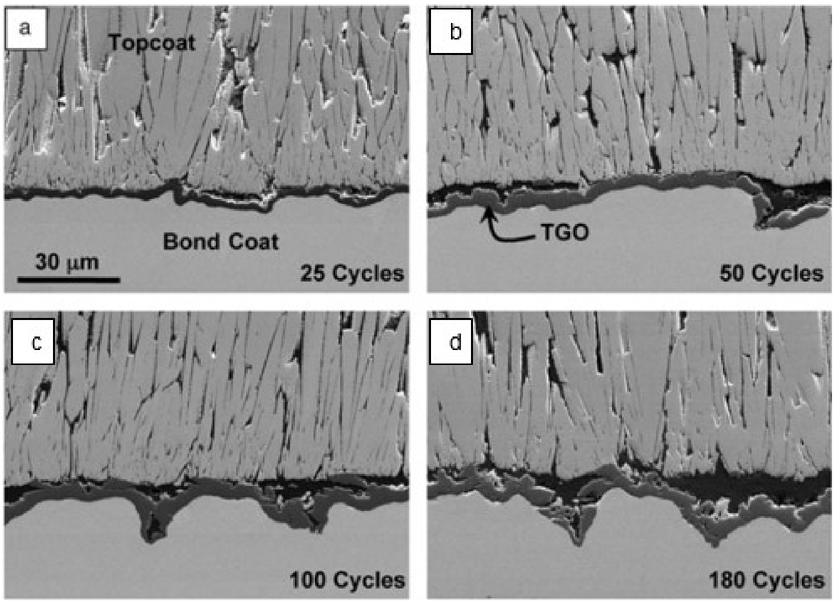

Figure 1.5: SEM image of TGO formation and thickening a) after 25 cycles b) after 50 cycles c) after 100 cycles d) after 180 cycles locally by using the electron beam physical vapor deposition method of 7 wt% yttria-stabilized zirconia thermal-barrier coating (TBC) on a Pt-modified nickel aluminide bond coat [5].

is commonly seen in literature. The wavelength of the interface was around 0.06 mm with the amplitude around 0.01 to 0.06 mm [6]. After introducing a crack in the TBC close to the peak region in the sinusoidal rough interface, it was noted that the TGO growth increases the equivalent strain energy release rate G_{eq}, the relation is given in Equation 1.1, at the end of the thermal cycle by almost 50%. Additionally, mode-II strain energy release rates, G_{II} according to the study conducted, also increase as a result of the oxidation of BC and TGO growth [6].

$$G_{eq} = \frac{1}{2}\left(G_I + 3G_{II} + \sqrt{G_I^2 + 6G_IG_{II}}\right) [6] \tag{1.1}$$

Furthermore, according to the study of Richer and his colleagues, oxides other than α-Al_2O_3 form in time at the TGO layer when the bond coat is CoNiCrAlY. Having α -α-Al_2O_3 in the TGO is advantageous due to the fact that oxygen permeability of α-α-Al_2O_3 is low and then the growth rate is low. Then, the failure arising from the TGO is postponed [31]. Therefore, the selection of the bond coat material is a critical issue in TBCs.

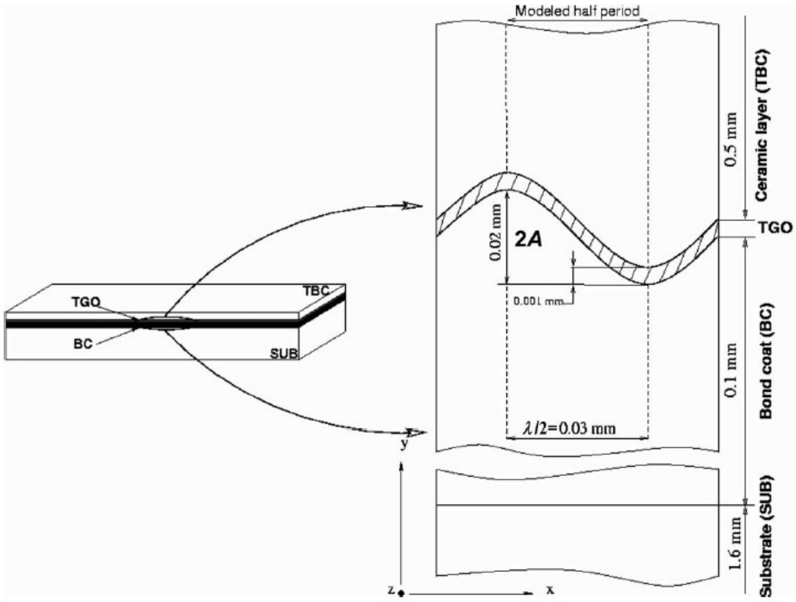

Figure 1.6: TBC system model of Aktaa et.al. [6]

1.1.2 Top Coat (TC)

The outermost layer of the TBCs is the topcoat which is indirect contact with the hot working gases in a gas turbine or other hot working components. Hence, the main task of this layer is to provide a thermal insulation [25, 32]. The essential requirement of the topcoat is a high melting temperature since it is the contact point to the hot gas temperature. Furthermore, a low thermal conductivity in order to satisfy the perfect insulation, a similar thermal expansion coefficient with the substrate to prevent the mismatch between the layers during in-service thermal cycles, a good strain tolerance for good resistance to thermal shocks during each thermal cycle and above all, a good oxidation and corrosion resistance are desired properties for the TC.[25, 30, 33].

In consideration of the required properties, different from BC materials, ceramic materials are the most suitable type of materials that can be used as a topcoat. As can be seen in Figure 1.7 considering the thermal expansion coefficient and the thermal conductivity properties, tetragonal zirconia is the most conventionally used ceramic material. Zirconia transforms into a monoclinic phase at temperatures around 1170°C leading to a volume expansion [34]. This expansion has a negative effect, residual stresses. Hence, yttria addition to zirconia has been a convenient method in order to

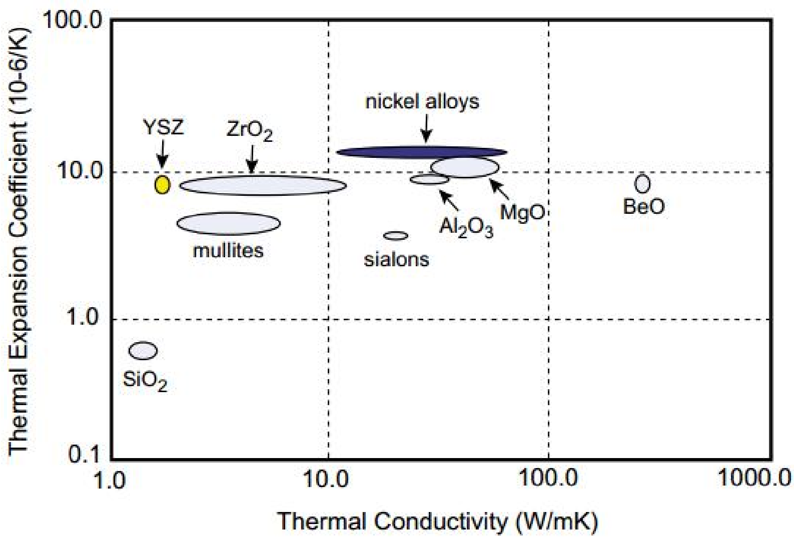

Figure 1.7: Representation of thermal expansion coefficient and thermal conductivity properties of various materials, [7]

avoid the transformation and the tetragonal phase is stabilized at low temperatures [25]. Yttria stabilized zirconia (YSZ) has a high thermal stability, high thermal expansion coefficient with a low thermal conductivity making it a desirable material to be used as a topcoat. Further, as shown in Figure 1.7 other ceramics like α-Al_2O_3, MgO, mullite and SiO_2 are unstable at high temperatures as a result of their polymorph properties [7, 25]. The success of the topcoat also depends on the strain tolerances according to the deposition method. While different methods result in different strain tolerances, in plasma spray coatings the tolerance is related with porosities in between splats and voids resulting with cracks [19, 25].

1.1.2.1 Yittria Stabilized Zirconia (YSZ)

Yittria stabilized zirconia (YSZ) has a numerous advantages and due to this reason it is the most widely used material for TBC applications. YSZ structure is basically formed by a high point defect that substitution of Zr^{4+} ions by Y^{3+} ions in the fluorite structure, producing a small spacing between point defects [18]. It is known that, YSZ is more resistant to corrosion than ZrO_2 coating stabilized by CaO or MgO [33, 35]. In addition, 18-20YSZ coatings are another variation of YSZ that has been studied by Troczynski and coworkers [36]. According to their studies, the most explicit disadvantage of YSZ is the limited operation temperature which is less than 1473K for considering long term applications. This is due to the fact that, increase in temperature results in a phase transformation from the tetragonal (t) structure to the tetragonal (t) and the cubic Fluorite (F) structure given in Figure 1.8 and followed by monoclinic (m) structure leading to a crack formation in the coating [8, 33]. Further to say, when there is silica as impurity in the YSZ coating, the thermal cycling life of the coating decreases since silica segregation to the grain boundaries is seen in the bulk zirconia-based zirconia and these segregates become excessive and collect at the triple points.

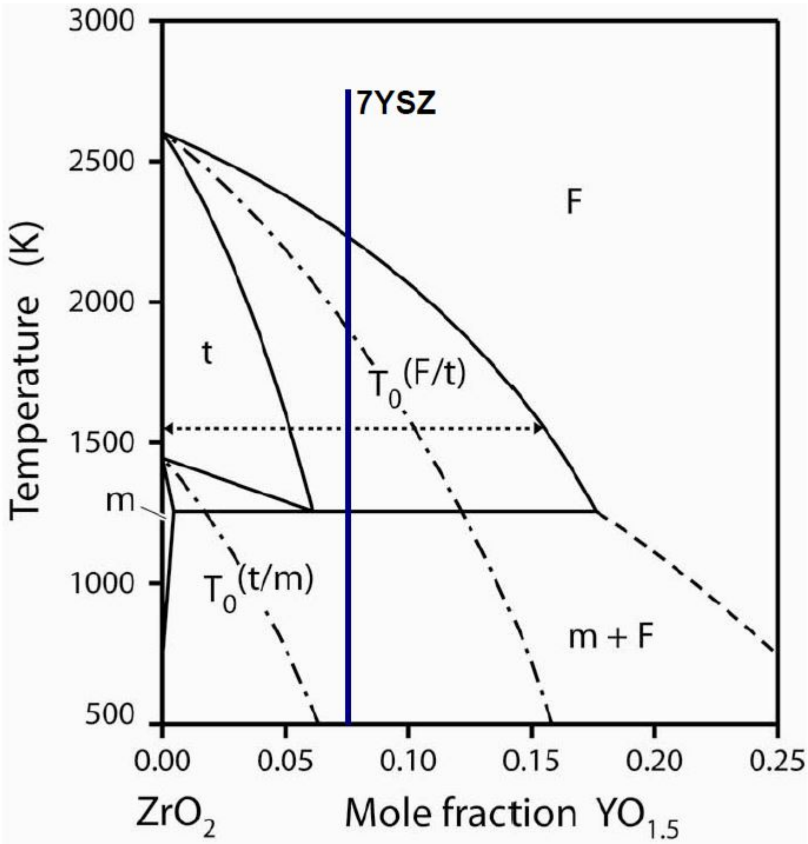

Figure 1.8: Phase diagram of YO1.5-ZrO2 [8]

These silica segregates cause a shape and size change of the grains, further Y_2O_3 dissolve from the YSZ and finally a localized destabilization can be seen [33, 37]. Moreover, a thin layer of silicates on the top of the bond coat acting as an oxygen barrier may improve the oxidation resistance of the bond coat since they have lower oxygen conductivity [37]. Still, these kind of problems could have been eliminated to a large extend by using alumina and mullite as the BC that are acting more oxidation resistant [38].

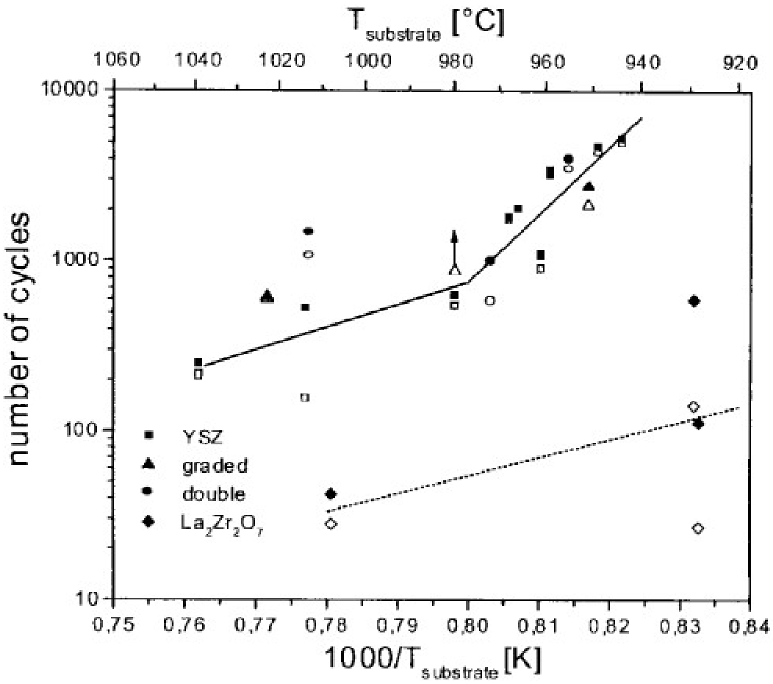

Figure 1.9: Thermal cycling lives of TBC depending of the substrate, [9]

The dependence of the thermal cycling lives on the substrate temperature is presented in Figure. 1.9 [9].

1.2 Methods for TBC Deposition

Contemporary applications show that there are two main methods to produce TBCs. These are known as the air plasma spraying (APS) and the electron beam physical vapor deposition (EB-PVD). The YSZ coatings are produced by either Air Plasma Spray (APS) and/or Electron Beam Physical Vapor Deposition (EB-PVD). Design considerations for the selection of coating method depends on the requirements such as component size, cost and performance. Each coating method has its own advantages and disadvantages. Conventional APS is relatively inexpensive but limited to porous or dense YSZ coatings, whereas filamentary strain tolerant coatings can be produced by EB-PVD method but it is more expensive compared to the APS method.

1.2.1 Air Plasma Spraying (APS)

Air plasma spraying, in other words atmospheric plasma spraying is basically a thermal spraying method consisting of composition of the cladding environment, the plasma steam, the powder material to be deposited and the substrate material in order to provide thermal, wear and corrosion resistances. During APS, the powder is injected inside the plasma steam which is formed by a steam of plasma gas between the two oppositely charged bars and the powder particles melt in the plasma steam while with the acceleration they are pushed to the surface. Pushed particles are cooled when they hit to substrate surface forming a layer-by-layer structure. In this structure each layer is called as a "splat" [1]. Figure 1.10 shows a schematic representation of the APS method. A representative microstructure after APS method can also be seen in Figure 1.11.

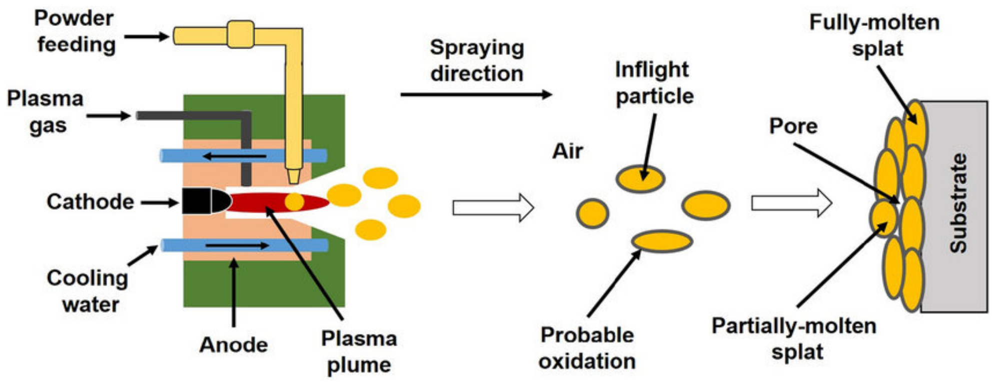

Figure 1.10: Schematic representation of air plasma spraying (APS), [10]

1.2.2 Electron Beam Physical Vapor Deposition (EB-PVD)

Electron Beam Physical Vapor Deposition (EB-PVD) method is based on a positively charged anode generating an electron beam under a high vacuum chamber which is targeted to the ingot supplement consisting of ceramic materials to be coated. This high energy is transmitted via the electron beam and the ingot supplement vaporizes forming a coating on the substrate material as seen in Figure 1.13.

Since vaporization of ceramic supplement is required during the process, this method is defined as a very slow and energy consuming method compared to the APS. On the

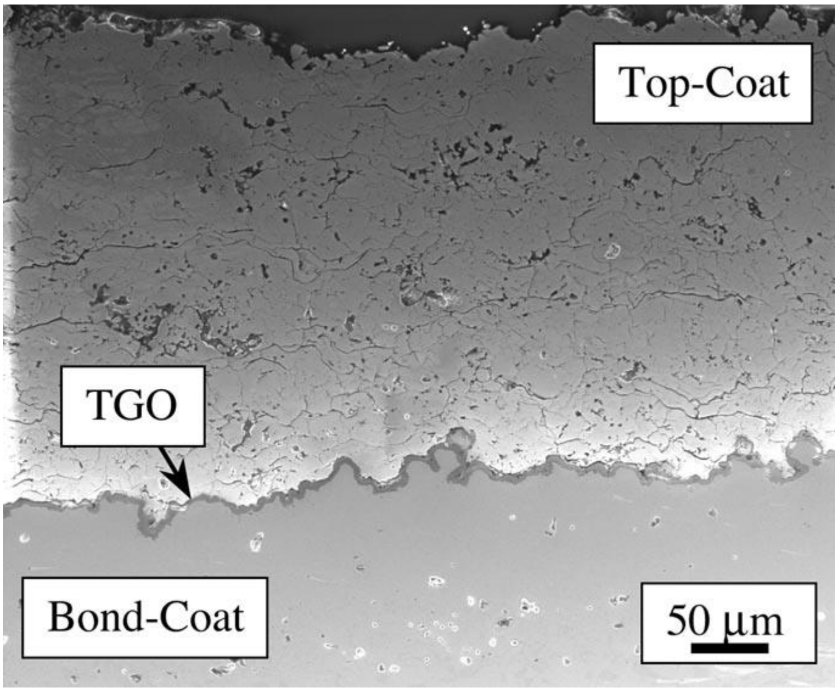

Figure 1.11: SEM image of TBC with 120 thermal cycles by using APS method, [11]

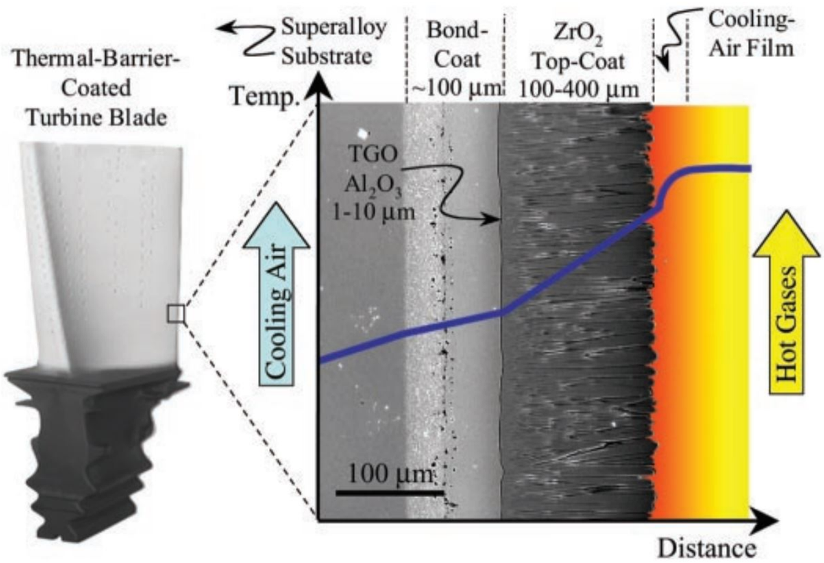

Figure 1.12: SEM image of a cross section of a TBC system by using EB-PVD as a deposition method showing the temperature reduction provided by the TBC [11]

other hand, the advantageous microstructure given in Figure 1.13b is more feather-like and more compact with free of large gaps.

As a result of this compact structure, the EB-PVD method shows a better insulation

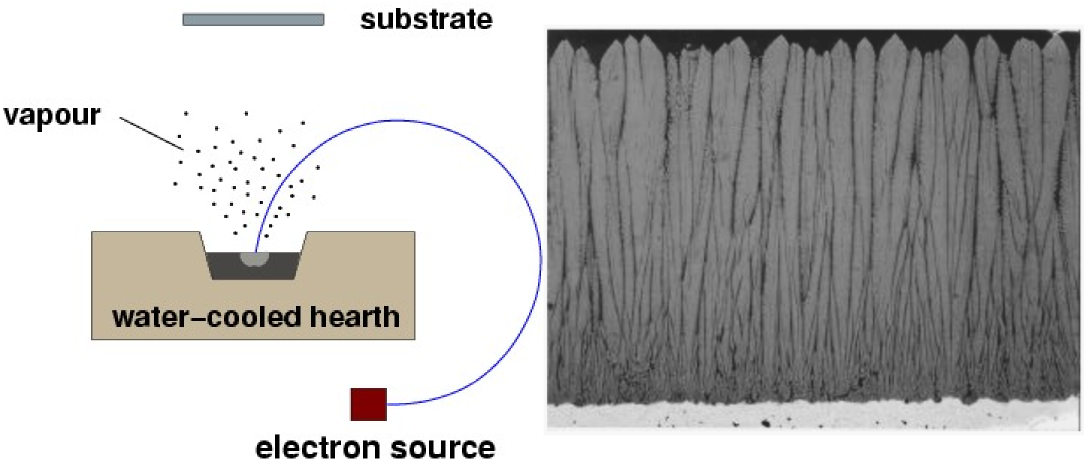

(a) (b)

Figure 1.13: (a) a schematic representation of EB-PVD method [12] (b) typical microstructure of EB-PVD deposited TBC system

performance compared to the APS method and other TBC coating techniques which are not mentioned in this study. Furthermore, the interfaces are also very smooth in the EB-PVD compared to the APS method. Therefore, the main disadvantage is the smooth interface causing coming from this occurrence is the interfacial crack propagation easier that is a great problem in industry.

1.2.3 Failure in TBC Systems

TBC systems consist of ceramic coatings so as to protect the substrate metal from creep, fatigue, especially thermal fatigue and corrosion. Therefore, a homogeneous and an effective coating system without any failure increases the efficiency of the turbine or the engine providing a long lifetime despite of the exterior environment. Since these coatings are ceramic materials, it is possible to observe several defects other than porosity coming from the ceramic structure. Furthermore, the coating thickness is an important parameter controlling the thermal insulation in as sprayed conditions of TBCs. An increase in thickness of the ceramic coating layer increases the thermal insulation efficiency. However, this increase in thickness also results in an increase in the residual stresses which become the main topic for many studies.

In order to investigate the thickness effect some studies were conducted with thick TBCs. Segmentation cracks and spallation have been reported as common failures [26]. Additionally, during service conditions, TBC failure by spallation of the top coat can also be seen in engines. The factors resulting in TBS failure can be summarized as: the thermal expansion coefficient mismatch, the oxidation of the metal substrate and the change in the microstructure, composition and interfacial morphologies and therefore the properties of the TBC system. This is the reason why failure mechanisms seen in TBCs are not completely understood [11].

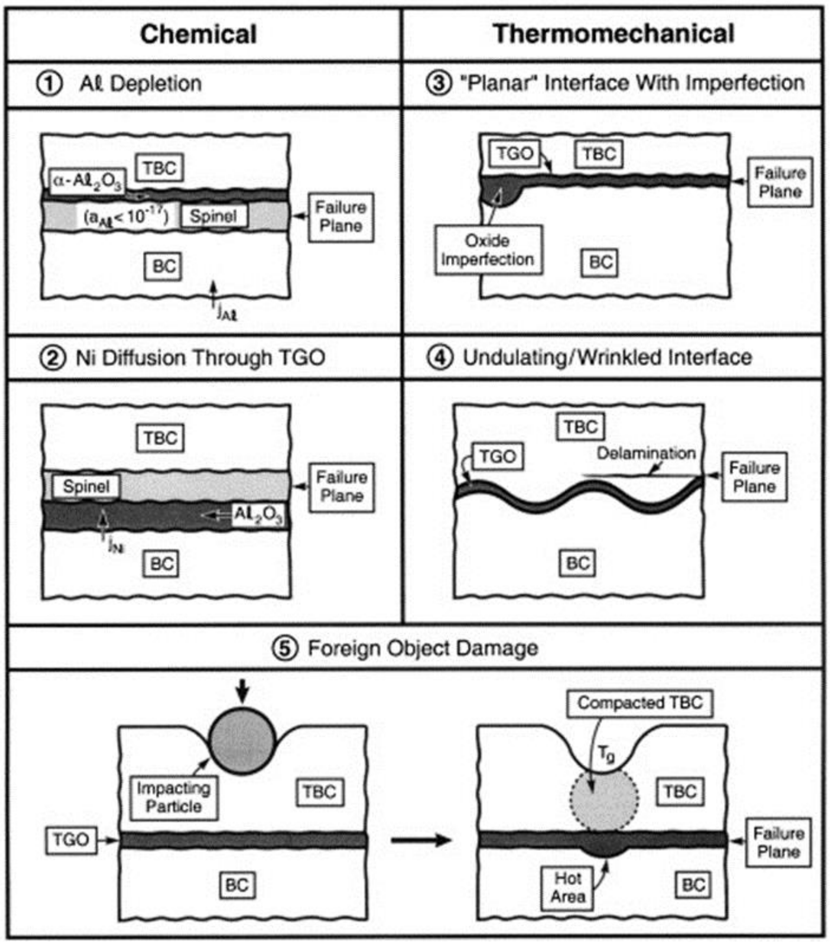

Figure 1.14: Different failure modes of TBC coatings [13]

Aluminum depletion, imperfections in the planar interface, nickel diffusion via TGO, foreign object damage and finally wrinkled interface can be named as different failure modes of TBCs [1]. These failure modes can be seen in Figure 1.14. In aluminum depletion failure and nickel diffusion chemical effects are observed resulting in an interface cracking due to weakening of the topcoat and the BC. The major driving force for atoms to diffuse is the high temperature. This diffusion causes a composition change in the interface and therefore the interface properties change to brittle leading to failure [1].

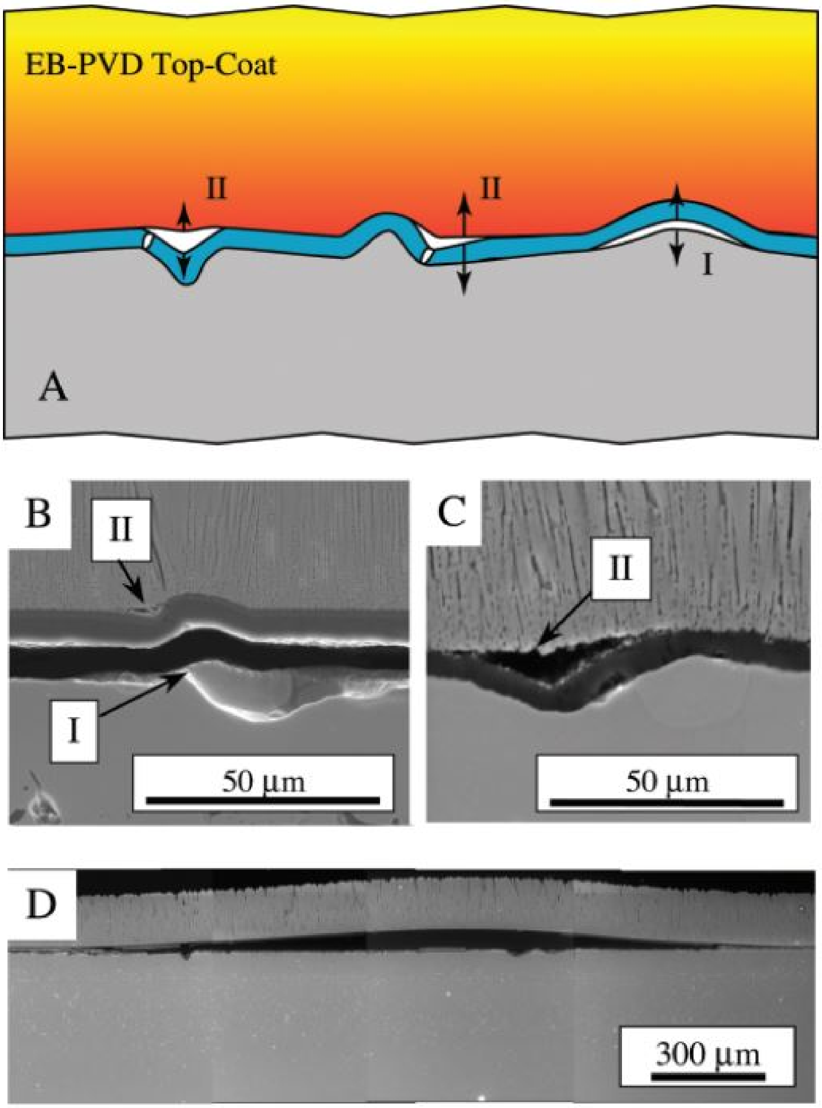

Figure 1.15: TBCs by EB-PVD (I) BC/TGO crack opening at the interface (II) Top-coat/TGO crack at the interface and (III) Interface porosity opening crack, [11]

The planar interface occurs as a result of the TBC coating produced by EB-PVD. As a result of the process, porosities and wrinkles can be seen at the interface, see Figure 1.15. Although the surface is very smooth, it is easy to see cracks. These cracks may start with a small porosity leading to a spallation of the TBC. Furthermore, if there

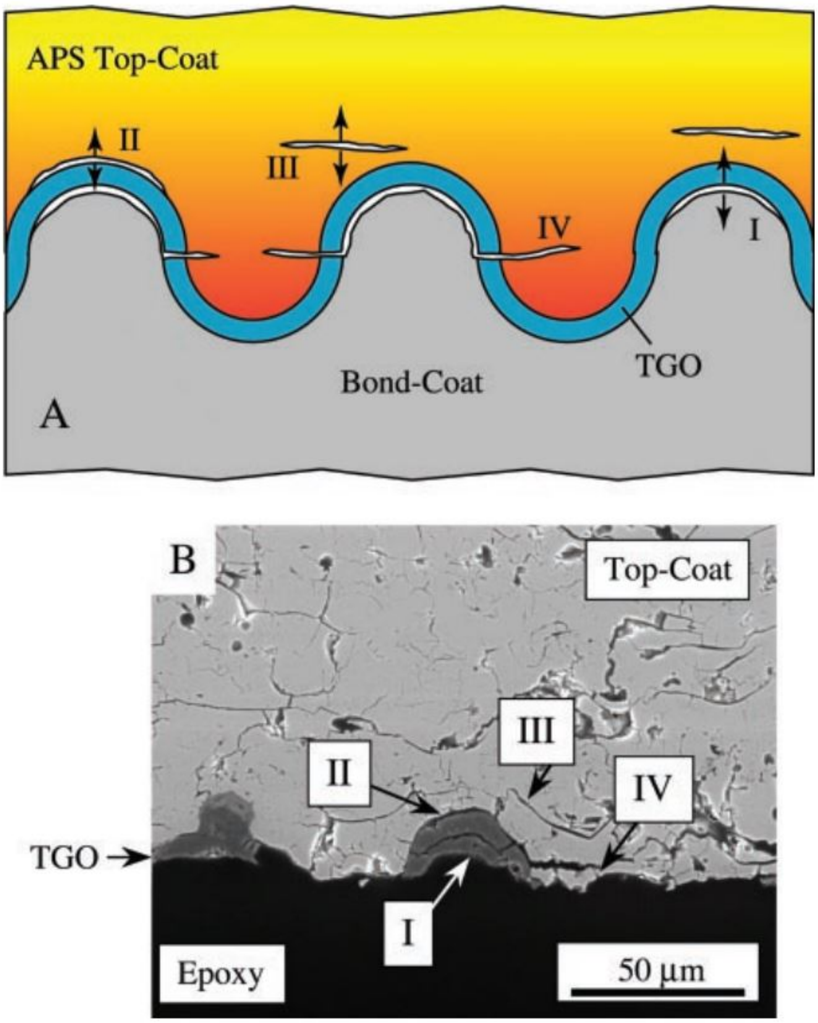

Figure 1.16: TBCs by APS (I) BC/TGO interface opening crack (II) TC/TGO interface opening crack (III) TC opening crack (IV) Crack propagation through TC, [11]

is a considerable mismatch of the thermal expansion coefficients of the topcoat and the BC, heating and cooling in service conditions give rise to an interface opening. When TBCs are deposited by using the APS method, the interface becomes wrinkle. As a result of the thermal mismatch between the topcoat and the BC together with the TGO, peaks and valleys formed by the APS method, are under pre-tension and pre-compression. These cycling pre-tension at the peak region forms a crack opening at the bondcoat and the TGO interface and the TGO and the topcoat interface. Studies showed that, interface openings mostly seen at the peaks where there is a pre-tension. Followed by the pre-tension, cracks may propagate at the interface and pass through the BC or even topcoat leading to failure, see Figure 1.16.

The final failure represented in Figure 1.14 is the foreign object damage based on the particles in the service environment. This failure is an exterior type of damage that can be caused by any kind of dust in the ambient. Therefore, failure occurs as a result of corrosion causing melted dust particles crumbling of small pieces of ceramic coatings and metallic substrates.

1.3 Numerical Studies on TBCs

The extended finite element method (XFEM) and cohesive zone model (CZM) have been used in last decades to simulate the crack initiation and propagation behavior of the TBCs. The failure patterns of the TBCs can be monitored using these methods and eventually the life predictions of the TBCs under the actual service conditions are expected to be realized [39].

The XFEM can be used to simulate the propagation behavior of the cracks at the ceramic film layer of the TBCs while the cohesive zone model (CZM) can simulate the degradation of interface stiffness and delamination of the TC/BC interface [39].

Fan et al. [40] have investigated the relation between the periodical surface crack spacings in the top coat layer of TBC system and the interface delamination. The cohesive zone model is used to model the interface delamination and to this end cohesive elements are created at the TC/BC interface. The main outcome of their study is the calculation of critical surface crack spacing or in other words the distance between vertical cracks in the film layer that reach to interface. It is found that the critical surface crack spacing value at which the delamination starts is about twenty times of the film layer thickness. Their experimental studies supports the critical surface crack spacings values as well. It is proposed in this study that the TBC performance and durability can be enhanced by increasing the surface crack density which reduces the possibility of the interfacial delamination.

Leo et al. [41] have investigated the delamination behavior at TBCs' interface with the CZM using a bilinear traction-separation interface constitutive relation with two dimensional simulations. They modeled their standard tension, shear and asymmetric four-point bending mixed-mode experimental specimens with zero initial thickness four-noded cohesive elements (COH2D4) in Abaqus. FEM simulations are incorporated with experiments and the interfacial failure initiation and propagation parameters used in the simulations are iteratively varied to match the load-displacement results of the experiments for all three experiments. It is proposed in this study that the interfacial material parameters of the APS-TBCs for FEM simulations can be determined with the FEM and experiments incorporated methodology represented.

Zhang et al. [42] have used the XFEM to investigate the relation among the interface roughness, the strain energy release rate and the film layer cracking behaviour of the APS-TBCs. It is shown in the study that periodical vertical film layer cracks are affected by the interface roughness. It is proposed that the roughness of the interface has an important effect on the cracking patterns, the strain energy release rate and the distribution of the interfacial stress. According to the results of the study the distributions of the stress and the strain energy release rate in the regions of convex and concave asperities of the substrate are diverting each other. The XFEM is used to perform for the numerical study to determine the crack propagation path in the TBC system, developing stresses and the strain energy release rate. The study basically argues that the interface roughness has a tremendous effect on the development of the stress and changes the values of the strain energy release rates. Furthermore, the study defends that the durability of TBCs can be improved by controlling the interface morphology artificially.

Yang et. al [43] combined single-edged notch bending tests by using the digital image correlation technique with the XFEM to calculate the fracture strength and the fracture toughness of 8YSZ. In their study notched finite element model is used to simulate fracture mechanisms of a single edge notched beam of 8YSZ. It is a complementary material characterization study using the XFEM and show that the XFEM technique could be used with determined experimental data to predict the TBC failures in complex geometries. However, the values calculated for the fracture stress and fracture toughness are not used in this study.

1.4 Scope of the Study

Thermal barrier coatings are ceramic insulation coatings that shield the substrate superalloys mechanically and thermally from the extreme environment that consists of hot gasses. TBCs directly affect the performance of a jet engine in terms of fuel efficiency and service life because they are used in locations in a typical aero jet engine where the most extreme environment being encountered. Therefore, the durability of TBCs directly correlates with the the durability of jet engines. Understanding their complex fracture mechanisms is significant for the design stage. This study focuses on the investigation of the fracture mechanisms of the TBCs.

In this study, it is aimed to investigate the failure mechanisms of APS-TBC numerically under four-point bending loading by using a combined XFEM/CZM model in the commercial software Abaqus. The study can be considered as a complementary numerical study of the experiments in the literature [1]. In order to simulate experimental conditions two different techniques combined to simulate complete fracture mechanisms of TBCs which consist of initiation and propagation of the surface cracks followed by delaminations at the interface. Three different thickness models are created for the FEM simulations according to the data obtained from the experimental study [1]. The XFEM is used to monitor the crack initiation and propagation at the top coat and the CZM is used to model the delamination at the top coat/bond coat interface. In simulations and experiments cracks first initiate at the uppermost layer of the TC and propagate through the TC. Then, delaminations occur at the interface after vertical cracks reach the TC/BC interface. The average crack spacing increases as the thickness of the YSZ layer increases. Furthermore, the delamination failure becomes more prominent as the YSZ layer thickness and the surface cracks spacing in the TC layer increase.

CHAPTER 2

METHOD

In this study, finite element models are created to simulate four-point bending experiments in the literature [1] to investigate the cracking mechanisms of the TBC by using the Extended Finite Element Method (XFEM) and the Cohesive Zone Method (CZM). In this chapter the history, theoretical background and general formulations of the XFEM and CZM methods are presented. Furthermore, the implementation of these methods to Abaqus and the limitations of Abaqus while using the XFEM and the CZM are explained. Finally, the level set method, which is used for tracking crack surfaces and monitoring their progress, is explained.

2.1 Extended Finite Element Method

While solving fracture mechanics problems by using analytical methods, many limitations emerge, simplifications and assumptions are required. In order to simplify the problem, generally homogeneous and isotropic linear elastic materials are used in an infinite domain with boundary conditions in the simplest forms. However, in real-world problems of sophisticated structures, the material itself contains small defects and discontinuities. Boundary conditions are more complicated and material properties are heterogeneous. Generally, the materials in real-world problems, are not homogeneous and isotropic linear elastic compared to most analytical methods' assumptions. On the other hand, satisfactory fracture mechanics simulations could be executed through numerical methods. Among these applications, the finite element technique is the most common and adopted method, and it is mostly used in complex engineering problems. Therefore, several different software packages are developed throughout the years on the basis of the finite element technique [14].

In the finite element method, non-smooth stress and strain fields around the crack tip can be monitored by refined meshes leading to a sudden increase in the number of degrees of freedom of the finite element model. Especially in three dimensional problems the situation becomes worse. Even though the finite element method seems to be well-suited for fracture mechanics problems, these defects are the obstructions of its use.

XFEM has been used to investigate crack initiation and propagation behaviour of different engineering materials in recent years and it became one of the most popular computational tools to analyse crack problems because of its computational advantages.

The XFEM is a numerical technique which is able to model internal and external boundaries such as holes, cracks etc. without requiring the mesh to comply to these boundaries. XFEM uses the partition of unity concept [44, 45] to adapt the internal boundaries in the discrete model and the technique itself is based on a standard Galerkin procedure. XFEM was originally proposed by Belytschko and Black [46]. They provided this method for enriching finite element solutions in order to solve crack propagation problems with minimum remeshing. Moes et al. [47] and Dolbow et al. [48, 49] presented an enhanced technique by adapting an enrichment that includes the asymptotic near tip field functions and a Heaviside function H(x). Later, the concept was adapted to three dimensional static crack problems by Sukumar et al. [50]. Belytschko introduced the technique to model arbitrary discontinuities in finite element approximation. The technique contemplates both the derivatives of the discontinuities and the discontinuity itself in the function [51]. In contrast to the element enrichment procedure of Benzley [52], the advantage of this enrichment process is the fact that it provides a response nearly independent of element size for a wide range. However, there is a drawback of the presented method which is the need for a variable number of degrees of freedom per node. Furthermore, the enriched elements with the asymptotic-near tip field functions require transition element. These are the most significant weaknesses of the technique [53].

2.1.1 Partition of Unity Method

The accuracy of finite element solution can be improved by using the so-called enrichment procedure. In other words, if a priori known analytical solution of the problem is included in the finite element formulation the accuracy of the results can be increased. The number of the nodal degrees of freedom increases as this concept is adapted to fracture mechanics problems because the analytical crack-tip solution is incorporated to the framework of the isoparametric finite element discretization to improve the crack-tip field prediction, see [54].

The partition of unity property is satisfied by the set of isoparametric finite element shape functions N_j

$$\sum_{j=1}^{m} N_j(x) = 1 \tag{2.1}$$

The partition of unity finite element method (PUFEM), proposed by [55], uses the enrichment functions concept in conjunction with the partition of unity feature given in Equation (2.1). PUFEM, as given in Equation (2.2) provides the approximation of the displacement within an element by using the enrichment functions $p_i(x)$ and the complementary degrees of freedom a_{ji} related to the enriched solution.

$$u^h(x) = \sum_{j=1}^{m} N_j(x) \left(u_j + \sum_{i=1}^{n} p_i(x) a_{ji} \right) \tag{2.2}$$

The total number of nodes of each element is determined by m and the number of enrichment functions p_i is determined by n. Equation (2.2) can be written for an enriched node x_k

$$u^h(x_k) = \left(u_k + \sum_{i=1}^{n} p_i(x_k) a_{ji} \right). \tag{2.3}$$

However, Equation (2.3) does not satisfy the interpolation property at node k. Therefore, the enriched displacement field is modified as follows in Equation (2.4) [54] to get around this problem

$$u^h(x) = \sum_{j=1}^{m} N_j(x) \left[u_j + \sum_{i=1}^{n} (p_i(x) - p_i(x_j)) a_{ji} \right]. \tag{2.4}$$

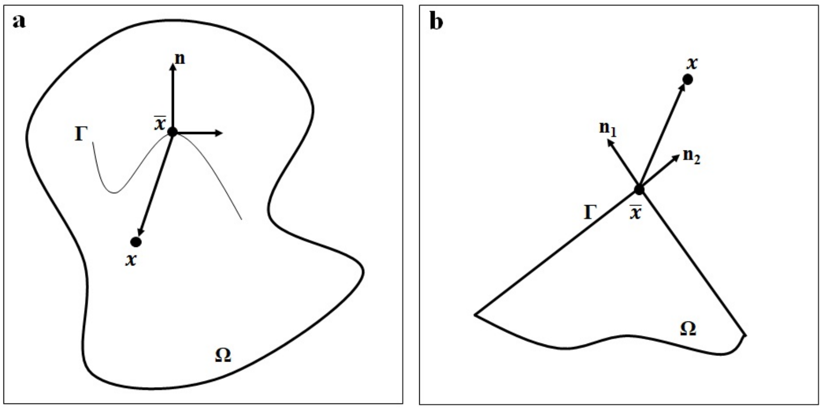

Figure 2.1: (a) smooth crack (b) kinked crack. Figure is adapted from [14]

2.1.2 Generalized Finite Element Method

In generalized finite element method (GFEM), see [56], shape functions are used for the ordinary and enriched parts of the finite element discretization independently to increase the order of integrity, i.e.

$$u^h(x) = \sum_{j=1}^{m} N_j(x)u_j + \sum_{j=1}^{m} \overline{N}_j(x)\left(\sum_{i=1}^{n} p_i(x)a_{ji}\right) \tag{2.5}$$

where $\overline{N}_j(x)$ are the shape functions related to enrichment basis functions $p_i(x)$. However, the interpolation at nodal points are not satisfied in Equation (2.5) as well. Therefore, the same procedure explained in previous section is applied to get around this problem

$$u^h(x) = \sum_{j=1}^{m} N_j(x)u_j + \sum_{j=1}^{m} \overline{N}_j(x)\left[\sum_{i=1}^{n} (p_i(x) - p_i(x_j))a_{ji}\right]. \tag{2.6}$$

2.1.3 Enrichment Functions

Cracks are modelled by two different types of enrichment functions in two-dimensional problems.

- **Heaviside Enrichment Function**

$$H(x,y)=\begin{cases}1 & \text{for} \quad (x-\overline{x})\cdot\mathbf{n}>\mathbf{0}\\ -1 & \text{for} \quad (x-\overline{x})\cdot\mathbf{n}<\mathbf{0}\end{cases} \tag{2.7}$$

For Heaviside enrichments, only the nodes that belong to an element split by a discontinuity may be used. The Heaviside function is able to model a jump in the displacement field which is caused by the seperation of the domain by a crack. In a deformable body Ω in Figure 2.1, the continuous curve Γ represents a crack in the domain, and $\mathbf{x}(x,y)$ is an arbitrary point in the body, $\overline{\mathbf{x}}(x,y)$ is the closest point to $\mathbf{x}(x,y)$ that belongs to Γ and $\mathbf{n}$ is the outward normal vector of the Γ at point $\overline{\mathbf{x}}(x,y)$. The Heaviside function can be defined as in Equation (2.7) in order to assign the position of $\mathbf{x}(x,y)$ relative to the crack location. The Heaviside function includes the discontinuity across faces of the crack.

- **Asymptotic Near-Tip Field Function**

The Heaviside function could not be used to estimate the displacement field in the elements which are partially cut by the crack, in other words elements that contain the crack tip. In this case asymptotic near-tip field enrichment functions initially introduced by [57] for the use in Element-Free Galerkin method (EFG) can be used. These functions have been extensively used for fracture problems and later they were employed by [58] in XFEM formulation. Following four functions expressed in local crack tip polar coordinate system (r,θ) are responsible to define the fracture tip displacement field

$$\begin{aligned}\{F_i(r,\theta)\}_{i=1}^{4}=\{&\sqrt{r}\cos(\frac{\theta}{2}),\sqrt{r}\sin(\frac{\theta}{2}),\\ &\sqrt{r}\sin(\frac{\theta}{2})\sin(\theta),\sqrt{r}\cos(\frac{\theta}{2})\sin(\theta)\}.\end{aligned} \tag{2.8}$$

By using four enrichment functions in Equation (2.8) new degrees of freedom are added to each node in every direction. The term $\sqrt{r}\sin(\theta/2)$ defines the discontinuity in the approximation over the crack tip because it is the only discontinuous function through the crack surface. However, other three functions are used in the neighbourhood of the crack tip only to improve the solution of the finite element approximation, especially to improve the accuracy of the calculation of stress intensity factors, see [59].

Following expression could be used based on the four enrichment functions given in Equation (2.8)

$$
\begin{aligned}
u^h(x) &= u_{FEM}(x) + u_{ENR}(x) \\
&= \sum_{i \in I} N_i(x) u_i + \sum_{j \in J} N_j [H(x)] a_j \\
&+ \sum_{k \in K_1} N_k(x) \left[\sum_{l=1}^{4} b_k^{l_1} F_l^1(x) \right] \\
&+ \sum_{k \in K_2} N_k(x) \left[\sum_{l=1}^{4} b_k^{l_2} F_l^2(x) \right]
\end{aligned}
\tag{2.9}
$$

Note that Equation (2.9) is written for a domain that contains two distinct crack tips. Furthermore, Equation (2.9) can be reformulated to satisfy interpolation property as follows

$$
\begin{aligned}
u^h(x) = &\sum_{i \in I} N_i(x) u_i + \sum_{j \in J} N_j \left[H(x) - H(x_j) \right] a_j \\
&+ \sum_{k \in K_1} N_k(x) \left[\sum_{l=1}^{4} b_k^{l_1} \left[F_l^1(x) - F_l^1(x_k) \right] \right] \\
&+ \sum_{k \in K_2} N_k(x) \left[\sum_{l=1}^{4} b_k^{l_2} \left[F_l^2(x) - F_l^2(x_k) \right] \right]
\end{aligned}
\tag{2.10}
$$

where J represents the set of nodes of the elements which are splitted by the crack completely and enriched with the Heaviside enrichment function. K_1 and K_2 are the sets of nodes whose support domains include crack tips 1 and 2, and their near tip enrichment functions are $F_l^1(x)$ and $F_l^2(x)$, respectively. $b_k^{l_1}$ and $b_k^{l_2}$ are the vectors of additional degrees of freedom used to model fracture tips. u_i indicates the conventional degrees of freedom and a_j describes the additional degrees of freedom used to model crack faces.

2.1.4 Traction-Separation Law

The linear traction-seperation law proposed by [60] as shown in Figure 2.2a is used for the XFEM enriched region in TC. In Figure 2.2a, the horizontal axis of the graph refers to the separation and the vertical axis is the traction. The slope of the initial part k is the cohesive stiffness. The damage initiation occurs at point X, therefore k gives the value of the cohesive stiffness which is the ratio of traction stress to separation at point X. At point Y, an unloading occurs and the cohesive stiffness decreases to $(1-D)k$ for the next time increment. D refers to the damage parameter and the value of D is zero before damage initiation. The damage initiation occurs at point X and it finishes at point Z. The values of D are 0 and 1, respectively at points X and Z. In Figure 2.2b derivation of the damage parameter D is shown. The loading stiffness is given as $m = (1 - D)k$ derived in Equation (2.11) from Figure 2.2

$$m = (1 - D)\left(\frac{T^u}{\delta_y}\right) \tag{2.11}$$

T^u/(δ_y) gives the undamaged crack stiffness value k. T^u refers to traction stress if cohesive damage does not occur and T^d refers to actual traction stress with cohesive damage. Then the following condition could be derived from Figure 2.2

$$T\frac{(\delta_z - \delta_y)}{(\delta_z - \underline{\delta})} = \delta_y(1 - D)\left(\frac{T^u}{\delta_y}\right) \tag{2.12}$$

The damage parameter D can be written in terms of seperation (δ), by simplifying Equation (2.12) as

$$D = \frac{\delta_z(\delta_y - \underline{\delta})}{\delta_y(\delta_z - \underline{\delta})} \tag{2.13}$$

The ultimate failure arises when the energy release rate due to the crack opening exceeds the critical energy release rate G_C. G_C can be determined by calculating the area under the curve in Figure 2.2. The failure type relies strongly on the value of G_C; high G_C is related to the ductile failure and low G_C is related to the brittle failure. The critical crack opening δ_z, depends on the fracture stress T and the fracture toughness

K_I^C, and the relationship for mode I failure is as follows

$$\delta_z = \frac{2(K_I^C)^2}{E\underline{T}}. \tag{2.14}$$

Detailed discussion on relations given in Equations (2.11), (2.12), (2.13), (2.14) can be found in [15].

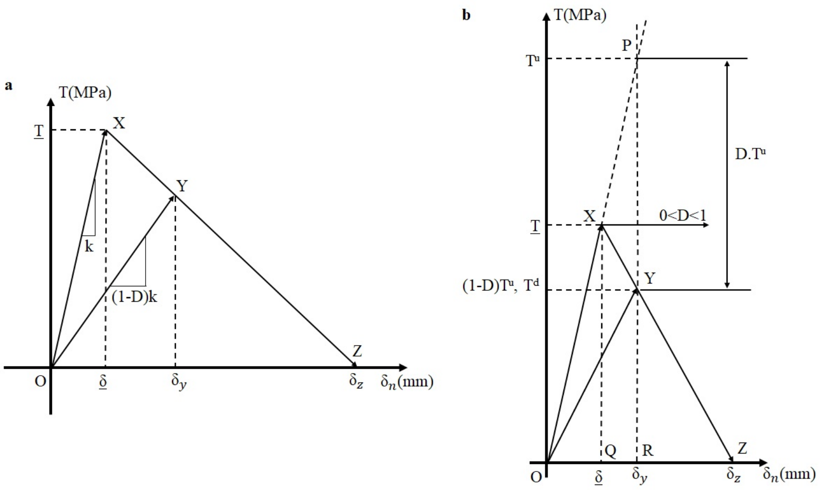

Figure 2.2: (a) Linear traction-seperation law; (b) Damage parameter and unloading process. Figure is adapted from [15].

2.2 Cohesive Zone Method

The Cohesive Zone Method (CZM) has been introduced in the early sixties to analyse damage process under static loading beyond the crack tip by [61]. A cohesive zone law, also known as traction-separation law, describes the constitutive behaviour between the relative displacement δ between two points and the traction T, see [62]. Abaqus allows two different alternatives to utilize the cohesive zone method in a finite element model. These are surface based and element based cohesive behaviour. In this study, surface based cohesive behaviour is used to model delamination at the TC/BC interface.

The surface-based cohesive behavior is defined as a surface interaction property and can be used to model the delamination at interfaces directly by using a traction-seperation constitutive model. Unlike the element based cohesive behaviour, the surface-based cohesive behavior ensures a simplified way to model cohesive connections with zero thickness interfaces.

Abaqus current traction-seperation model assumes linear elastic behaviour initially, followed by damage initiation and evolution. Elastic constitutive matrix is given in Equation (2.15) describes the elastic behaviour and it gives the relation between the normal and shear stresses with normal and shear separations.

$$t = \begin{Bmatrix} t_n \\ t_s \\ t_t \end{Bmatrix} = \begin{bmatrix} K_{nn} & K_{ns} & K_{nt} \\ K_{ns} & K_{ss} & K_{st} \\ K_{nt} & K_{st} & K_{tt} \end{bmatrix} \begin{Bmatrix} \delta_n \\ \delta_s \\ \delta_t \end{Bmatrix} = K\delta \tag{2.15}$$

For two dimensional problems nominal traction stress t has two components; normal traction t_n and shear traction t_s. For three dimensional problems third component; second shear traction t_t is added to the relation and δ_n, δ_s, δ_t given in Equation (2.15) denotes the corresponding separations.

2.3 XFEM implementation in ABAQUS

As it is explained in previous sections, the XFEM was first proposed in 1999. Therefore, there are not many commercial codes that use XFEM method. However, XFEM implementation provides enormous potential to the users. The most significant capability of the XFEM is that the finite element mesh does not need to conform the crack surface exactly. Several attempts have been made over the years to implement XFEM both in commercial FEA software and user developed codes. Abaqus and LS-DYNA are the most popular ones among them.

In 2009, Dassault Systems released version 6.9 of Abaqus software which includes basic XFEM functions. The implementation of the XFEM in Abaqus is based on phantom node method which was introduced by Hansbo [63] and later modified by by Song [64] and Rabczuk [16]. There is a fundamental difference between original XFEM formulation and Abaqus implementation; in Abaqus implementation the presence of the discontinuity is reproduced by superposing the phantom nodes to the classical finite element nodes. Phantom node method is explained in Section 2.3.1.

2.3.1 Phantom-node method

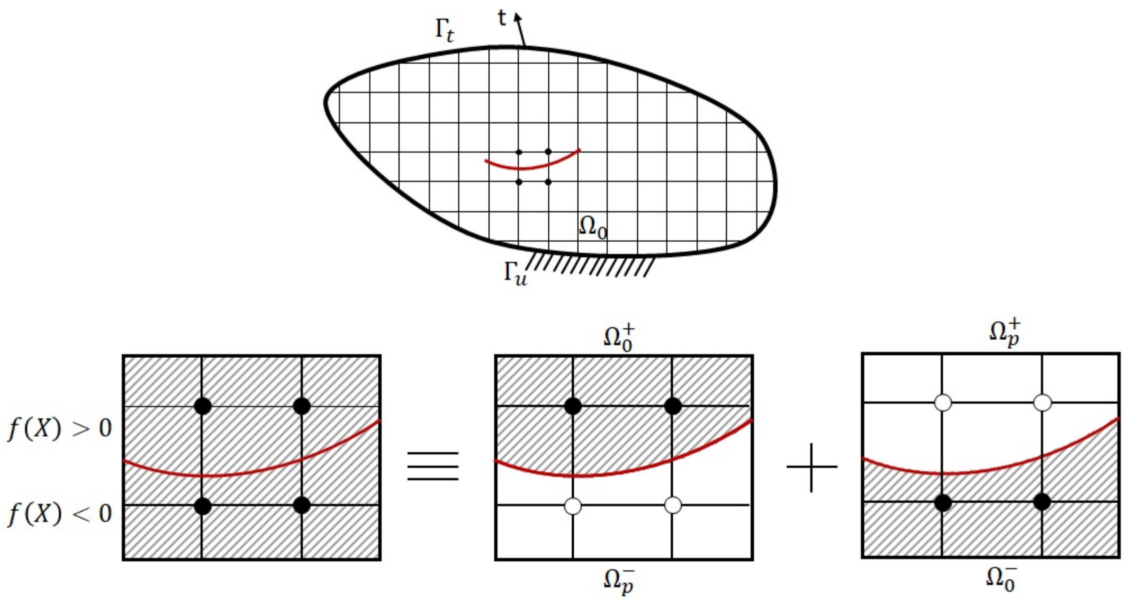

Figure 2.3: The principle of the phantom-node method. Figure is adapted from [16]

A discretized body which contains a discontinuity is shown in Figure 2.3. Furthermore, an element which is cut by the crack is shown. Ω_0 and Ω_p refer to real and phantom domains, respectively. The parts of the damaged elements which belong to the real domain Ω_0, is extended to the phantom domain Ω_p, to be able to interpolate the displacement in the Ω_0 by using the degrees of freedom of the phantom nodes in the Ω_p, which are presented empty circles in Figure 2.3. Phantom nodes are linked to corresponding real nodes as long as the enriched element is intact. When a crack cuts the element, it is separated into two parts each of which include phantom and real nodes, see Figure 2.3. The following expression given by Song [64] approximates the displacement field

$$\begin{aligned} u^h(X,t) = &\sum_{I \in (\omega_0^+, \omega_p^-)} u_I(t) N_I(X) H(f(X)) \\ &+ \sum_{J \in (\omega_0^+, \omega_p^-)} u_J(t) N_J(X) H(-f(X)). \end{aligned} \tag{2.16}$$

where $f(X)$ refers to the signed distance with respect to the crack and $H(x)$ refers to the the Heaviside enrichment function. ω_0^+, ω_0^-, ω_p^+ and ω_p^- are the nodes regard-

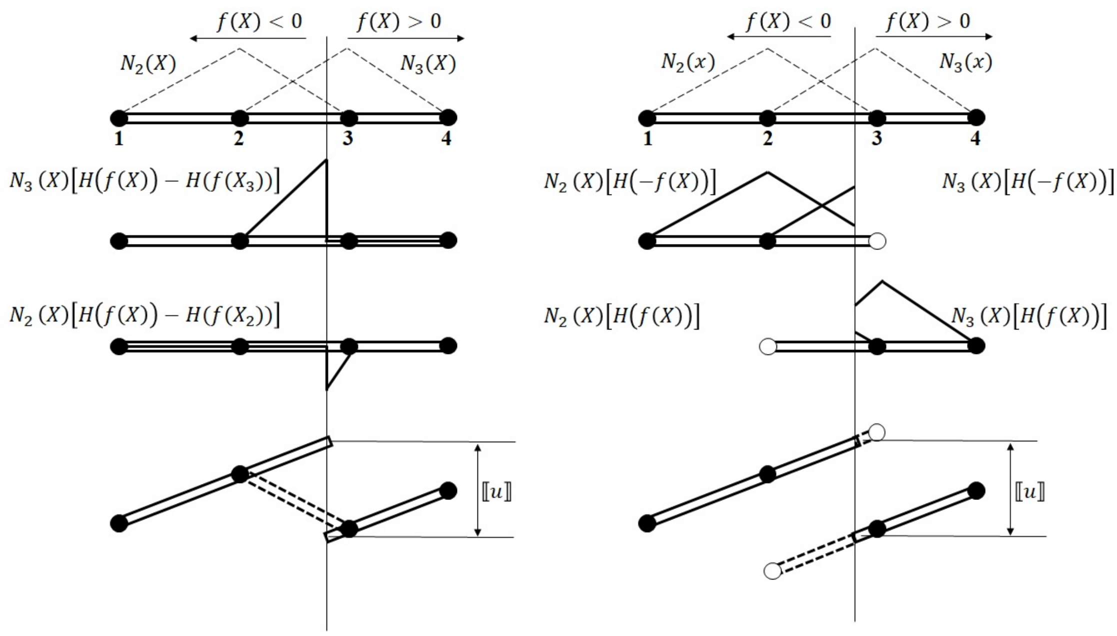

Figure 2.4: Classic XFEM and phantom-node method. Figure is adapted from [16]

ing to Ω_0^+, Ω_0^-, Ω_p^+ and Ω_p^-, respectively. The comparison of the shape functions between original XFEM and phantom node method is illustrated in Figure 2.4 for a one-dimensional phantom node superimposed element. By integrating over the area from the original nodes end up to the crack, i.e. Ω_0^+ and Ω_0^- the jump in the displacement field is accomplished [16].

Principally, if the equivalent strain energy release rate exceeds the critical strain energy release rate at the crack tip in an enriched element, the process of separation starts. Once this requirement has been met, every phantom node is no longer restricted to its corresponding original node, and thus, phantom nodes can freely move apart.

2.3.2 Level Set Method

The discontinuities are modelled almost independent of the finite element mesh in the XFEM framework. The issue is how to monitor the initiation and propagation of these discontinuities, as the the finite element mesh does not explicitly define them. In order to track cracks, voids and holes the level set method has been used which was initially introduced by Osher and Sethian [65] for tracking the development of moving boundaries and later it was used in XFEM. The narrow band level set method proposed by Adalsteinsson and Sethian [66] can be used to decrease the computational costs associated with the level set method.

The important point of the level set method is to treat to the interfaces as the zero level set of some functions [67]. In order to fully characterize a crack, two different level set functions are defined as follows

- A normal level set function, $\varphi(x)$
- A tangential level function, $\psi(x)$.

The normal level set function for a closed curve takes the following form

$$\varphi = (x - \overline{x}) \cdot n \tag{2.17}$$

where $\overline{x}$ which belongs to Γ_c given in Figure 2.5 is the closest point to an arbitrary point $x(x, y) \in \Omega$ and n describes the normal vector of $\overline{x}$.

For an interior crack, tangential level set function $\psi(x)$ is computed by finding the minimum signed distance to the normal at the crack tip and two different functions can be discriminated [14] which can be written as follows

$$\psi(x) = max\left\{\psi_1(x), \psi_2(x)\right\} \tag{2.18}$$

The tangential level set function ψ is used to track the crack surface, while the normal level set function φ is used to track the crack tip [68]. In conclusion, the normal and tangential level set functions are defined such in the following way

$$\begin{cases} \text{for} \quad x \in \Gamma_{cr} \quad \varphi(x=0) \quad \text{and} \quad \psi(x \leq 0) \\ \text{for} \quad x \in \Gamma_{tip} \quad \varphi(x=0) \quad \text{and} \quad \psi(x=0). \end{cases} \tag{2.19}$$

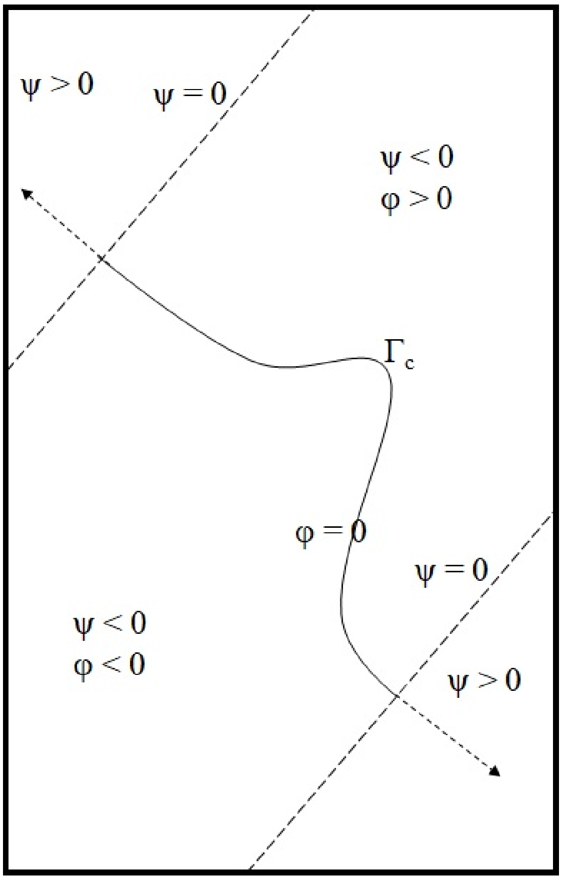

Figure 2.5: Construction of level set functions

2.3.3 Limitations of the XFEM in ABAQUS

Due to its recent introduction, there are some limitations [68] of XFEM implementation in Abaqus. The most significant ones are listed below;

- implemented only for the static stress analysis procedure
- can use only linear continuum elements
- contour integrals for stationary cracks not currently supported
- cannot model fatigue crack growth
- intended for single or a few non-interacting cracks in the structure
- an element cannot be cut by more than one crack
- crack cannot turn more than 90 degrees in one increment

- crack cannot branch
- the first signed distance function must be non-zero
- only frictionless small-sliding contact is considered
- only enriched regions can have a material model with damage

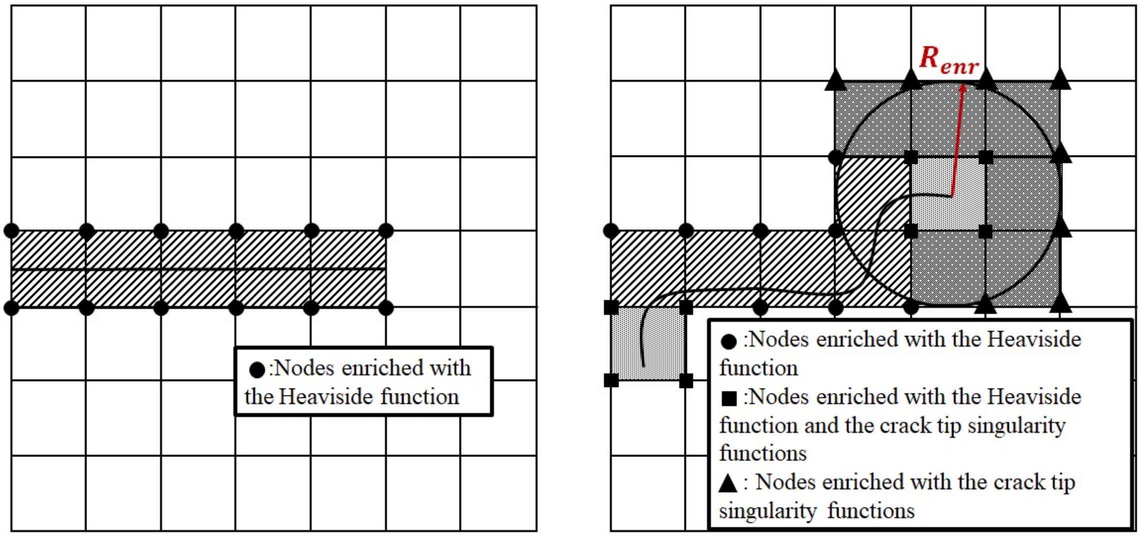

Figure 2.6: Abaqus/Standard enrichment procedure

Furthermore, the enrichment process of the nodes performed in Abaqus is of considerable interest. There are important differences for stationary and propagating cracks in XFEM implementation of Abaqus. In the first case, it seems evident that the crack can not propagate in the body, and only a static analysis can be performed. The crack tip can be located anywhere in an element domain for stationary cracks but it can only be located along an element edge for propagating cracks, because while crack propagates through the element it requires to cut the supporting domain of the element completely. Therefore, the crack tip of the propagating cracks can not be located arbitrarily in the element but only along an element edge. In other words, the crack tip cannot be located inside the element domain for propagating cracks.

There is a significant difference in the enrichment procedure between stationary and propagating cracks. To be more specific, the number of enriched nodes and the adoption of the enrichment functions are different for those two crack types. In propagating cracks, only Heaviside enrichment functions are governed, and as a consequence, the crack can be located everywhere in the finite element model while the crack tip itself has to lie on an element edge. On the contrary, for the stationary cracks, XFEM discretization consists of both the Heaviside and asymptotic near-tip singularity functions. According to Figure 2.6, the nodes of the elements divided by the crack entirely are enriched only with the Heaviside enrichment function, while the single element containing of the crack tip has its nodes enriched with the Heaviside function and asymptotic near-tip singularity functions. Abaqus allows the user to define the enrichment region, and it is illustrated in Figure 2.6 as R_{enr}. Increasing the number of enriched elements or in other words expanding the enriched area boundaries increase the accuracy of the finite element discretization and the computational cost as well.

CHAPTER 3

FINITE ELEMENT MODEL

In this chapter, the method followed in generation of FEM models of four-point bending experiments shown in Figure 3.1, is explained in detail. Damage parameters used in the XFEM enriched region for the crack initiation and the cohesive region for the delamination are explained. The procedure developed to assign random maximum principal stress (MAXPS) properties to the elements in the uppermost layer of the TC is presented. In order to verify the FEM models a mesh verification study is conducted, the details and the results of the this study are also explained.

3.1 Model

Two-dimensional finite element models of the symmetric four point bending experiments conducted in [1] are created. There are three different TBC specimens with different BC and TC thicknesses. The geometry and the coating thicknesses of three different specimens are given in Table 3.1.

Table 3.1: Substrate and coating thicknesses of the specimen

Specimen	**Top Coat [mm]**	**Bond Coat [mm]**	**Substrate[mm]**
Thick	0.60	0.16	1.60
Standard	0.38	0.10	1.60
Thin	0.26	0.05	1.60

Two-dimensional models are created, because of the limited computational resources and three-dimensional effects are considered to be negligible for the problem. In the

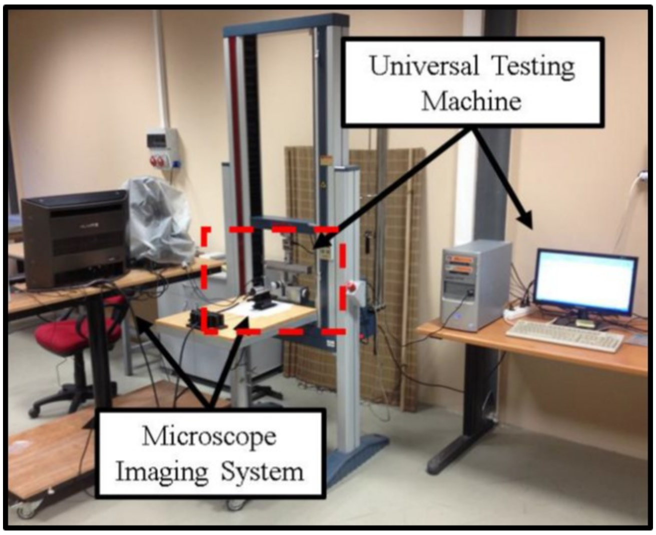

(a) Four-point bending test setup

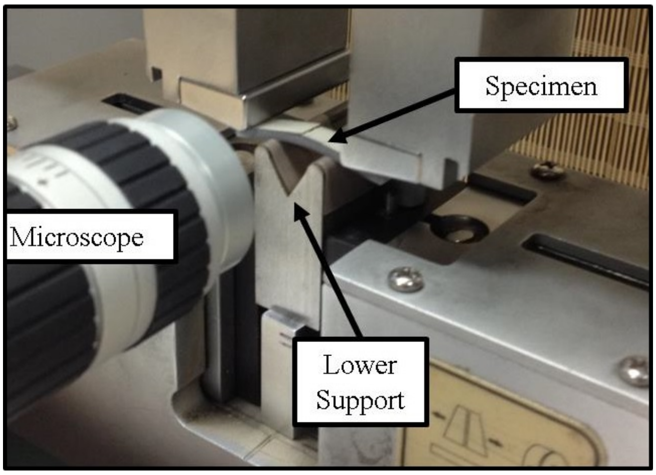

(b) close up view of the specimen tested

Figure 3.1: Experimental four-point bending setup [1]

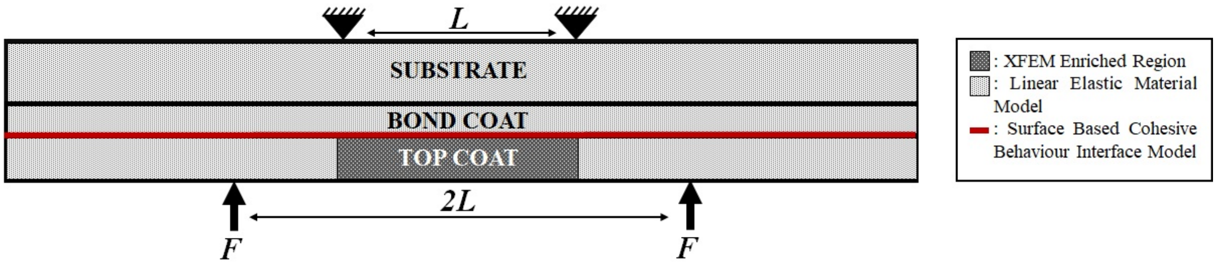

Figure 3.2: Schematic view of the finite element model of four point bending test

four point bending tests given in Figure 3.2, the substrate thicknesses are same for all three models, while BC and TC thicknesses vary. The models are constrained by four circular rigid bodies, the two of them are used to support the beam and the other two are used to apply the load. Frictionless contacts are used between the rigid bodies and the specimens. The rigid body supports are constrained with encastre boundary condition and a displacement controlled loading in y-direction is applied with two rigid bodies from the TC. When analyses have been run with these boundary conditions rigid body motion problems have been occurred. To overcome rigid body motion problem of the specimen in finite element analysis, an artificial boundary conditon which does not exist in the experiment is added to the model. The model is also constrained in the x-direction by adding an artificial boundary condition to the vertical axis in the middle of the substrate section, see Figure 3.3.

According to the deposition technique either air plasma spraying and electron beam vapor deposition residual stress occurring in the TBCs. The most important factor of the residual stress is the temperature at which the coating process is formed. Depending on the temperature and deposition technique the residual stress field varies from compressive to the tensile. In addition to these differences stress field can also vary in the thickness direction. Generally stress is higher at the surface close to the substrate comparing to the outermost surface of the coating [69]. In this study, residual stresses are not taken into account.

Four node plane strain elements with reduced integration (CPE4R) are used throughout the model. In the TC and the BC 0.05 mm mesh size is used. In substrate layer of the model mesh size varies through the thickness direction and increases from 0.05

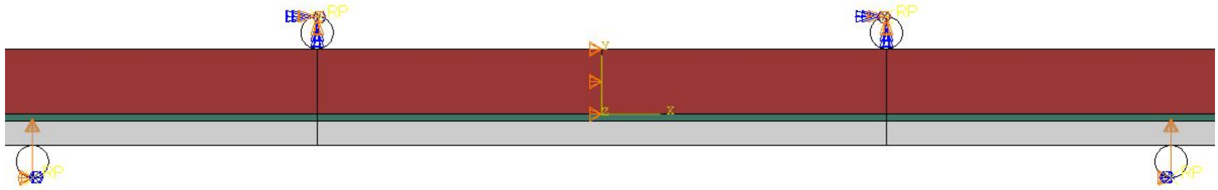

Figure 3.3: Boundary conditions of the finite element model

mm up to 0.2 mm. The employed mesh sizes are determined by a mesh convergence study explained in Section 3.2.

3.1.1 Material Properties

Table 3.2: Material Properties

Layer	E [GPa]	ν [-]	MAXPS [MPa]	$G_{critical}$[kJ/m^2]
Substrate (Inconel 718)	205	0.284	-	-
Bond Coat (NiCrAlY)	115	0.3	-	-
Top Coat (YSZ)	45	0.157	1000	8

Material properties given in Table 3.2 are taken from the literature [1] except the Young's modulus of the TC. The Young's modulus of the top coat layer is calculated by nanoindentation test in [1] as 118 GPa with a 17 GPa standard deviation. On the other hand [70] conducted cantilever beam experiments for similar systems. Since the bending experiments for the determination of the Young's modulus is more relevant for the problem considered in this study, the Young's modulus of 45 GPa found in [70] is used.

3.1.1.1 Damage Properties for the XFEM Region

In Abaqus XFEM, damage initiation and propagation criteria have to be assigned to the material model to be able to observe expected crack initiation and propagation phenomenon. In order to predict the expected damage initiation in the region which consists of XFEM enriched elements, the Abaqus/Standard User's Manual [17] recommends to implement in material specifications either the ***Maximum principal stress damage criterion*** (MAXPS) or the ***Maximum principal strain damage criterion*** (MAXPE). In this study, the first criterion has been utilized. The maximum principal stress criterion can be represented as

$$f = \left\{ \frac{\langle \sigma_{max} \rangle}{\sigma^o_{max}} \right\}. \tag{3.1}$$

In other words, MAXPS criterion assumes that a crack will nucleate within the body once the ratio reaches a value equal to 1. In Equation (3.1), σ^o_{max} represents the maximum allowable principal stress, while σ_{max} is the maximum principal stress. The symbol $\langle\rangle$ indicates the Macaulay brackets, used to signify that a purely compressive stress state does not lead to any damage initiation [14],[17].

The Maximum Principal Stress Criterion (MAXPS) is used as a damage initiation criterion for the failure model of the YSZ in the XFEM enriched region. The parameter MAXPS is determined according to the experimental results of [1] and it is adjusted by iterations based on the crack nucleation times found in experiments. The bending tensile strength is calculated by [71] as 1000 MPa for 3YSZ and the results of the iterative study is validated for 3YSZ. The porosity of TBC coatings is one the most important properties, see [72]. To model the porosity or micro cracks in the YSZ a script is written and MAXPS value of uppermost layer elements is fluctuated around 1000 MPa by this script. The script randomly distributes MAXPS parameter in user-defined limits in the uppermost layer elements of the TC layer.

3.1.1.2 Damage Properties for the Cohesive Region

The beginning of degradation process of the cohesive response at contact surfaces, in other words damage initiation, begins when the criterias defined by user either as contact stresses or contact separations are satisfied. In Abaqus several damage initiation criteria exist.

The damage initiation criterion given in Equation (3.2) and the damage evolution law used in surface-based cohesive behavior are very similar to those used for cohesive

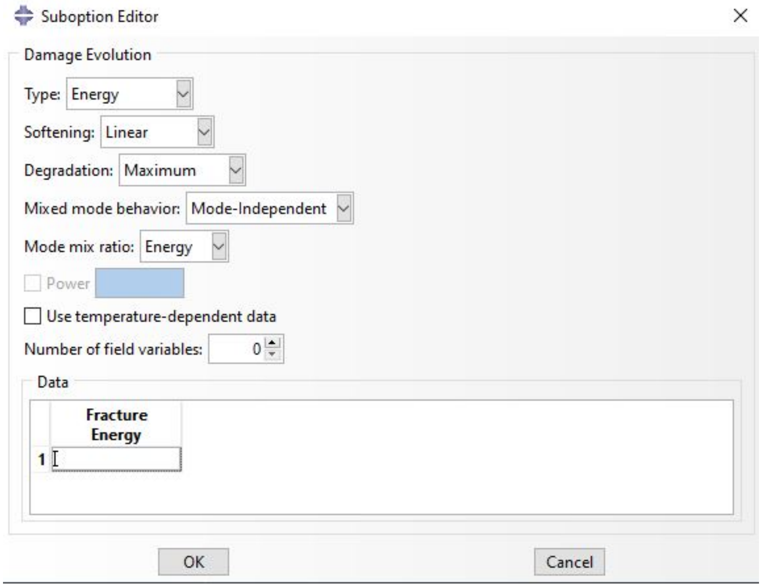

Figure 3.4: Damage evolution for XFEM region in Abaqus

elements with the traction-separation constitutive model. A linear elastic traction-separation behavior, relates the normal and shear stresses to the normal and shear separations across the interface before the initiation of any damage. The damage evolution describes the degradation of the cohesive stiffness.

The Maximum Stress (MAXS) damage initiation criterion given in Equation (3.2) is used in this study.

$$max\left\{\frac{\langle t_n\rangle}{t_n^o}, \frac{t_s}{t_s^o}, \frac{t_t}{t_t^o}\right\} = 1 \tag{3.2}$$

In Equation (3.2) t_n describes the normal contact stress in the pure normal mode, t_s describes the shear contact stress along the first shear direction and t_t is the shear contact stress along the second shear direction [17].

3.1.1.3 Damage Evolution

Once the damage initiation criterion is satisfied and the damage process is started, the degradation rates of the stiffness of the material and the cohesive surface are defined by the damage evolution law [17].

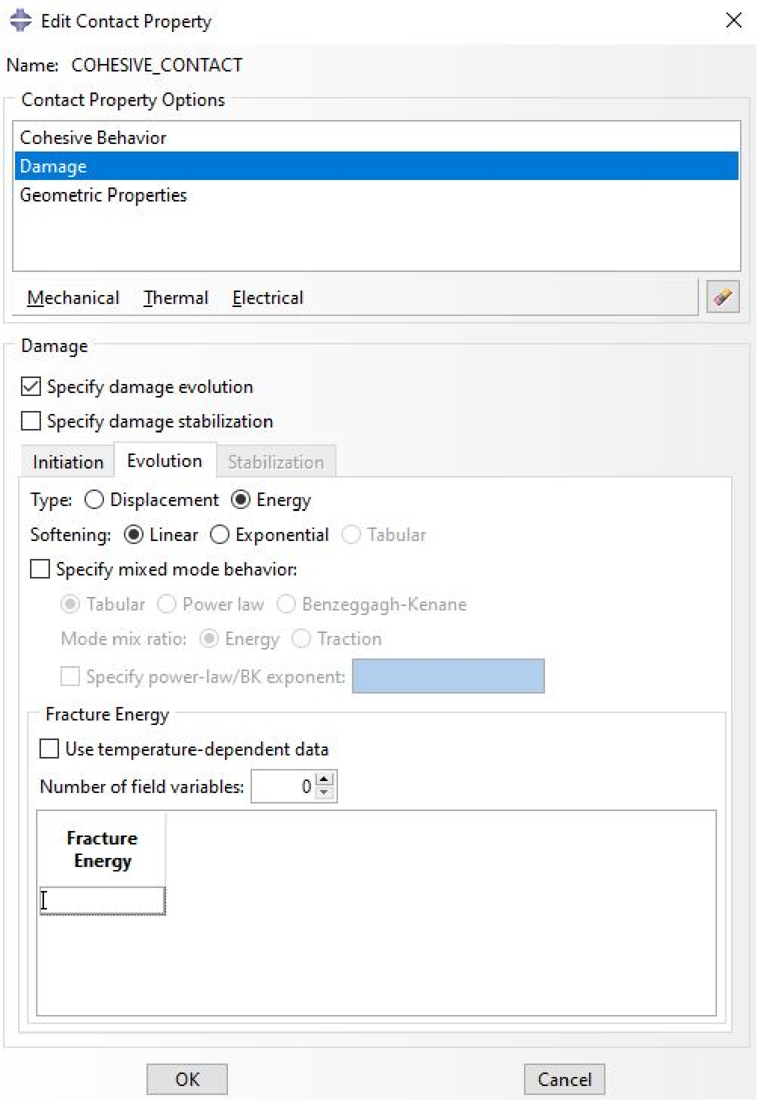

Figure 3.5: Damage evolution for cohesive surface in Abaqus

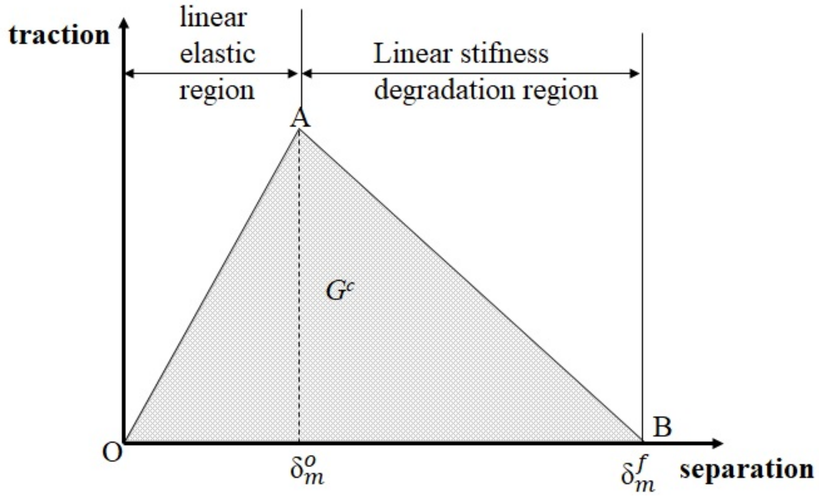

Figure 3.6: Linear damage evolution. Figure is adapted from [17]

There are two components to the definition of damage evolution. The first component involves specifying either the effective separation at complete failure, δ_m^f , relative to the effective separation at the initiation of damage, δ_m^o; or the energy dissipated due to failure, G^c, see Figure 3.6.

Damage evolution can be defined based on the energy that is dissipated as a result of the damage process, also called the fracture energy. The fracture energy is equal to the area under the traction-seperation curve, see Figure 3.6. The fracture energy is specified as a property of the cohesive interaction and either a linear or exponential softening behaviour could be chosen. Abaqus ensures that the areas under the linear or the exponential damaged response is equal to the fracture energy [17].

In this study damage evolution parameter is assigned both to the XFEM region elements in the TC layer as a material property and the cohesive surface between the TC and BC layer as a contact property. In Figure 3.4 and 3.5 selection menus in the Abaqus user interface both for the YSZ and cohesive contact property are given.

3.1.2 Randomness

After some initial simulations of four point bending tests in Abaqus by using the XFEM, cracks are initiated and propagated. However, the cracks initiated almost at all

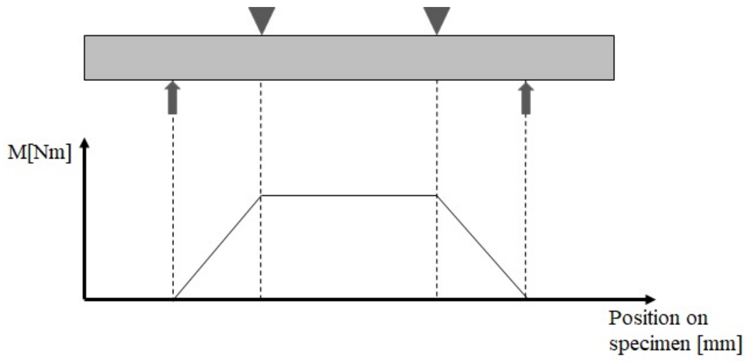

Figure 3.7: Four point bending moment distribution

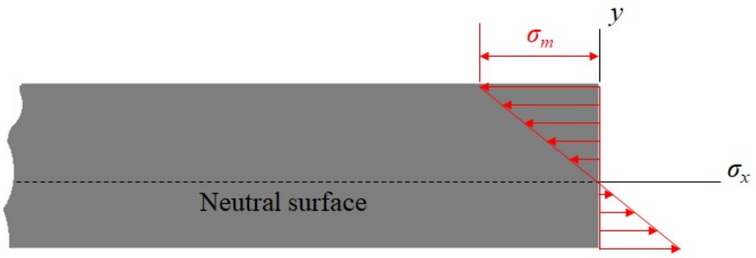

Figure 3.8: Bending stresses

elements of the uppermost layer of the top coat simultaneously, see Figure 3.11. This result is indeed expected because Abaqus is working according to the user defined damage initiation criterion. The XFEM enriched region which is shown in Figure 3.2 in the top coat is modelled as homogeneous and the damage initiation criteria is set to a single value for the whole region.

In the four point bending tests pure bending condition occurs and the bending moment is constant between the loads, see Figure 3.7. Therefore, the maximum tensile stress is at the uppermost part of the top coat region. Pure bending is a stress state in which a bending moment is applied to a beam without axial, shear, or torsional forces being present simultaneously [73]. The bending stress state of the beam is shown in Figure 3.8 and the equation of the normal stress σ_x is as follows;

$$\sigma_x = -\frac{y}{c}\sigma_m \tag{3.3}$$

In Equation (3.3) σ_m denotes the maximum absolute value of the stress. This equation

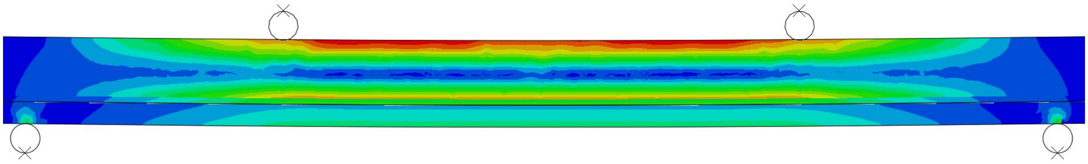

Figure 3.9: Stress distribution of the four point bending test

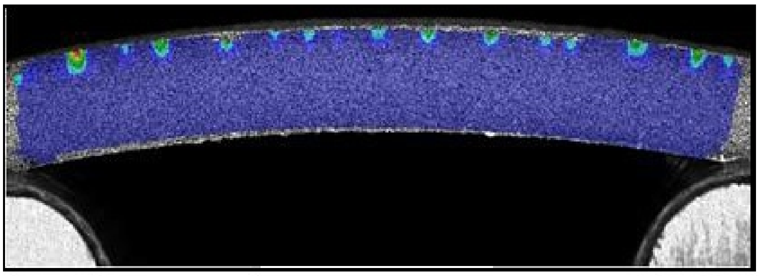

Figure 3.10: Crack initiations at the top coat of the TBC specimen in the literature [1]

shows that, the normal stress varies linearly with the distance from the neutral surface and it reaches the maximum value at outermost surface [73].

$$\sigma_m = \frac{Mc}{I} \tag{3.4}$$

Equation (3.4) shows σ_m is inversely proportional to the ratio $\frac{I}{c}$ which is called the elastic section modulus. I is the moment of inertia, or second moment, of the cross section with respect to a centroidal axis perpendicular to the plane of the couple M. Note that the ratio depends only upon the geometry of the beam cross section.

According to the Figure 3.7 and Equation (3.4) maximum tensile stress occurs at the outermost surface of the beam between supports where the moment is constant and maximum. It is also seen in finite element results in Figure 3.9 as well. Therefore the results shown in Figure 3.11 are expected because the same MAXPS value is assigned to every element in the XFEM enriched region and once the stress value reaches the assigned value cracks nucleate and start to propagate.

However, the results in the literature [1], see Figure 3.10, are not similar to the initial FEM results. A certain amount of spacing is seen between two adjacent cracks in experimental results in the literature [1]. Unlike the experiments, in FEM anal-

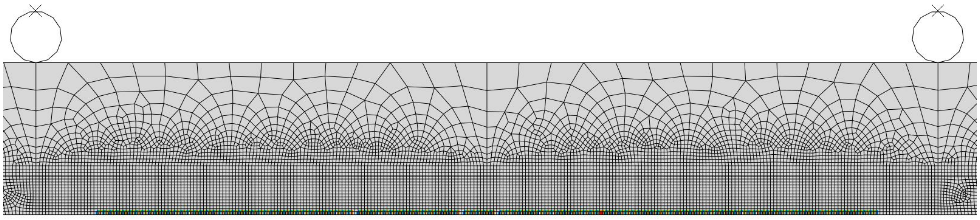

(a) Cracks initiation

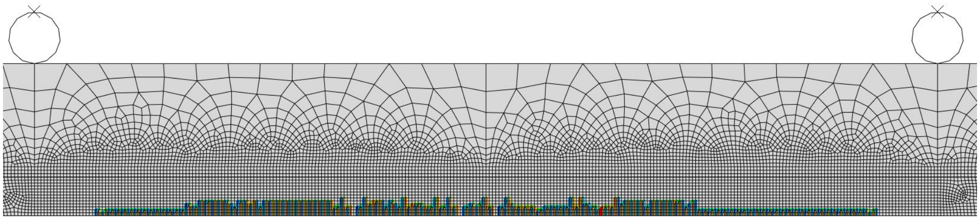

(b) Cracks propagation

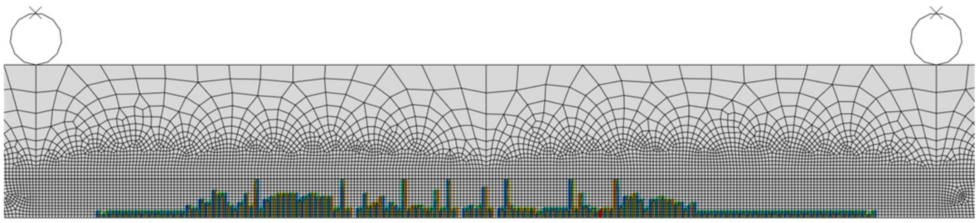

(c) Cracks reach interface

Figure 3.11: Crack initiations in homogeneous model

ysis cracks initiate almost in every element at the outermost layer, see Figure 3.11. Considering the Abaqus XFEM damage initiation logic and the theory of four-point bending tests, simultaneous crack initiations is expected at the outermost layer elements of constant moment region of TBC specimens. Furthermore, assigning same MAXPS value to every element is not realistic because of the nature of the ceramic material. 3YSZ is not homogeneous and the porosity is one of the most common sources of inhomogeneity in ceramics, see [72].

Therefore, a script is written and the damage initiation property of the uppermost layer element of the top coat is manipulated. By this script MAXPS parameter is fluctuated around a nominal value.

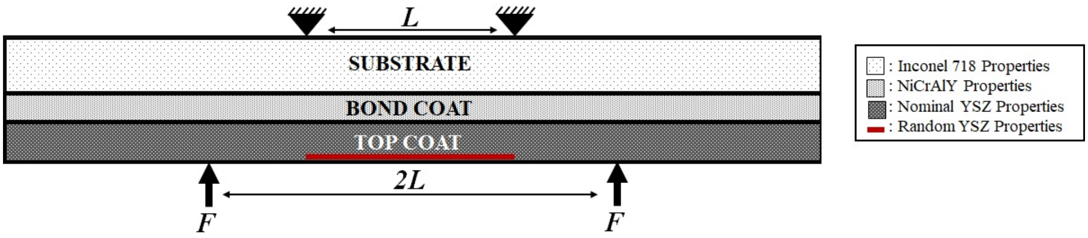

Figure 3.12: Material properties assignment diagram of FEM models

3.1.2.1 MAXPS Variation Procedure

By default, when a job is submitted associated with a model for analysis, Abaqus/-CAE generates an input file representing the created model and then Abaqus analyzes that input file. Input file of the Abaqus is written in ASCII format and can be viewed and edited using a text editor [17]. In addition, the contents of the input file can be modified externally. For example, the magnitude of the load applied, material properties, element types assigned in the model can be changed by editing the input file. By importing the edited input file Abaqus analyzes the model according to the edited features. In this study input files of the generated models are modified according to the procedure explained as follows;

- 2D planar, deformable, shell geometries are created for substrate, bond coat and top coat separately in Abaqus/CAE. For the geometrical dimensions of the TBC layers, specimen dimensions in the literature [1] are used and the geometrical dimensions of the specimens are given in Table 3.1.
- Different materials are created according to the material properties given in the literature [1], see Table 3.2. Inconel 718 properties are assigned to the substrate material and NiCrAlY properties are assigned to the bond coat material. However, because of the problem mentioned in the Section 3.1.2 two different materials are created for the top coat layer. One of them is for the outermost layer elements and the other one is the remaining elements at the top coat except the outermost layer elements between the loading supports, see Figure 3.12.
- Different sections are created for every layer to be able to assign different material properties for the created geometries. For substrate and bond coat layers

this procedure is pretty straightforward and easy. Then, created sections are assigned to the substrate and bond coat part.

- For the top coat layer randomly some finite elements are selected from the outermost layer to create section from these elements. Then, remaining elements are selected to create second section. This step is done to open an interface for the script to be able to edit the input file of Abaqus.
- Then the model is created and input file is generated by Abaqus/CAE.
- The input file of the model can be read and edited by the written script and the coordinates of elements can be determined. According to the element coordinates, outermost layer elements can be extracted and the initially assigned material properties can be edited.
- New materials and sections are created in the number of outermost layer elements of the top coat.
- MAXPS parameter is fluctuated in the user defined limits randomly and random MAXPS parameter is assigned to the elements at the outermost layer of the top coat.

3.2 Mesh Verification

One of the main objective of this study is to simulate the variation of the crack spacing with the thickness of TC. This variation was reported in the literature [1]. To verify the finite element model and to decide the mesh size different mesh densities are used in simulations and the results are compared.

As it is explained in the Section 3.1.1.1 maximum stress and the maximum moment occurs in the uppermost layer between the supports in the four-point bending tests. It is also seen in the experiments [1] that cracks are only initiated in this region. Therefore, the most significant area of the beam is the middle region of the TC layer between the loads, so only elements in this region are enriched for the crack initiation and propagation, see Figure 3.13.

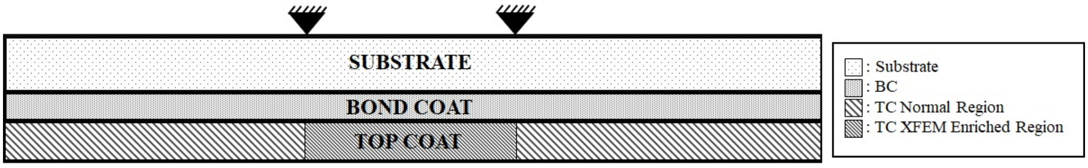

Figure 3.13: Mesh density map of the FEM model

Table 3.3: Number of elements for different mesh densities

Mesh Density	**Substrate**	**BC**	**TC Normal Region**	**TC XFEM Enriched Region**	**Total**
Coarse	1538	514	899	980	3931
Medium	4114	1378	1794	3640	10926
Fine	10417	4998	3630	14000	33045

In order to reduce the computational cost finer and structured meshes are assigned only in this related region. In adjacent regions of the top coat a biased mesh is assigned. The same technique is used in the bond coat layer of the model as well. In the substrate layer, whole region is assigned with a biased mesh and the concentration is reduced from the bond coat interface through the bottom surface which supports the loads. This approach is followed for different mesh densities in the mesh verification study and the rest of this study as well.

The distance L between the supporting points, see Figure 3.12, is 14 mm. In the coarse mesh model, 0.1 mm sized square shaped, structured elements are used. Consequently, 140 elements in the longitudinal axes of the beam are created between supporting points at the outermost layer of the elements. For the medium mesh, the size of the meshes in this region is halved and the number of elements at the outermost layer of the mesh is doubled to 280. For the fine mesh, the size of the elements is further halved again and the number of elements at the outermost layer is doubled compared to medium mesh. Total number of elements of each FEM model are given in Table 3.3.

As it is explained in Section 3.1.2, for the crack initiation MAXPS parameter is assigned to the elements at the outermost layer randomly in user defined limits. In this

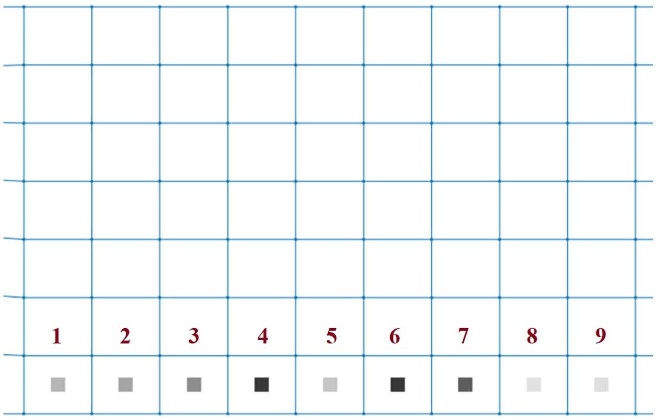

(a) Coarse mesh

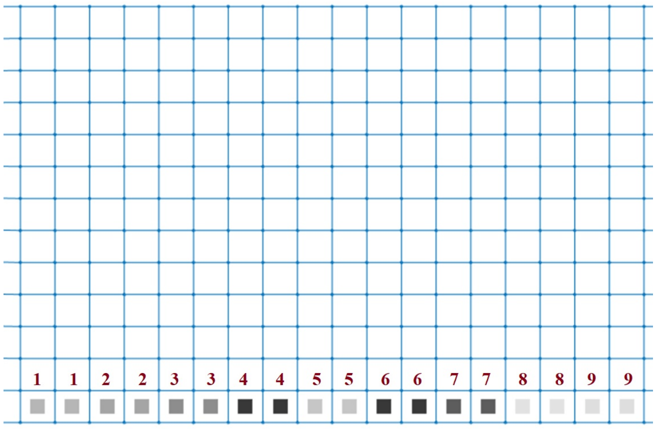

(b) Medium mesh

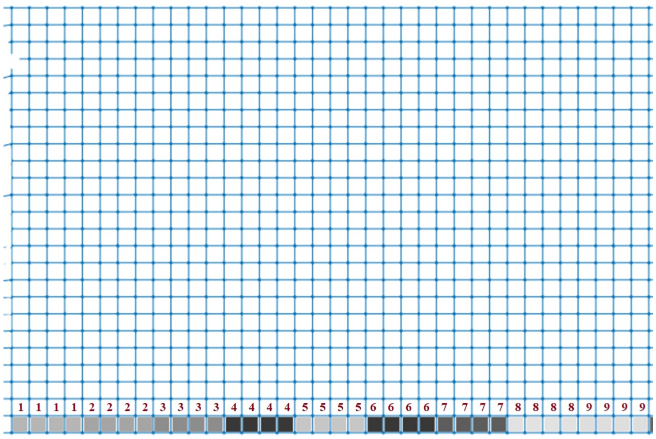

(c) Fine mesh

Figure 3.14: Variation of the MAXPS parameter of the elements in the outermost layer of models with different mesh densities

way it was intended to see average crack spacing change with the changing thicknesses of the TC. However, creating different mesh density models would cause a problem; since there is different number of elements in the models with different mesh densities, the random MAXPS parameter assigned to these outermost layer elements would also have a different number. This would change MAXPS variation pattern for different mesh densities. Therefore, the script is modified to assign same MAXPS parameter for the same region in different mesh density models.

It is started with the coarse mesh model which has 140 elements in the longitudinal axes between the supporting loads. This means that 140 different random MAXPS parameter in the user defined limits should be created. For the medium mesh density model as it is explained previously, this number increases to 280. In order to keep the same damage initiation parameters at the same coordinates in each model; MAXPS parameters assigned to 140 elements of the coarse mesh density model randomly and the same MAXPS values are assigned to two adjacent elements in the medium density mesh. Similarly, the same MAXPS values are assigned to four adjacent elements in the fine mesh, see Figure 3.14.

In Figure 3.14 different mesh densities are seen, and the meshes are drawn by the script written in MATLAB. Squares in the elements at the outermost layer refers to different MAXPS values. Colour scale of the squares is chosen such that lighter color tones like gray to white refer to higher MAXPS values and darker color tones like gray to black refer to lower MAXPS values. The numbers above the outermost layer elements in Figure 3.14 represents the order of the random MAXPS number. Considering the element sizes for different mesh densities, same regions in every model are assigned to the same MAXPS values by applying this method.

In order to check the validity of FEM models, 4 different random patterns of MAXPS are assigned to each different density and hence 12 models are created in total for mesh verification analyse. Cohesive surface approach also applied every model and XFEM and CZM used together. These two methods requires high computational power even they are used separately because of the number of the cracks initiation and propagation in the TC layer. Furthermore, the combination of the two methods requires even higher computational power, considering the delamination at the inter-

Table 3.4: Number of cracks for different mesh densities

Model Number	Coarse	Medium	Fine
Model - 1	6	5	No converged
Model - 2	5	6	9
Model - 3	6	6	5
Model - 4	6	6	6
Average	**5.75**	**5.75**	**6.67**

face between TC and BC.

Variation of average crack spacing with the TC layer thickness change is one of the outputs of the four-point experiments in the literature [1]. Therefore, in the mesh verification study variation of the average crack spacing among different meshes is investigated. Only cracks that reach to the interface between the TC and the BC layers were counted as cracks in this study. Results of the mesh verification study is given in Table 3.4. The crack patterns for Model-3 and Model-4 for different mesh densities are given in Figure 3.16 and Figure 3.17, respectively.

The load-displacement behaviour of the different mesh densities are compared in Figure 3.15 and all three meshes are in a good agreement with each other.

The number of cracks results of the coarse and medium meshes are in good agreement with each other. However, the second model with fine mesh density shows different behaviour compared to medium and coarse meshes, in the fine mesh of the second model more cracks initiate. On the other hand, the fine mesh of the fourth model has a good agreement with the coarse and medium mesh density models. Furthermore, convergence issues raised during the analysis of the fine mesh models which requires more computational resource compared to medium and coarse meshes. For these reasons, it would not be reasonable to continue with the fine-mesh models for the rest of this study.

Even though the coarse and the medium mesh density models are in good agreement in terms of the average crack spacing, the medium mesh density model is chosen for the rest of the study because of the geometrical sizes, see Table 3.1, of different

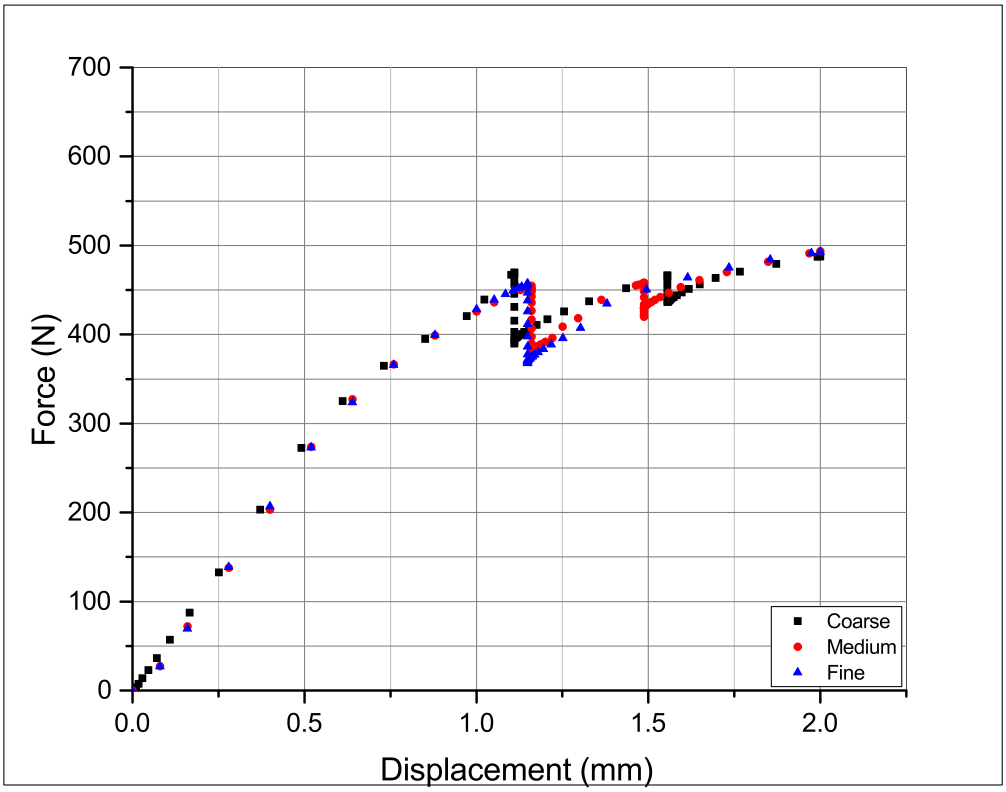

Figure 3.15: Load-displacement behaviour comparison of different mesh densities

layers in different TC thickness models. In the thin specimen the BC layer is thinner compared to the standard and the thick specimen. Therefore, employment of the coarse mesh would lead to aspect ratio differences between the TC and the BC layer elements and this could effect the reliability of the results. Even though it has an advantage for the run times of the analyses medium mesh model is a better choice.

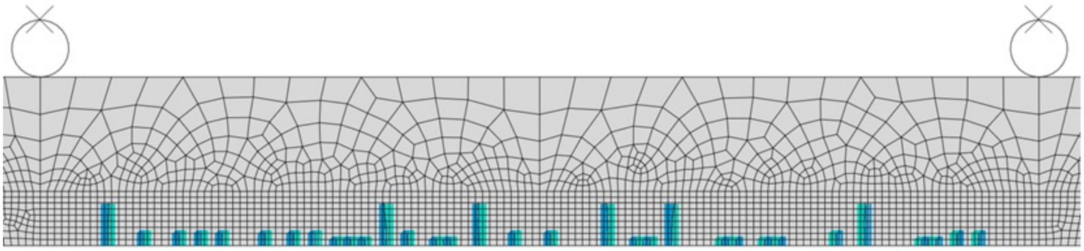

(a) Coarse mesh Model-3 results

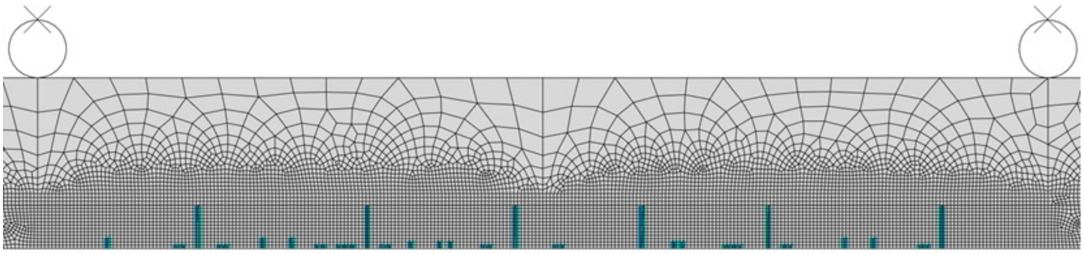

(b) Medium mesh Model-3 results

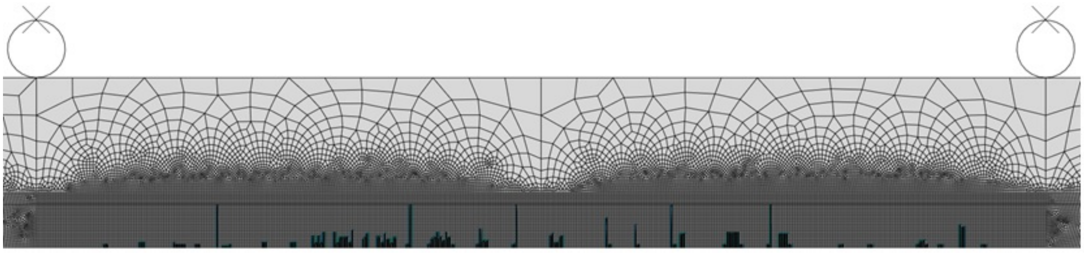

(c) Fine mesh Model-3 results

Figure 3.16: Model-3 results with different mesh densities

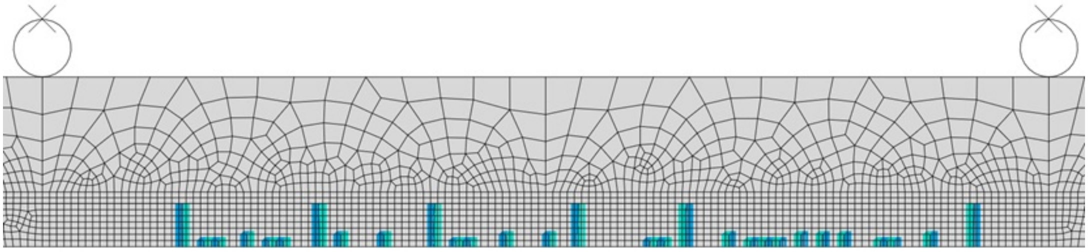

(a) Coarse mesh Model-4 results

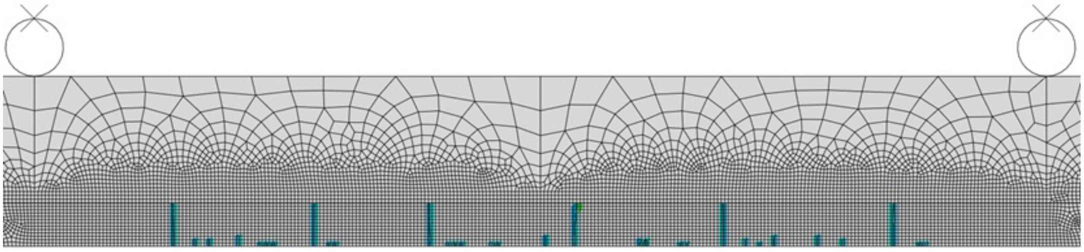

(b) Medium mesh Model-4 results

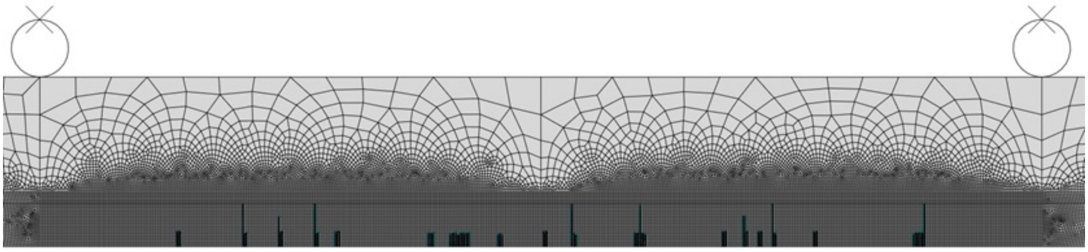

(c) Fine mesh Model-4 results

Figure 3.17: Model-4 results with different mesh densities

CHAPTER 4

NUMERICAL RESULTS

In this chapter, TBC specimens with different thicknesses are analyzed under a displacement controlled four-point bending test by using an approach that combines the XFEM and the CZM. An artificial parameter is created in order to constitute randomness effect of the ceramic material used at the TC layer. Numerical results of the parametric studies for the cohesive zone at the TC/BC interface and the TC layer are presented and the fracture mechanism of the TBCs are investigated numerically. The results of the study are compared with the experimental results in the literature [1].

4.1 Effect of the Cohesive Stiffness

The cohesive surface behaviour is used at the interface between the TC and BC layers instead of cohesive elements to simulate the degradation of the interface, as it is described in Chapter 3. The cohesive zone method enables the initiation and propagation of the delamination at the interface. In Abaqus there are two options to model constitutive response of the cohesive zone:

- Traction-separation approach
- Continuum approach

the continuum approach is used if the actual thickness of the interface is modelled, contrarily the traction-separation approach is used when the interface thickness is modeled as zero. In this study, the thickness of interface between the TC and the BC considered as zero [74].

The traction-separation relationship at the interface is characterized by three critical parameters;

- Cohesive stiffness
- Damage initiation threshold
- Damage evolution parameter

The initial stiffness value of the cohesive interface between the TC and the BC layers is accepted as a penalty parameter in Abaqus and it is not a measurable physical parameter. Preferably the cohesive stiffness value should be very large even it should be infinity. However, in FEM models a sufficiently high but a finite value must be assigned to the cohesive surface stiffness. It is important to note that a very high value of stiffness may result in convergence problems [74]. Thus, the interface stiffness should be large enough to prevent an artificial compliance but also small enough to reduce the risk of numerical problems such as spurious oscillations of the tractions at the interface [75].

Abaqus allows user to assign cohesive surface stiffness as an uncoupled or coupled relationship between tractions and separations. In the literature, for cohesive zone problems generally uncoupled relationship is chosen unless there is a data set available for the coupled elastic response. Therefore, in this study uncoupled relationship is chosen for the cohesive zone stiffness. The uncoupled relationship in Equation (2.15) becomes the following

$$t = \begin{Bmatrix} t_n \\ t_s \\ t_t \end{Bmatrix} = \begin{bmatrix} K_{nn} & 0 & 0 \\ 0 & K_{ss} & 0 \\ 0 & 0 & K_{tt} \end{bmatrix} \begin{Bmatrix} \delta_n \\ \delta_s \\ \delta_t \end{Bmatrix} = K\delta \tag{4.1}$$

where K_{nn}, K_{ss}, K_{tt} refer to the normal, the shear and the second shear stiffness components. By default, the normal and tangential stiffness components are not coupled: pure normal separation by itself does not give rise to cohesive forces in the shear directions, and pure shear slip with zero normal separation does not give rise to any cohesive forces in the normal direction [17]. In our problem Mode-I fracture

Table 4.1: Cohesive Stiffness Iterations for Thin Model

THIN						
Cohesive Stiffness	**Model - 1**		**Model - 2**		**Model - 3**	
[kN/mm^3]	**Small Cracks**	**Int. Cracks**	**Small Cracks**	**Int. Cracks**	**Small Cracks**	**Int. Cracks**
200	6	8	10	7	8	7
300	9	8	11	7	8	7
400	9	8	11	7	10	7
500	9	8	11	7	10	7
600	10	7	12	7	10	7
800	10	8	11	9	11	7
1000	8	9	9	10	11	7
1200	9	8	12	7	11	7

is dominant at the interface between the TC and the BC layers and delamination is investigated in the experiments [1]. Therefore, it is assumed that the normal and the shear stiffness components are equal to each other and the same values are assigned to K_{nn} and K_{ss} in all analyses.

Analysis are started to set the cohesive zone stiffness value for the rest of the study. Three different models are created according to the procedure given in Section 3.1.2.1. For every TC and BC thickness values those three models with different MAXPS distribution patterns are used in the analyses. In the analyses all the material parameters other than the cohesive stiffness are fixed to investigate the effect of the cohesive stiffness on the results. Furthermore, $\pm 3\%$ variation of MAXPS parameter is used.

One of the main output of the experiments [1] is the variation of the average crack spacing for different thickness specimens. Although the delamination and cracking mechanisms of the TBCs are also investigated in the experiments [1] at this stage of the current numerical study the delamination is not considered. To prevent the damage initiation at the interface a very high value of 2000 MPa is chosen for MAXS parameter which describes the cohesive strength.

It is aimed to see that the number of cracks at the TC layer is not affected by the change of the cohesive stiffness values. In the literature, very large values of cohesive stiffness, 3–4 orders of magnitude larger than the Young's modulus of the neighbouring bulk materials are recommended [76]. Therefore, the analysis is started with the

Table 4.2: Cohesive Stiffness Iterations for Standard Model

STANDARD						
Cohesive Stiffness	**Model - 1**		**Model - 2**		**Model - 3**	
[kN/mm^3]	**Small Cracks**	**Int. Cracks**	**Small Cracks**	**Int. Cracks**	**Small Cracks**	**Int. Cracks**
200	9	6	14	7	13	6
300	10	6	14	8	15	6
400	10	6	14	8	15	6
500	10	6	14	8	15	6
600	11	6	14	8	15	6
800	11	6	14	8	15	6
1000	11	6	14	9	15	6
1200	11	6	14	9	15	6

relatively high values as recommended. However, when large values are assigned to K_{nn} and K_{ss} parameters numerical instabilities and convergence issues experienced especially in thick model.

In order to overcome this problem, the analysis are continued by decreasing the K_{nn} and K_{ss} values to one order of magnitude larger than the Young's modulus of the BC layer and convergence is satisfied in thin and standard models but instabilites and convergence issues are not solved in the thick model. The stiffness values are decreased one order of magnitude more and convergence is achieved for the each thickness. As it is mentioned in the literature [75], the cohesive stiffness values should be selected as high as possible while convergence can still be achieved. Therefore, the analyses are continued by increasing the stiffness until convergence problem is occurred.

Table 4.1, 4.2 and 4.3 show the number of cracks obtained in the analyses. Number of small cracks are also given in the tables but for average crack spacing calculation number of all cracks are not taken into account as in the experiments [1], only the cracks that reach to the TC/BC interface which are given in the tables as "Int. Crack" columns are counted as cracks. The number of crack results are very consistent for the standard model for the considered range of cohesive stiffness values. Even though the number of cracks results show some variations for the thin model. In most cases there is a tendency of rise in number of cracks with an increase of cohesive stiffness.

Table 4.3: Cohesive Stiffness Iterations for Thick Model

THICK						
Cohesive Stiffness	**Model - 1**		**Model - 2**		**Model - 3**	
[kN/mm^3]	**Small Cracks**	**Int. Cracks**	**Small Cracks**	**Int. Cracks**	**Small Cracks**	**Int. Cracks**
200	31	6	27	5	30	5
300	29	6	27	5	29	6
400	31	6	28	5	29	6
500	7	6	27	7	7	6
600	N/A	N/A	28	6	1	5
800	N/A	N/A	N/A	N/A	28	6
1000	4	4	N/A	N/A	28	6
1200	N/A	N/A	25	6	27	5

However, it is not the case for the thick model and convergence problems are experienced for large interface stiffness values. Therefore, 500 kN/mm^3 is chosen as the cohesive interface stiffness value for the rest of the study for all models. Although the units of the cohesive stiffness and the Young's modulus are not comparable, selected K value is one order of magnitude higher than the Young's modulus of the TC layer and five times higher than the Young's modulus of the BC layer numerically.

One can conclude that the cohesive stiffness value is not the most important parameter for the traction-separation relation for the crack initiation and propagation.

4.2 Effect of the Maximum Principal Stress (MAXPS) Parameter

In Abaqus, the crack initiation in the XFEM enriched region elements is based on the stress or the strain value at the center of the enriched element. As it is mentioned in Section 3.1.1.1, MAXPS parameter is chosen for the prediction of the crack initiation in the TC of the TBCs.

The FEM model created for the simulation of the experiments in [1] is a complex model because it is a composite beam consisting of three different materials with different thicknesses and different material parameters. Note that crack initiations and propagations are expected only at the TC layer of TBC beams. The TC layer of the TBC is almost three times thinner than the substrate for the thick model and this

Table 4.4: ASTM A109 Steel material properties for a XFEM study

ASTM A109 Steel			
Yield Strength [MPa]	305.3	**MAXPS Damage**	Maximum Principal Stress: 345 MPa
Ultimate Tensile Strength [MPa]	437.7	**Damage Evolution**	Type: Energy
Young's Modulus [GPa]	204.8		Softening: Linear
Strain at Ultimate Failure [-]	18.0		Degradation: Maximum
Poisson's ratio [-]	0.29		Mode mix ratio: Mode-Independent
			Fracture Energy: 5.3 kN/m

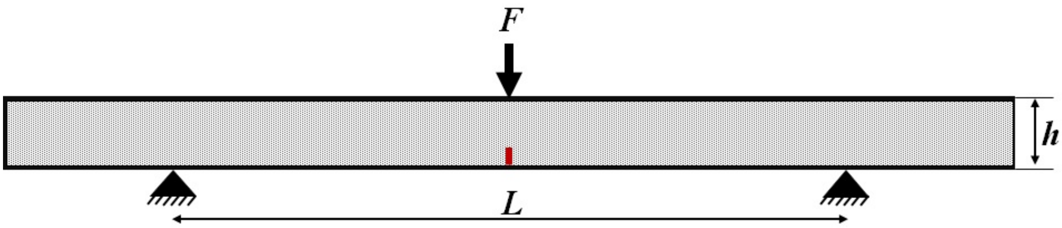

Figure 4.1: Finite element model of the three-point bending

ratio is higher for the standard and the thin models. Furthermore, it has a modulus of elasticity almost five times smaller than the substrate material. There is also a cohesive surface at the interface between the TC and the BC layer which increases the complexity of the model. Therefore, investigating the load-displacement behaviour and getting comparable results would be more difficult for a realistic TBC model. Thus, a simpler FEM model which is given in Figure 4.1 is created to show the effect of the maximum principal stress (MAXPS) parameter on crack initiation.

The two-dimensional FEM model given in Figure 4.1 simulates a displacement controlled three-point bending test. The distance between supports, L, is 40 mm and the height, h, of the beam is 1.6 mm. Four-node bilinear reduced integration elements are used in the model which has 4329 structured finite elements. Unlike the rest of the study, for this 3-point bending test an initial crack which has a size equal to the length of an element is defined at the bottom side of the beam in the middle which is illustrated as a small red line in Figure 4.1. The initial crack is introduced to investigate the effect of the parameters for damage initiation and propagation better.

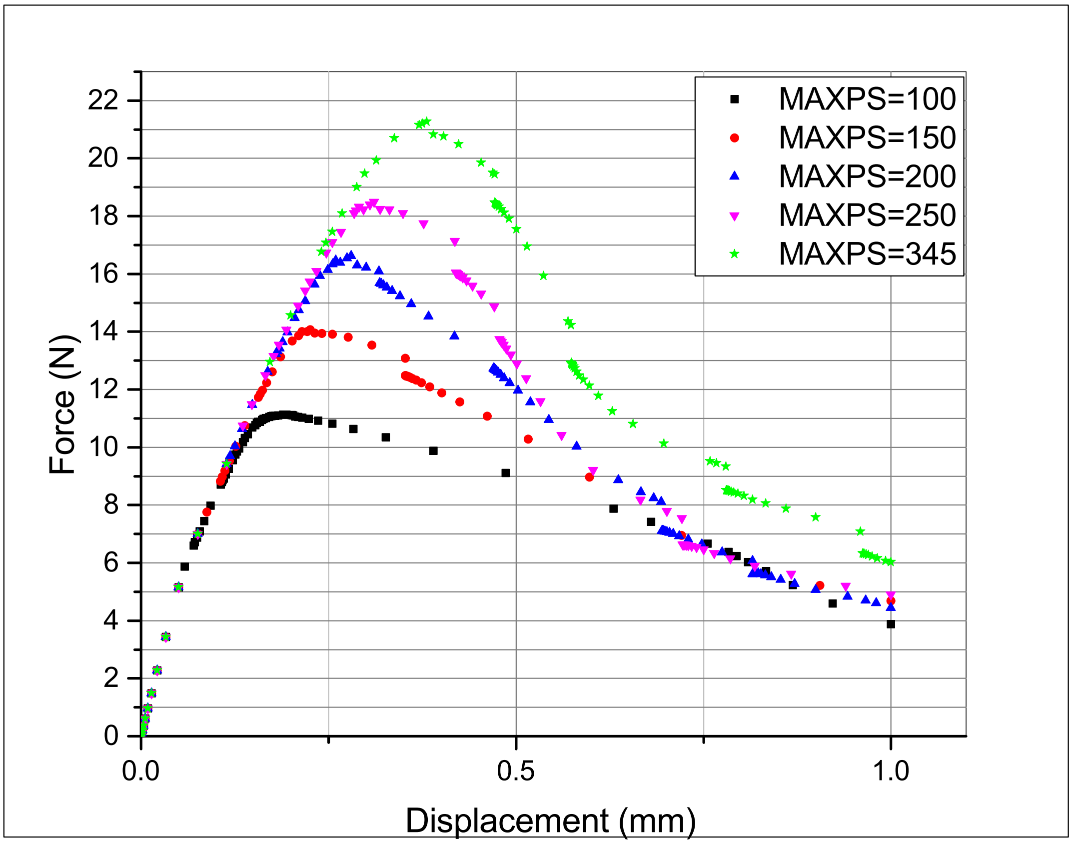

Figure 4.2: Load-displacement curve of 3-point bending test for different MAXPS values

A generic material is used for this study and material parameters given in Table 4.4 are taken from literature [77], which are used for fracture simulations of a grenade handle. An elastic-plastic material model is used for the analysis. For the material failure model MAXPS and the fracture energy are chosen for the damage initiation and the propagation criteria respectively.

Five different analyse are run by varying the MAXPS parameter and the load-displacement curves are compared to each other to investigate the behaviour, see Figure 4.2. It is clearly visible that the lower MAXPS values decrease the crack initiation load of the beam. Figure 4.2 illustrates the relation between the MAXPS parameter and the crack initiation. The crack initiation load is directly proportional with the MAXPS.

In order to show the effect of the fracture energy parameter five more analyse are

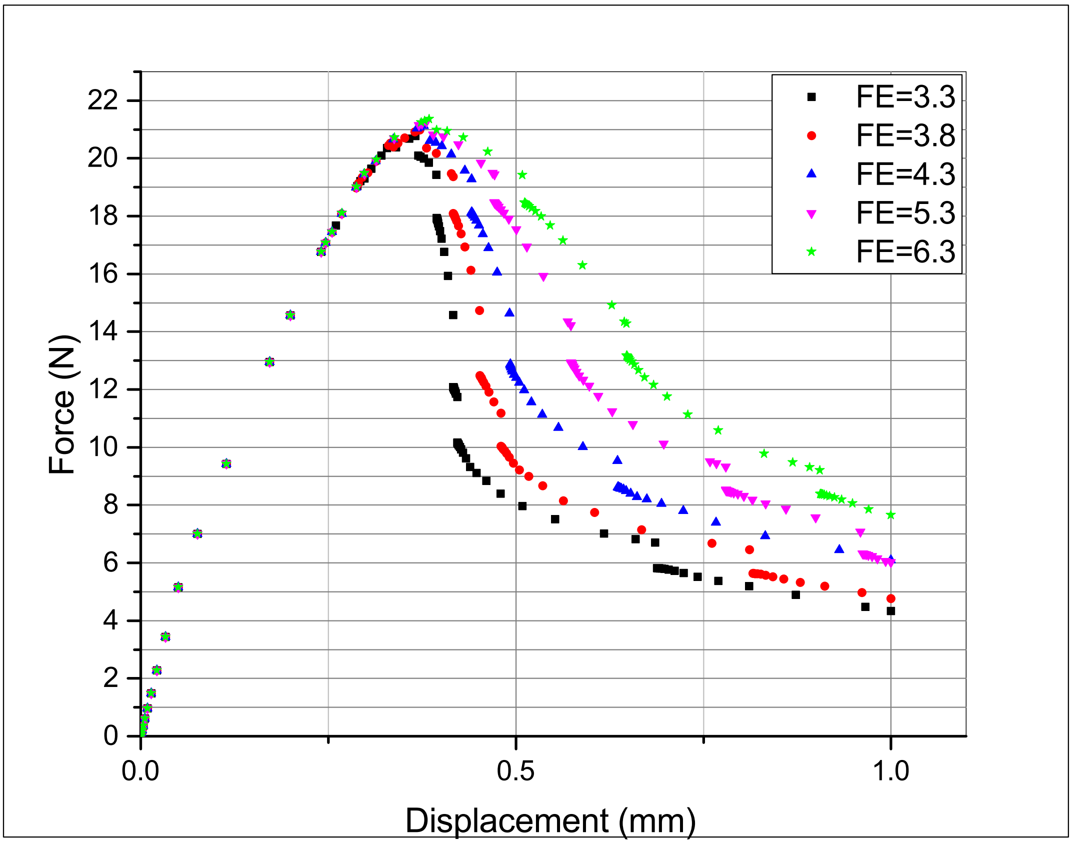

Figure 4.3: Load-displacement curve of 3-point bending test for different fracture energy values

run by varying the fracture energy value and the results are illustrated in Figure 4.3. The fracture energy is not related with the damage initiation, it defines the damage evolution characteristics so the peak points of the load-displacement curves are not changed but the post-peak behaviors are different for different fracture energy values. As expected, higher fracture energy results in a more ductile the post-peak response.

The typical traction-separation response is illustrated by the results presented in Figure 4.2 and 4.3 very well. The MAXPS parameter defines the peak point of the traction-separation relation and the fracture energy defines the area under the curve between the peak point, damage initiation, and the ultimate failure point as described in Section 2.1.4.

The crack propagation in the three-point bending simulation by XFEM is illustrated in Figure 4.4. The images in the figure are chosen arbitrarily among those 10 analyse and they show that the crack propagates through the direction of the initial crack at the bottom of the beam as expected.

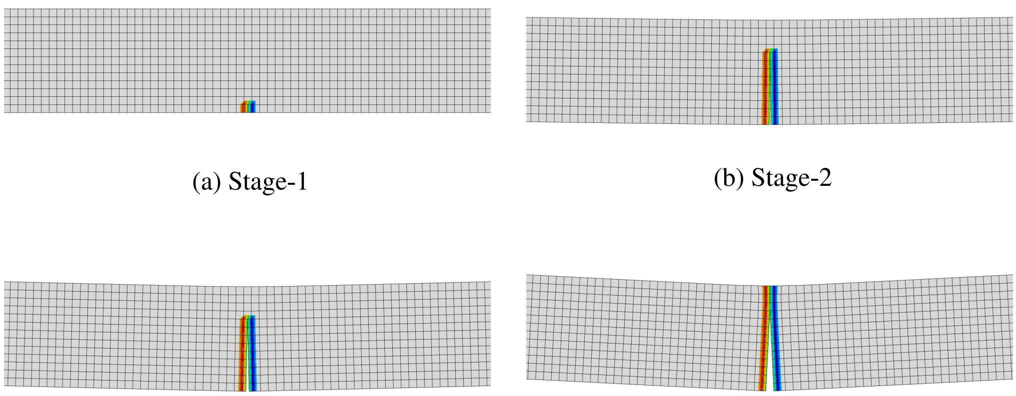

(a) Stage-1 (b) Stage-2

(c) Stage-3 (d) Stage-4

Figure 4.4: Crack propagation in 3-point bending test

The bending fracture stress of the TC layer was not measured in the experiments [1] so there is no available data to assign directly as MAXPS parameter of the XFEM enriched region in TC layer of the TBC specimen. However, when the DIC results of the four-point bending tests presented in [1] are investigated an inference can be made about the crack initiation instant of the specimens. The thick specimen is chosen for the tuning of the MAXPS parameter and then the tuned MAXPS value is assigned to the standard and the thin specimens as well in this numerical study.

The four-point bending tests were made in a displacement controlled manner and the loading rate was constant in the experiments. The failure progress was recorded in-situ using a microscope in conjunction with a DIC system [1]. The cracks initiated at stage 100 for the thick specimen and the ultimate failure occurred at stage 184. Using these data the displacement of the loading supports is calculated as 1 mm. In other words, cracks initiate at approximately 1 mm transverse displacement in four-point bending tests [1].

In this numerical study the time step is specified as 1 in all analyses so the maximum displacement is applied within the time period of 1 to the specimens. Considering that 2 mm displacement is applied in four-point bending test in the numerical study, cracks should start approximately at the time step 0.50. As a result of the iterations made using this data, it is concluded that the MAXPS value should be around 1000 MPa for the TC layer of the TBC specimen. When 1000 MPa value is assigned to the TC layer damage initiation parameter, cracks initiate approximately at time step 0.50 as desired. However, the crack initiation instant does not vary much in different MAXPS patterns which will be explained in Section 4.3.

In order to verify this approximation for the damage initiation parameter value of the TC layer also literature is reviewed. In the study of Kondoh et al. [71] tensile and bending tests were performed for different mol % Y_2O_3 which is also used in the TC layer of the TBC specimens investigated in this study. The experimental results in the study [71] show that 1000 MPa value for the MAXPS parameter used in the XFEM enriched region of the TC layer is reasonable. This supports the approach used to approximate the value from the experimental results of the four-point bending tests [1]. Therefore, 1000 MPa value is assigned to each different thickness specimen in the numerical study because all the specimens tested in the experiments are produced with same processes.

4.3 MAXPS Variations for Randomness Effect

As it is explained in the Section 3.1.2.1 MAXPS value of the outermost layer elements in the TC layer can be fluctuated between certain limits by the script written for this purpose. Ceramic materials are known to be not very homogeneous because of their nature. Even though the global mechanical properties in bulk ceramics can be approximated in relatively small bounds, these properties vary locally to a larger extent because of their porous micro-structure [72]. This cardinal property directly affects the fracture behaviour of the ceramic materials. Therefore, in this study in order to create the randomness effect in the TC layer a fluctuation of the MAXPS parameter in the TC ceramic layer is used for all models.

Fluctuation is applied only to the outermost layer elements of the TC layer and the MAXPS value for the rest of the elements in the XFEM enriched region is fixed to

Table 4.5: Number of cracks for $\pm 3\%$, $\pm 4\%$ and $\pm 5\%$ variation of MAXPS value

Fluctuation Range	**%3**			**%4**			**%5**		
Model Number	**Thin**	**Standard**	**Thick**	**Thin**	**Standard**	**Thick**	**Thin**	**Standard**	**Thick**
Model - 1	9	8	2	10	8	6	8	8	5
Model - 2	9	7	3	10	8	4	10	9	7
Model - 3	11	8	3	9	8	6	9	8	6

1000 MPa. This method is applied to each model with different random fluctuation and thickness. To increase the sturdiness of the analysis three different patterns are created for each thickness. The number of different random fluctuation patterns for each thickness can be increased but because of insufficient computational resources the number is limited to three.

Iterations have been started by applying $\pm 1\%$ fluctuation to the numerical models, in other words, the upper and the lower bounds of the MAXPS is 990 MPa and 1010 MPa respectively at the outermost layer elements. However, $\pm 1\%$ difference leads to cracks initiated almost every elements in the TC layer. This situation contradicts the main aim to define the random variation procedure. Iterations are continued by increasing $\pm 1\%$ more the upper and the lower bound of the MAXPS values, but the same problem is experienced with $\pm 2\%$ variation as well.

Reasonable and acceptable results are obtained with the $\pm 3\%$ fluctuation value. Number of cracks are low in the thick specimen compared to the standard and the thin specimen but the results are plausible compared to $\pm 1\%$ and $\pm 2\%$ fluctuation cases. The number of cracks for each specimen and each different fluctuation pattern are tabulated in Table 4.5. Analysis are continued to increase the variation limits with 1% resolution and the results for $\pm 4\%$ and $\pm 5\%$ fluctuations are also tabulated in Table 4.5 while $\pm 6\%$ and $\pm 7\%$ are given in Table 4.6.

The number of cracks in the thick specimen starts to decrease drastically for $\pm 7\%$ fluctuation. Therefore, higher fluctuation ranges are not studied. After the number of cracks are determined from simulations the average crack spacings of the TC layer is calculated for each specimen. As explained in Chapter 3, the cracks are expected to initiate and propagate only in the constant moment region of the TBC beam which

Table 4.6: Number of cracks for $\pm 6\%$ and $\pm 7\%$ variation of MAXPS value

	%6			%7		
Model Number	**Thin**	**Standard**	**Thick**	**Thin**	**Standard**	**Thick**
Model - 1	9	8	6	7	6	2
Model - 2	9	8	6	6	6	2
Model - 3	10	8	5	6	5	1

has a length of 14 mm. To this end 14 mm length is used in the average crack spacing calculations as in the experiments [1]. The average crack spacing definition is given as follows

$$Average\ Crack\ Spacing = \frac{L}{Total\ Cracks}. \tag{4.2}$$

The average crack spacing is calculated according to the average number of cracks values of three different fluctuation patterns for different thickness specimens, and the results are shown in Figure 4.5 together with the experimental results [1]. According to the results it can be seen that the change in average crack spacing with the TC thickness is similar in simulations and experiments. Both the experiments and the finite element results show that the increase in the thickness of TC results in an increase in the average crack spacing for every fluctuation value. Numerical results of $\pm 4\%$, $\pm 5\%$ and $\pm 6\%$ fluctuations are very consistent and in a good agreement with each other.

4.4 Cohesive Surface Damage Initiation and Propagation

One of the main objectives of this study is to see whether XFEM and CZM techniques work together to simulate crack formation and propagation in the interfaces of composite beams such as TBCs. Those two techniques work well together until this point of the study so far but the delamination between the TC and the BC layer is not very prominent. To investigate the delamination mechanism of the TBCs, the cohesive damage initiation parameter MAXS value has to be changed for the crack propagation at the TC/BC interface. So far 2000 MPa value is assigned for all mod-

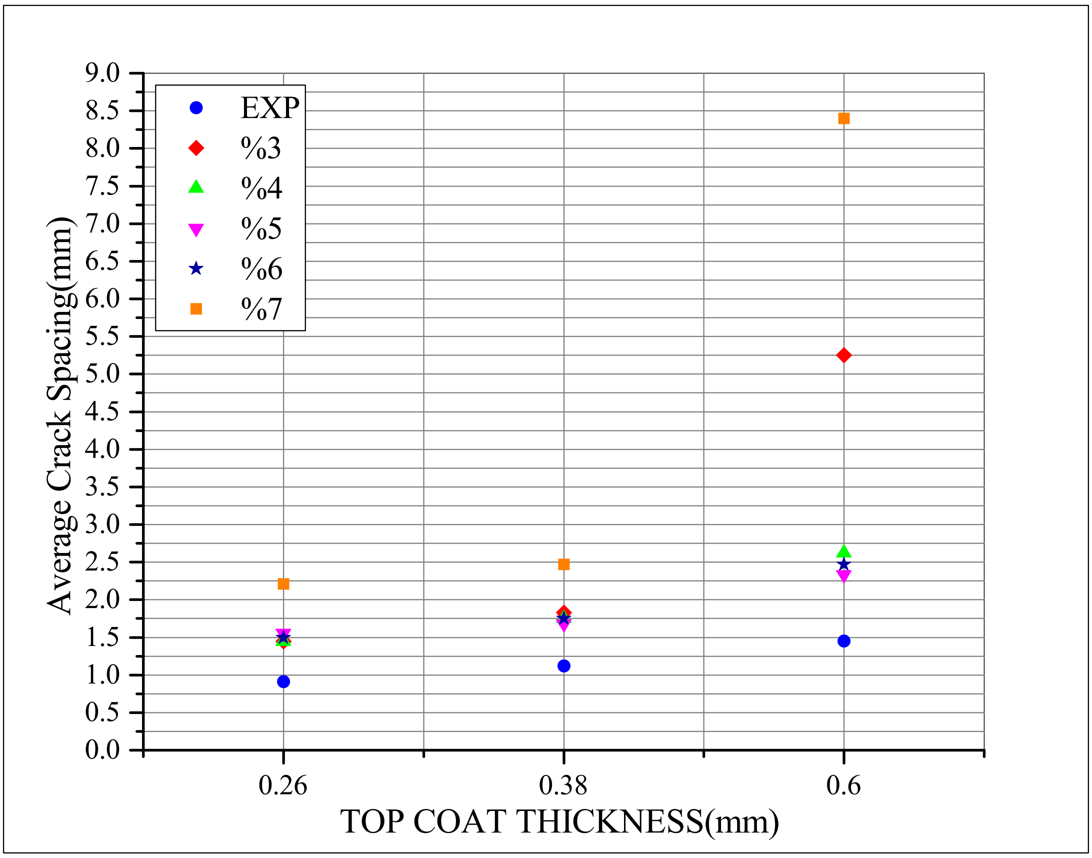

Figure 4.5: Average crack spacing comparison for different MAXPS fluctuations and experimental results [1]

els. For the damage evolution of the cracks at the interface 6.80 kJ/m^2, 7.36 kJ/m^2 and 8.27 kJ/m^2 fracture energy values are assigned for the thin, standard and thick specimens respectively as it was calculated in the experiments [1].

In order to start the iterations for the cohesive zone damage initiation paramater MAXS, $\pm 5\%$ fluctuation of MAXPS is selected because $\pm 5\%$ distribution results are very consistent with the experimental results [1] in the manner of average crack spacing as shown in Figure 4.5. Model-3 of $\pm 5\%$ distribution is chosen arbitrarily and analyses are run with thick specimen.

The MAXS value of the cohesive zone is decreased 100 MPa for every iteration step and the results start to change at 1300 MPa value. The analyse are completed with

1300 MPa value and the results are shown in Figure 4.11. It is clearly seen that delamination between the TC/BC layer is much more prominent compared to the results of the analysis with 2000 MPa MAXS value shown in Figure 4.10. The load-displacement behaviour of these two analyses with the experimental results are given in Figure 4.6. The load-displacement behaviour of the two different analyses with different MAXS values are quite similar until 1.88 mm displacement is applied to the beam. At this point the first delamination starts at the TC/BC interface of the beam, and this delamination results in one more sharp drop in the load-displacement curve. This decreases the load carrying capacity of the beam and changes the softening behavior. Unlike the other sharp drops in the curve this drop occurs not due to the cracks which propagate in the TC layer vertically towards to TC/BC interface but it occurs because of the delamination at the interface. The second drop which is only seen in the analysis run with 1300 MPa MAXS is observed at 1.973 mm displacement level. This is the instant of the second delamination at the interface. Numerical results are very consistent with each other but if they are compared with the experimental results, a good agreement is found only in the elastic region. Experimental load displacement curves are not the main scope of these numerical simulations and FEM models are created according to the nominal size values of the beams which are given in the study [1] and the tolerance values are not taken into account. The XFEM and CZM damage initiation and evolution parameters used in this finite element study are not directly measured values in the experiments [1] and they are approximated to the actual values by iterations. Therefore, the difference in load displacement curves between the experimental and FEM results are considered as plausible.

The same procedure is applied to the standard specimen but iterations are started with 1300 MPa MAXS value. The delamination at the interface is not prominent as it is seen in Figure 4.12 so the MAXS value is further decreased with a resolution of 100 MPa. At 900 MPa value the delamination at the interface is observed. The crack propagation and delamination results are shown in Figure 4.13. The load-displacement curves for MAXS values of 2000 MPa, 1300 MPa, 900 MPa and the experiment [1] are shown in Figure 4.7. As illustrated in Figure 4.7, the softening behaviour of the standard specimen differs from the thick specimen, because the TC layer of the standard specimen is thinner than the thick one although the thickness of the substrate

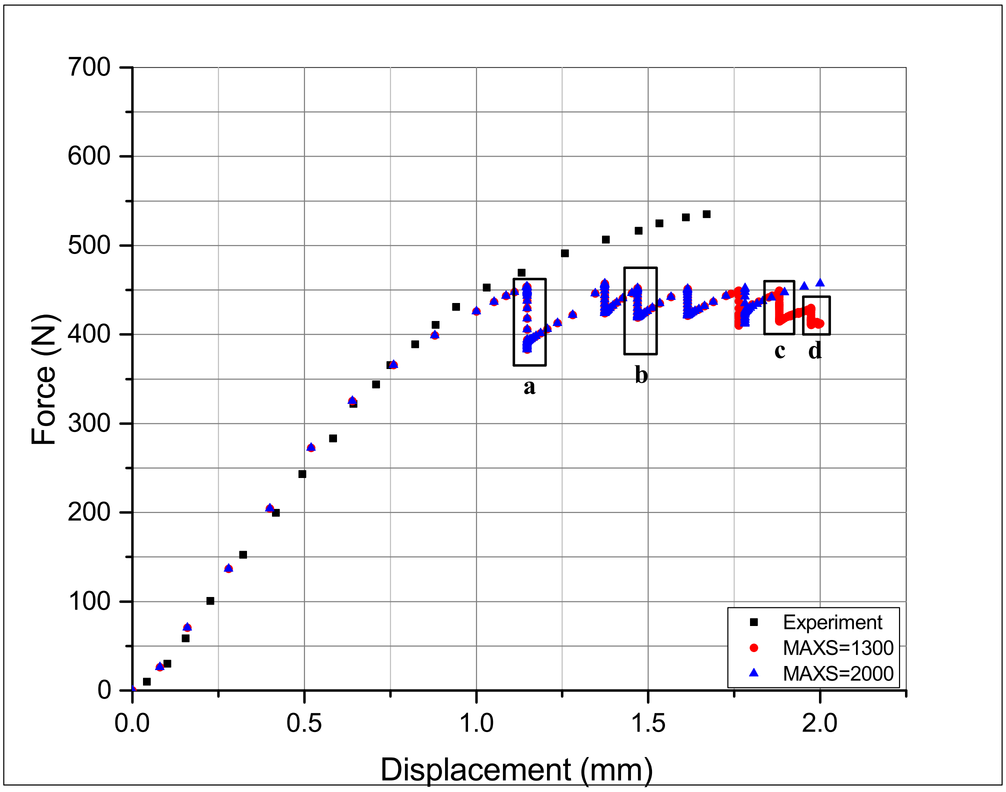

Figure 4.6: Load-displacement behaviour comparison of thick model for different MAXS values with the experimental results [1]

layer does not change for each specimen. Therefore, the load carrying capacity of the TC layer of the composite TBC beam is lower in the standard beam compared to the thick one. This geometrical difference between models explains the smaller sharp drops in the load-displacement curve in Figure 4.7. The load-displacement curves of numerical results are in good agreement with each other but they all differ from experimental results. The possible reasons of the difference are explained previously.

The procedure which is applied to the thick and the standard FEM models is applied to the thin model as well. For the thin model iterations are started with 900 MPa whereof the results are shown in Figure 4.14. The larger delaminations occur at the interface with for MAXS=600 MPa and the results are shown in Figure 4.15. The load-displacement behaviour of the numerical analyses and the experiment are illustrated together in Figure 4.8. The same phenomenon which is encountered in standard

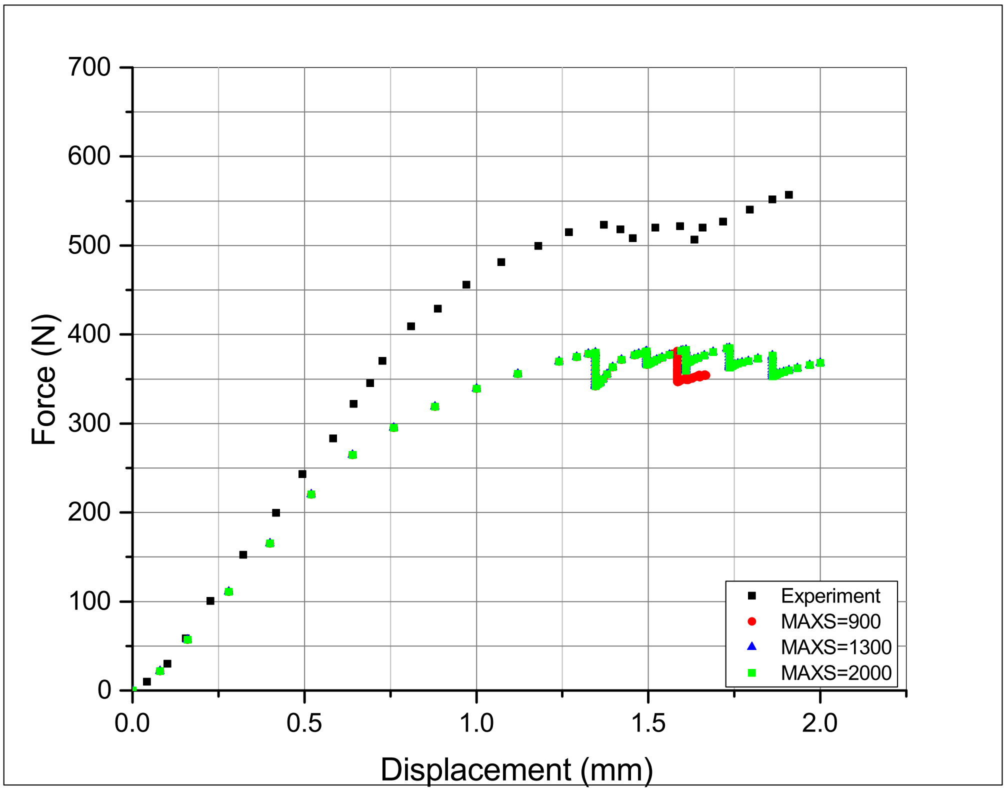

Figure 4.7: Load-displacement behaviour comparison of standard model for different MAXS values with the experimental results [1]

and thick models is observed in the thin model as well.

The main purpose of this numerical study is to investigate the cracking mechanism of TBCs and study the variation of average crack spacing with the coating thickness change. The cracking mechanisms of different thickness TBC specimens are similar, i.e., first, cracks perpendicular to surface initiate at the uppermost layer elements and they propogate through the TC layer vertically. Then, vertical cracks reach to TC/BC interface and stop, followed by delamination initiation and propagation through the interface. The delamination is more prominent in the thick model compared to standard and thin models as it was observed in experiments [1], see Figure 4.9. In other words, simulation results of combined XFEM/CZM model show similar behaviour with the experiments [1].

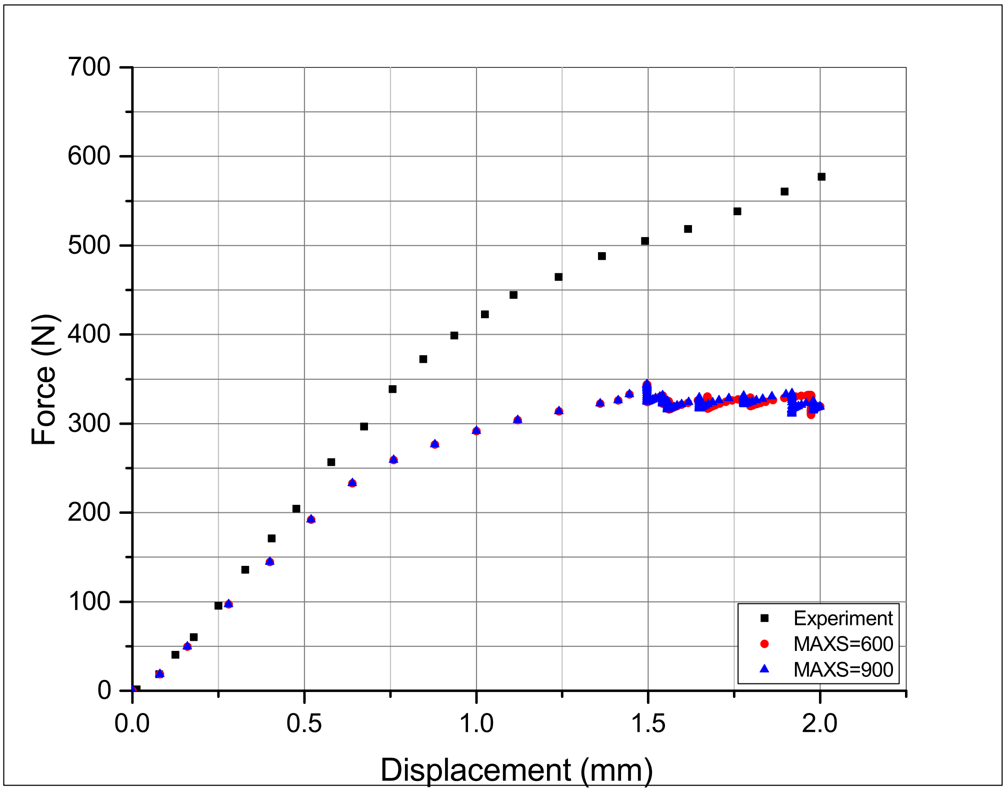

Figure 4.8: Load-displacement behaviour comparison of thin model for different MAXS values with the experimental results [1]

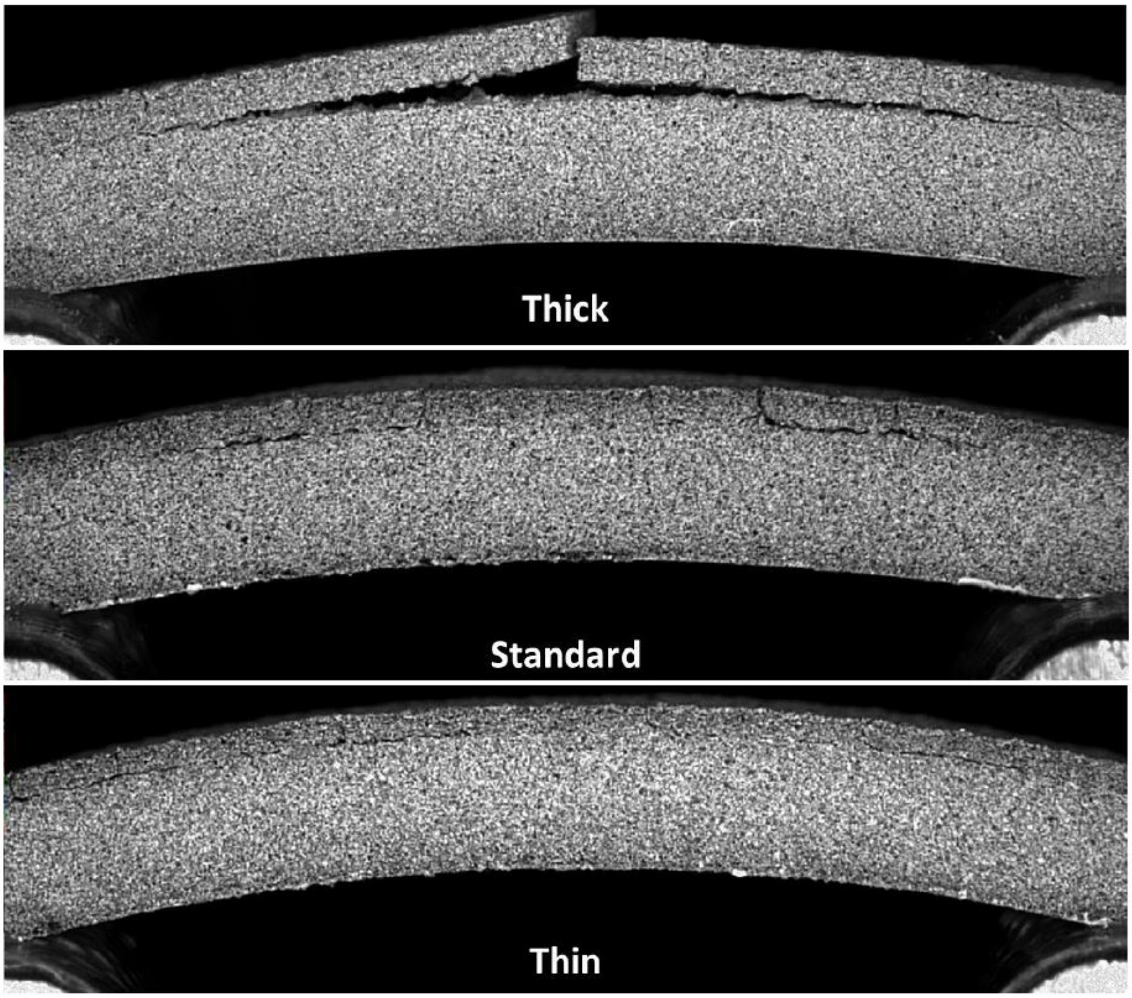

Figure 4.9: Experimental results of the four-point bending test for the thin, the standard and the thick specimen [1]

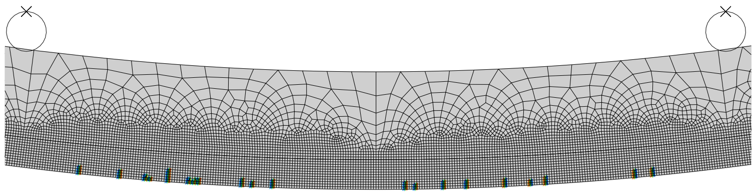

(a) Time Step=0.5739, corresponds to point a before the load drop in Figure 4.6

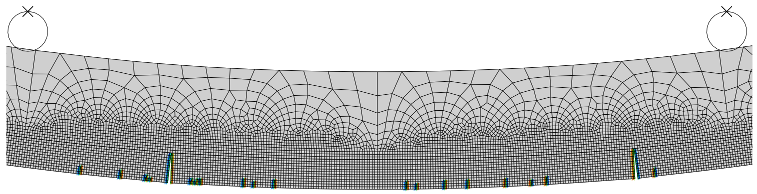

(b) Time Step=0.5739, corresponds to point a after the load drop in Figure 4.6

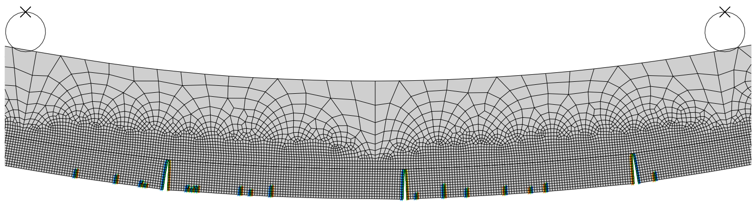

(c) Time Step=0.7344, corresponds to point b before the load drop in Figure 4.6

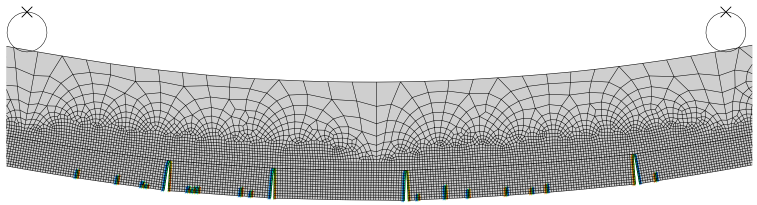

(d) Time Step=0.7344, corresponds to point b after the load drop in Figure 4.6

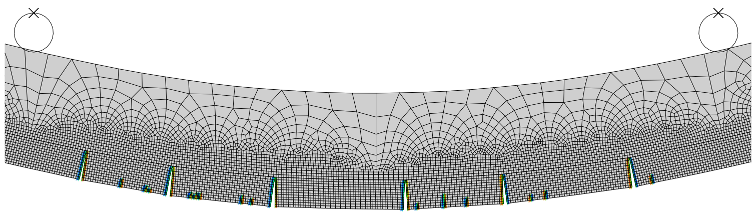

(e) Time Step=0.891

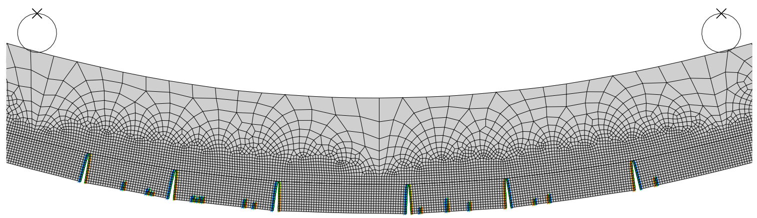

(f) Time Step=1

Figure 4.10: Model-3 results for the thick specimen with MAXS=2000

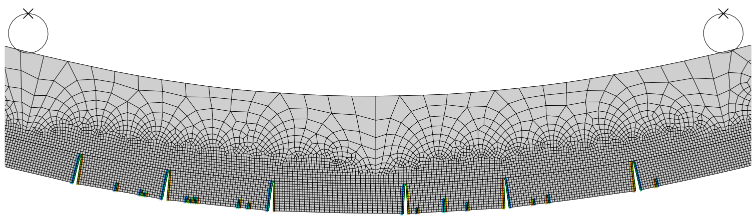

(a) Time Step=0.941, corresponds to point c before the load drop in Figure 4.6

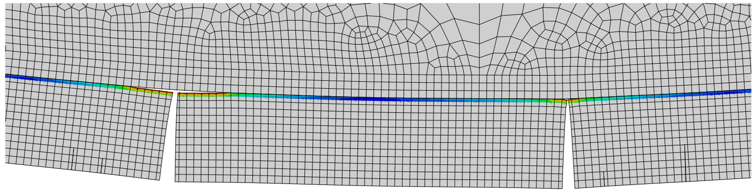

(b) Time Step=0.941, corresponds to point c during the load drop in Figure 4.6

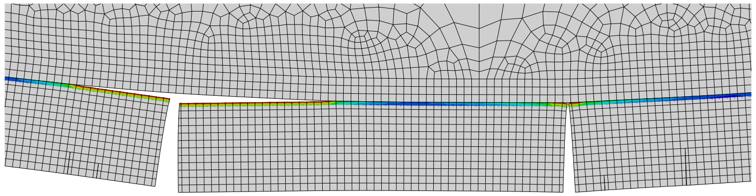

(c) Time Step=0.941, corresponds to point c after the load drop in Figure 4.6

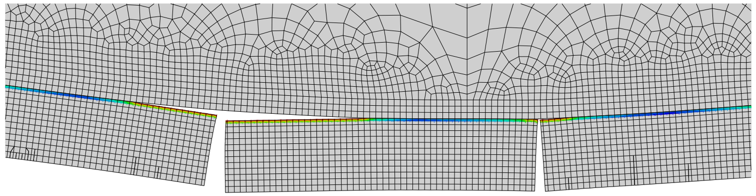

(d) Time Step=0.987, corresponds to point d before the load drop in Figure 4.6

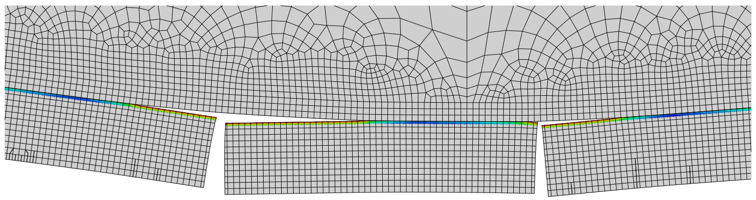

(e) Time Step=0.987, corresponds to point d after the load drop in Figure 4.6

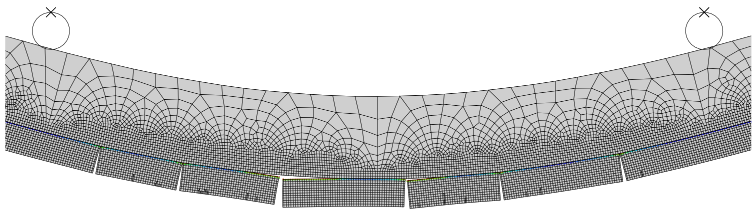

(f) Time Step=1

Figure 4.11: Model-3 results for the thick specimen with MAXS=1300

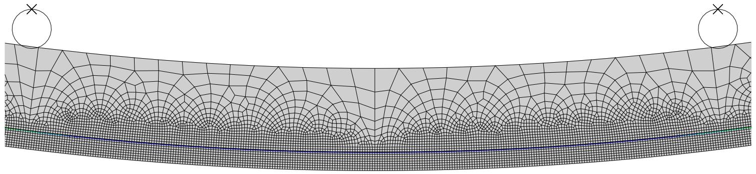

(a) Time Step=0.56

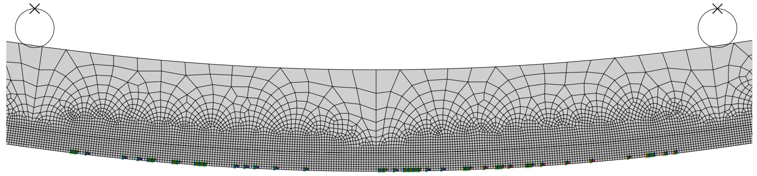

(b) Time Step=0.62

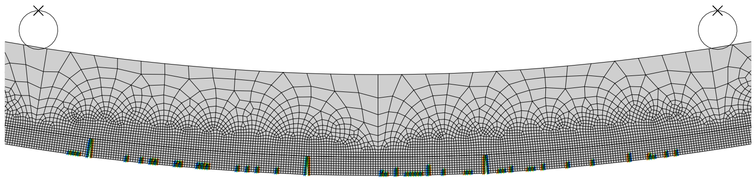

(c) Time Step=0.6737

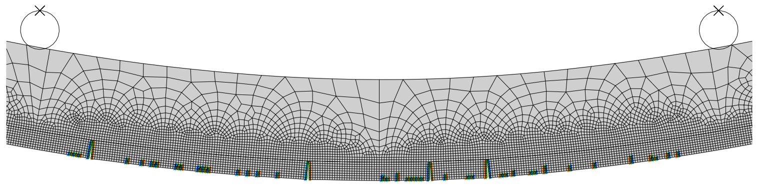

(d) Time Step=0.7518

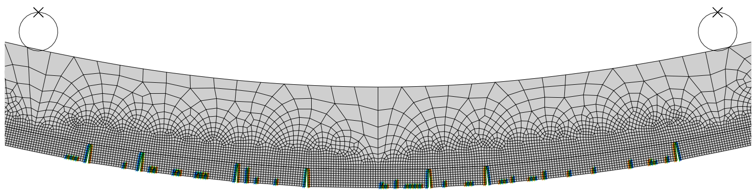

(e) Time Step=0.8676

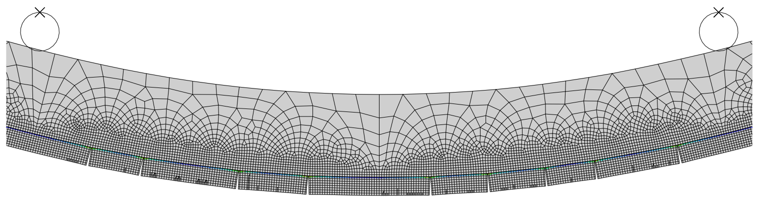

(f) Time Step=1

Figure 4.12: Model-3 results for the standard specimen with MAXS=1300

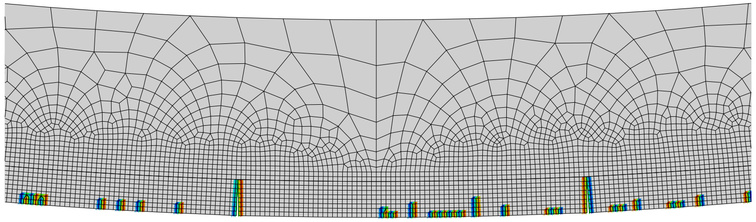

(a) Time Step=0.673

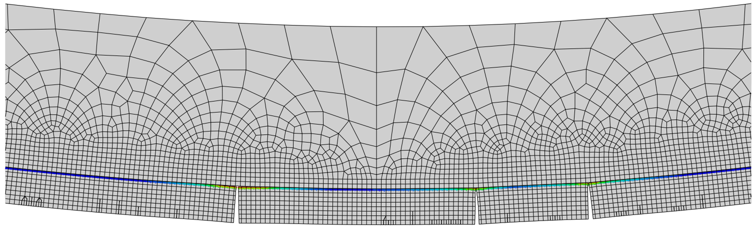

(b) Time Step=0.792

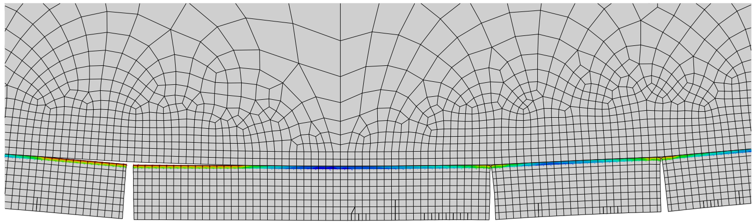

(c) Time Step=0.792

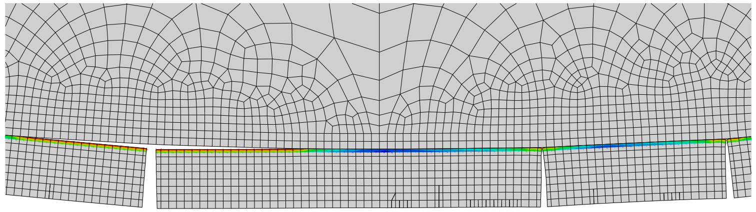

(d) Time Step=0.792

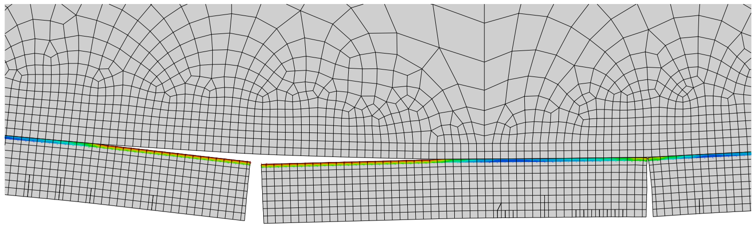

(e) Time Step=0.8676

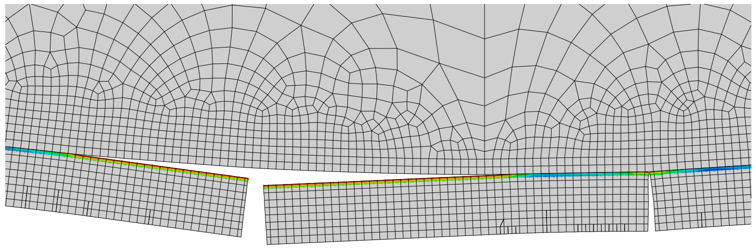

(f) Time Step=0.834

Figure 4.13: Model-3 results for the standard specimen with MAXS=900

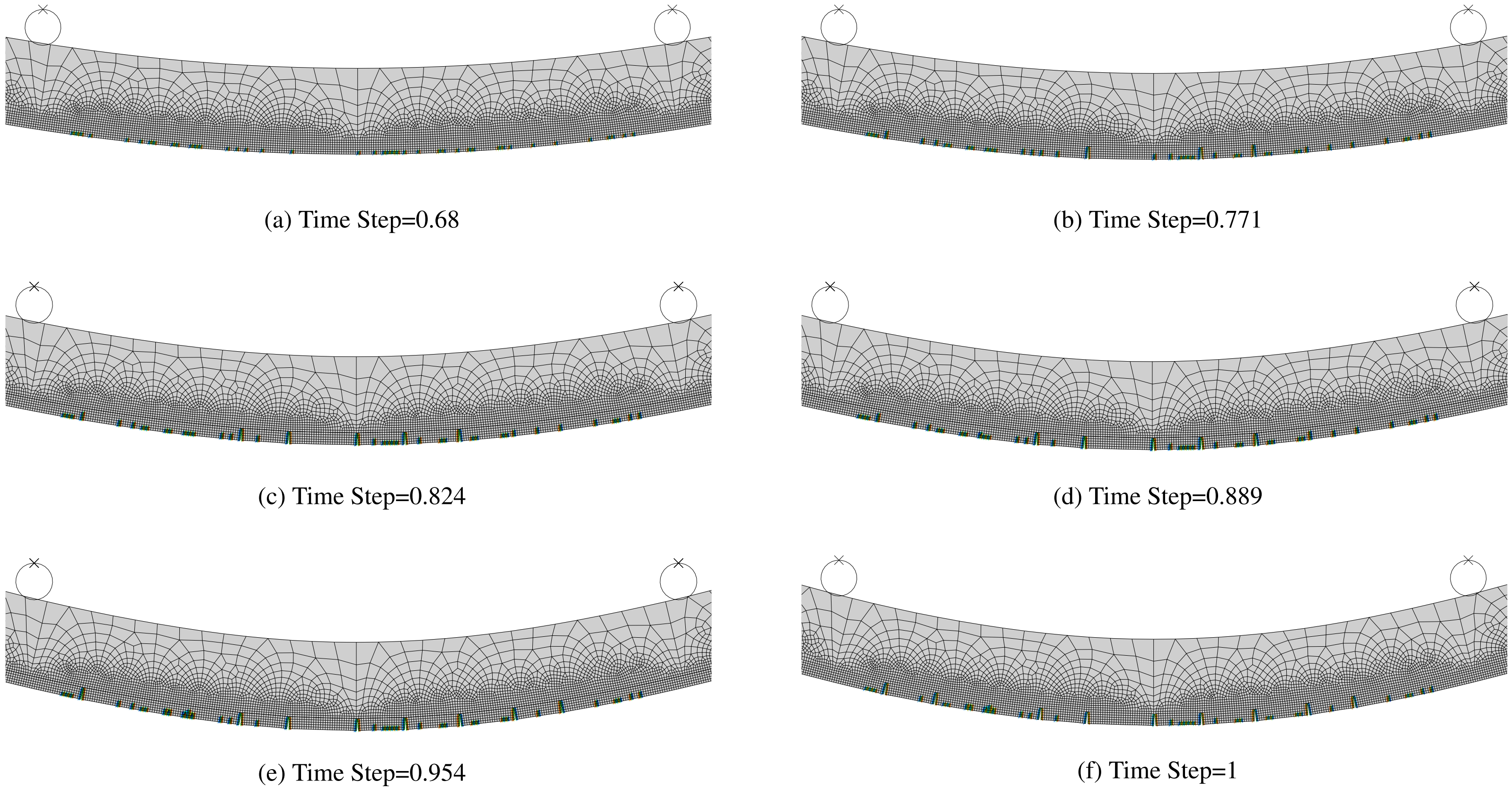

(a) Time Step=0.68

(b) Time Step=0.771

(c) Time Step=0.824

(d) Time Step=0.889

(e) Time Step=0.954

(f) Time Step=1

Figure 4.14: Model-3 results for the thin specimen with MAXS=900

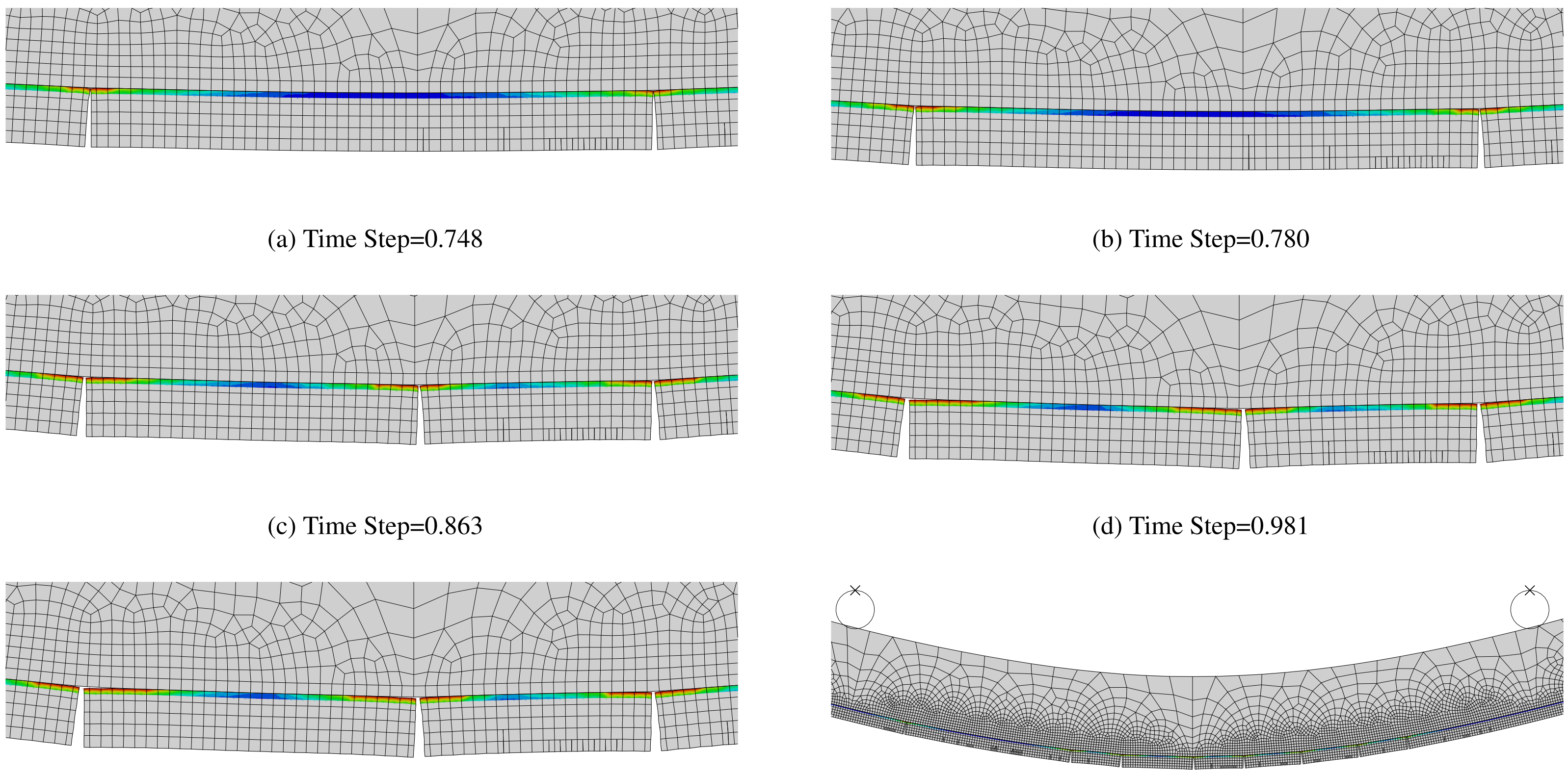

(a) Time Step=0.748

(b) Time Step=0.780

(c) Time Step=0.863

(d) Time Step=0.981

(e) Time Step=0.985

(f) Time Step=1

Figure 4.15: Model-3 results for the thin specimen with MAXS=600

4.5 Overcome to Convergence Issues

Unlike the solution of linear problems, in a nonlinear analysis such as damage and fracture problems the solution cannot be calculated by solving a single step of linear equations. Instead, the loading is determined as a function of time to find the solution and time is increased incrementally to obtain the nonlinear response. Therefore, the simulation is split into a number of time increments by Abaqus/Standard and the approximation is found at the end of each time increment. However, using the Newton method, it generally takes several iterations to determine an acceptable solution for each time increment [17, 78].

Convergence difficulties are very familiar issues for damage and fracture analysis in Abaqus and there are several different methods which are given below to overcome the convergence problems;

- the viscous regularization
- the automatic stabilization
- the nondefault solution controls

In this study automatic stabilization technique is used to overcome the encountered convergence problems throughout the study.

Consider the external nodal forces P and the internal nodal forces I acting on a body. The source of the internal loads acting on a node is the stresses in the adjacent elements that are attached to that node. To satisfy the equilibrium for the body, the net force acting at every node must be zero. Therefore, the basic statement of equilibrium is that the internal forces, I, and the external forces, P, must balance each other:

$$P - I = 0 \tag{4.3}$$

However, nonlinear static problems can be unstable and the equilibrium given in Equation 4.3 is not satisfied in every time increment during the analysis. This type of problems has to be solved either by dynamical analysis method or with the addition of artificial damping to the finite element model [17].

Abaqus/Standard provides an automatic mechanism to stabilize unstable quasi-static problems through the automatic addition of damping to the model. The applied damping factors can be constant over the duration of a step, or they can vary with time to account for changes over the course of a step [17]. In this study, constant damping approach is preferred, because convergence could not be satisfied sustainably when adaptive damping approach is used.

Viscous forces of the form

$$F_v = cM^*v \tag{4.4}$$

are added to the global equilibrium equations, where M^* refers to an artificial mass matrix calculated with unity density. c refers to a damping factor, $v = \Delta u/\Delta t$ is the vector of nodal velocities, and Δt is the time increment [17].

In order to ensure that the solutions are accurate and acceptable the viscous damping energy (ALLSD) is compared with the total strain energy (ALLIE). The ratio should be kept in a reasonable amount [17].

As mentioned before the constant damping factor is used for every analysis and the value for the damping factor is found iteratively. After every run the values of the ALLSD are checked for every time increment over the course of the analysis according to recommendation of the Abaqus documentation [17]. This methodology is applied throughout the study. The ALLSD value is tried to kept below %5 of the ALLIE value, see Figure 4.16 which is an arbitrarily chosen example from the analysis results in this study.

For the detailed explanation about the automatic stabilization and the other methods to overcome convergence problems see Abaqus documentation [17].

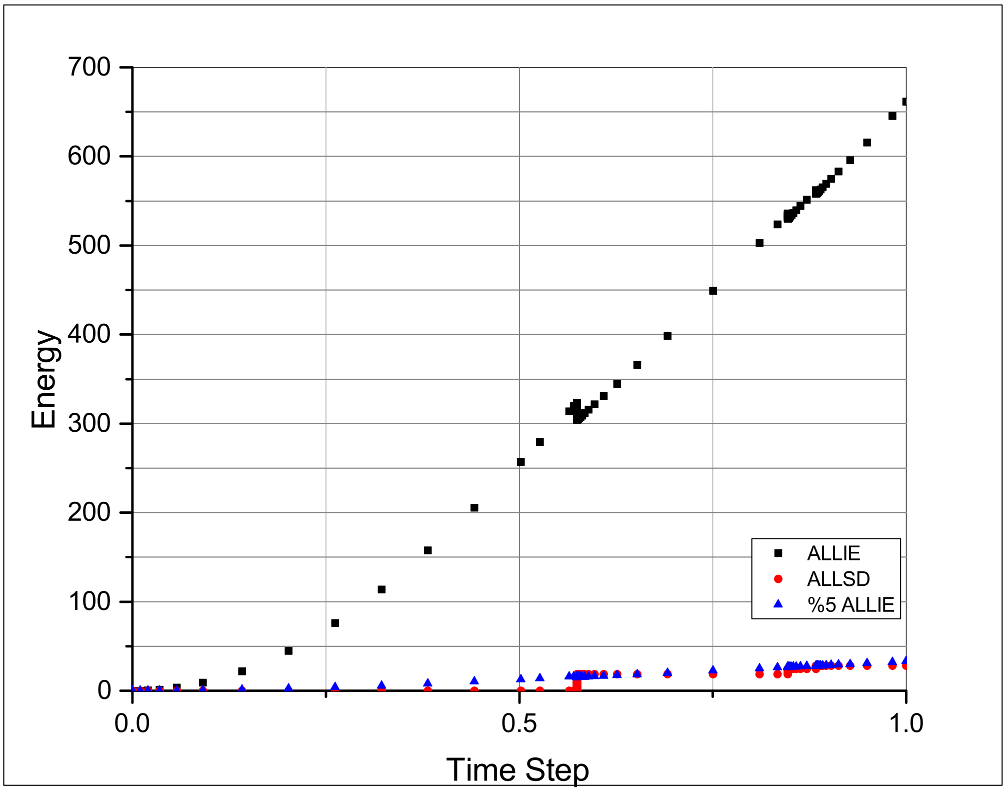

Figure 4.16: Comparison of the viscous damping energy (ALLSD) with the total strain energy (ALLIE)

CHAPTER 5

CONCLUSION

5.1 Summary

The work presented in this thesis aims to investigate the failure mechanisms of TBCs by using the XFEM and the CZM which are already available in the commercial FEA software Abaqus. The main motivation of the study is to investigate the complete failure mechanism of a TBC system which consists of initiation and propagation of surface cracks followed by a delamination by combining these two methods.

In the first chapter of the study the main motivation of the TBC use in jet engines is briefly explained and the historical evolution of the materials used in a typical TBC system for the aviation industry are given. The two main processes for the TBC deposition and the different failure modes of the TBCs are explained. Then the numerical studies which use the XFEM or the CZM in the literature for the investigation of the TBC failure are also summarized and the scope of the study is presented.

In the second chapter, the solution methods of the fracture mechanics problems in conventional finite element methods are briefly introduced and their evolution is given in a historical order. However, the conventional finite element method has many limitations in fracture mechanics problems. These defects of the conventional methods are summarized and the basic motivation underlying the need for improvement of the XFEM is explained. The evolution of the XFEM and its advantages against the conventional finite element method are presented, and the theory behind the method is introduced. The second method used in this study is the CZM for the investigation of the delamination in the TBCs. The CZM is also introduced and the underlying theory of this method is also given. The implementation of both methods in Abaqus are explained and the limitations of the XFEM method in Abaqus are summarized.

In the third chapter, the created finite element models to investigate the four-point bending study in the literature [1] are introduced. The methodology of the new approach and its necessity to create the randomness effect in the TC layer ceramic material are explained. The traction-separation approach is chosen for the damage initiation and propagation in this numerical study. The parameters used for the traction-separation approach in the XFEM enriched region and the cohesive zone for the crack initiation and the propagation are explained. For the analyses a mesh verification study is conducted and its results are given.

In the last chapter of the thesis the results of the numerical study by using the XFEM and the CZM are presented, and the results are compared with the experimental findings [1]. The main failure behaviour of the TBCs which is seen in the experiments is also observed in the simulations. The cracks initiate at the free surface of the TC layer and propagate through the TC layer vertically towards to the TC/BC interface. When they reach to the interface the delamination starts. The variation of average crack spacings by the thickness increase in the film layer is in a good agreement with the experimental results.

5.2 Conclusions

The XFEM has made many improvements in the examination of the fracture mechanics problems and it presents many computational advantages such as:

- it eliminates the necessity of remeshing
- it can solve the problems of crack propagation with non-continuous characteristics
- the crack propagation path is not necessary to be defined
- the propagation path of the crack can be traced

Even though the XFEM offers many advantages for fracture mechanics problems, its implementation to Abaqus has still some drawbacks. In this study severe convergence problems have been encountered. The major causes of these difficulties may be related to the complex geometry of the TBCs and their complex fracture behaviour. It requires very small time increments for the crack propagation and this increases the run times of the analyses. In order to overcome the convergence difficulties a damping must be applied. According to the literature [78] an automatic stabilization would be appropriate. However, in this problem automatic stabilization did not work and convergence problems continued. Therefore, throughout the study fixed damping values are used and this parameter is determined iteratively by controlling the dissipated energy to internal energy ratio below 5%. This procedure extends the process to get acceptable results.

Even though the XFEM in Abaqus still needs enhancements it gives satisfactory results for the crack initiation and also gives the traceable crack propagation paths. The results obtained are plausible when compared with the experimental results [1].

5.3 Future Work

In this thesis, a numerical study is developed with a new approach by applying fluctuation to the MAXPS parameter in the TC layer to observe the fracture mechanism of the TBCs. In the future, the subjects given below can be considered for a better understanding of the fracture mechanisms of the TBC systems:

- To increase the sturdiness of the analyses number of created patterns with the artificial MAXPS fluctuation parameter for each different thickness model can be increased.
- The study can be incorporated with the experiments for material characterization of the TC and the TC/BC interface for the parameters which will be the direct inputs for the XFEM and the CZM respectively
- According to the literature the TGO layer is quite important for the fracture mechanism. As a future work investigation of the complete fracture mechanism of the TBCs consisting of TC cracks, TC/BC interfacial delamination and TGO driven delamination in the TC layer in a single model would be interesting.

- Residual stress is an important factor for the investigation of the failure mechanisms of the TBCs. In this study, residual stresses are not taken into account. The study can be extended with thermo-mechanical analysis for the investigation of residual stress driven cracks.

REFERENCES

[1] B. Kütükoğlu. Experimental investigation of the failure of air plasma sprayed thermal barrier coatings, 2015.

[2] D. R. Clarke, M. Oechsner, N. P. Padture. Thermal-barrier coatings for more efficient gas-turbine engines. *MRS bulletin*, 37(10):891–898, 2012.

[3] R. L. Jones. Thermal barrier coatings. In *Metallurgical and ceramic protective coatings*, pages 194–235. Springer, 1996.

[4] M. Bäker and P. Seiler. A guide to finite element simulations of thermal barrier coatings. *Journal of Thermal Spray Technology*, 26(6):1146–1160, 2017.

[5] B. Heeg, V. K. Tolpygo, D. R. Clarke. Damage evolution in thermal barrier coatings with thermal cycling. *Journal of the American Ceramic Society*, 94:s112–s119, 2011.

[6] J. Aktaa, K. Sfar, D. Munz. Assessment of tbc systems failure mechanisms using a fracture mechanics approach. *Acta materialia*, 53(16):4399–4413, 2005.

[7] D. D. Hass. Thermal barrier coatings via directed vapor deposition. 2002.

[8] H. Zhao. *Low conductivity thermal barrier coatings*. PhD thesis, University of Virginia, 2009.

[9] R. VaBen, X. Cao, Xueqiang, D. Stover. Improvement of new thermal barrier coating systems using a layered or graded structure. In *Annual Conference on Composites, Advanced Ceramics, Materials, and Structures-B: Ceramic Engineering and Science Proceedings*, volume 4, page 435, 2009.

[10] A. Kumar, S. K. Nayak, P. Bijalwan, M. Dutta, A. Banerjee, T. Laha. Optimization of mechanical and corrosion properties of plasma sprayed low-chromium containing fe-based amorphous/nanocrystalline composite coating. *Surface and Coatings Technology*, 370:255–268, 2019.

[11] N. P. Padture, M. Gell, E. H. Jordan. Thermal barrier coatings for gas-turbine engine applications. *Science*, 296(5566):280–284, 2002.

[12] H. Bhadeshia. Coatings for turbine blades.

[13] A. G. Evans, D. R. Mumm, J. W. Hutchinson, G. H. Meier, F. S. Pettit. Mechanisms controlling the durability of thermal barrier coatings. *Progress in materials science*, 46(5):505–553, 2001.

[14] L. Gigliotti. Assessment of the applicability of xfem in abaqus for modeling crack growth in rubber. 2012.

[15] S. T. Kyaw, I.A. Jones, T.H. Hyde. Simulation of failure of air plasma sprayed thermal barrier coating due to interfacial and bulk cracks using surface-based cohesive interaction and extended finite element method. *The Journal of Strain Analysis for Engineering Design*, 51(2):132–143, 2016.

[16] T. Rabczuk, G. Zi, A. Gerstenberger, W. A. Wall. A new crack tip element for the phantom-node method with arbitrary cohesive cracks. *International Journal for Numerical Methods in Engineering*, 75(5):577–599, 2008.

[17] DASSAULT Systemes. Abaqus 6.14 analysis user's guide: Analysis, vol. iv. *Dassault Systemes*, 2014.

[18] D. R. Clarke, S. R. Phillpot. Thermal barrier coating materials. *Materials today*, 8(6):22–29, 2005.

[19] R. A. Miller. Thermal barrier coatings for aircraft engines: history and directions. *Journal of thermal spray technology*, 6(1):35, 1997.

[20] W. N. Harrison, D. G. Moore, J. C. Richmond. Review of an investigation of ceramic coatings for metallic turbine parts and other high-temperature applications. 1947.

[21] R. Vaßen, M. O. Jarligo, T. Steinke, D. E. Mack, D. Stöver. Overview on advanced thermal barrier coatings. *Surface and Coatings Technology*, 205(4):938–942, 2010.

[22] S. Stecura. Optimization of the nicral-y/zro-y2o3 thermal barrier system. 1985.

[23] M. F. J. Koolloos. Behaviour of low porosity microcracked thermal barrier coatings under thermal loading. 2003.

[24] R. L. Jones. Some aspects of the hot corrosion of thermal barrier coatings. *Journal of Thermal Spray Technology*, 6(1):77–84, 1997.

[25] A. C. Karaoglanli, K. Ogawa, A. Turk, I. Ozdemir. Thermal shock and cycling behavior of thermal barrier coatings (tbcs) used in gas turbines. *Progress in gas turbine performance*, pages 237–260, 2013.

[26] L. Wang, X. H. Zhong, Y. X. Zhao, S. Y. Tao, W. Zhang, Y. Wang, X. G. Sun. Design and optimization of coating structure for the thermal barrier coatings fabricated by atmospheric plasma spraying via finite element method. *Journal of Asian Ceramic Societies*, 2(2):102–116, 2014.

[27] N. M. Yanar. *The failure of thermal barrier coatings at elevated temperatures*. PhD thesis, University of Pittsburgh, 2004.

[28] K. Abe, T. Aranami, Y. Harada M. A. Yoshiba. High-temperature oxidation and hot corrosion behavior of two kinds of thermal barrier coating systems for advanced gas turbines. *Journal of Thermal Spray Technology*, 5(3):259–268, 1996.

[29] T. A. Taylor and P. N. Walsh. Thermal expansion of mcraly alloys. *Surface and Coatings Technology*, 177:24–31, 2004.

[30] M. F. J. Koolloos and J. M. Houben. Behavior of plasma-sprayed thermal barrier coatings during thermal cycling and the effect of a preoxidized nicraly bond coat. *Journal of thermal spray technology*, 9(1):49–58, 2000.

[31] P. Richer, M. Yandouzi, L. Beauvais, B. Jodoin. Oxidation behaviour of conicraly bond coats produced by plasma, hvof and cold gas dynamic spraying. *Surface and Coatings Technology*, 204(24):3962–3974, 2010.

[32] T. Roberts. The structure and stability of high temperature intermetallic phases for application within coating systems. 2009.

[33] X. Q. Cao, R. Vassen, D. Stöver. Ceramic materials for thermal barrier coatings. *Journal of the European Ceramic Society*, 24(1):1–10, 2004.

[34] J. R. VanValzah, H. E. Eaton. Cooling rate effects on the tetragonal to monoclinic phase transformation in aged plasma-sprayed yttria partially stabilized zirconia. *Surface and coatings technology*, 46(3):289–300, 1991.

[35] J. Kaspar and O. Ambroz. Plasma spray coatings as thermal barriers based on zirconium oxide with yttrium oxide. In *The 1st Plasma-technik-symposium*, pages 155–166, 1988.

[36] T. Troczynski, Q. Yang, G. John. Post-deposition treatment of zirconia thermal barrier coatings using sol-gel alumina. *Journal of thermal spray technology*, 8(2):229–234, 1999.

[37] R. A. Miller, W. J. Brindley, J. G. Goedjen, R. Tiwari, D. Mess. The effect of silica on the cyclic life of a zirconia-yttria thermal barrier coating. In *1994 Thermal spray industrial applications: Proceedings*. 1994.

[38] P. Ramaswamy, S. Seetharamu, K. J. Rao, K. B. R. Varma. Thermal shock characteristics of plasma sprayed mullite coatings. *Journal of thermal spray technology*, 7(4):497–504, 1998.

[39] L. Wang, D. C. Li, J. S. Yang, F. Shao, X. H. Zhong, H. Y. Zhao, K. Yang, S. Y. Tao, Y. Wang. Modeling of thermal properties and failure of thermal barrier coatings with the use of finite element methods: a review. *Journal of the European Ceramic Society*, 36(6):1313–1331, 2016.

[40] X. L. Fan, R. Xu, W. X. Zhang, T. J. Wang. Effect of periodic surface cracks on the interfacial fracture of thermal barrier coating system. *Applied Surface Science*, 258(24):9816–9823, 2012.

[41] C. V. Di Leo, J. Luk-Cyr, H. Liu, K. Loeffel, K. Al-Athel, L. Anand. A new methodology for characterizing traction-separation relations for interfacial delamination of thermal barrier coatings. *Acta Materialia*, 71:306–318, 2014.

[42] W. X. Zhang, X. L. Fan, T. J. Wang. The surface cracking behavior in air plasma sprayed thermal barrier coating system incorporating interface roughness effect. *Applied Surface Science*, 258(2):811–817, 2011.

[43] X. S. Yang, J. Wan, C. Y. Dai, Y. Zhang, W. G. Mao, Y. C. Zhou, C. Lu. Finite element analysis of crack propagation and fracture mechanical properties

of freestanding 8 wt.% y2o3–zro2 coatings. *Surface and Coatings Technology*, 223:87–91, 2013.

[44] T. J. Liszka, C. A. M. Duarte, and W. W. Tworzydlo. Hp-meshless cloud method. *Computer Methods in Applied Mechanics and Engineering*, 139(1-4):263–288, 1996.

[45] J. M. Melenk and I. Babuška. The partition of unity finite element method: basic theory and applications. *Computer methods in applied mechanics and engineering*, 139(1-4):289–314, 1996.

[46] T. Belytschko and T. Black. Elastic crack growth in finite elements with minimal remeshing. *International journal for numerical methods in engineering*, 45(5):601–620, 1999.

[47] T. Belytschko, J. E. Dolbow, N. Moës. A finite element method for crack growth without remeshing. *International journal for numerical methods in engineering*, 46(1):131–150, 1999.

[48] J. E. Dolbow. An extended finite element method with discontinuous enrichment for applied mechanics. 2000.

[49] T. Belytschko, J. E. Dolbow, N. Moës. Discontinuous enrichment in finite elements with a partition of unity method. *Finite elements in analysis and design*, 36(3-4):235–260, 2000.

[50] B. Moran, T. Belytschko, N. Sukumar, N. Moës. Extended finite element method for three-dimensional crack modelling. *International journal for numerical methods in engineering*, 48(11):1549–1570, 2000.

[51] S. Usui, C. Parimi, T. Belytschko, N. Moës. Arbitrary discontinuities in finite elements. *International Journal for Numerical Methods in Engineering*, 50(4):993–1013, 2001.

[52] S. E. Benzley. Representation of singularities with isoparametric finite elements. *International Journal for Numerical Methods in Engineering*, 8(3):537–545, 1974.

[53] A. Yazid, N. Abdelkader, H. Abdelmadjid. A state-of-the-art review of the x-fem for computational fracture mechanics. *Applied Mathematical Modelling*, 33(12):4269–4282, 2009.

[54] S. Mohammadi. *Extended finite element method: for fracture analysis of structures*. John Wiley & Sons, 2008.

[55] J. M. Melenk and I. Babuška. The partition of unity finite element method: basic theory and applications. *Computer methods in applied mechanics and engineering*, 139(1-4):289–314, 1996.

[56] T. Strouboulis, K. Copps, I. Babuška. The generalized finite element method. *Computer methods in applied mechanics and engineering*, 190(32-33):4081–4193, 2001.

[57] M. Fleming, Y. A. Chu, B. Moran, T. Belytschko. Enriched element-free galerkin methods for crack tip fields. *International journal for numerical methods in engineering*, 40(8):1483–1504, 1997.

[58] T. Belytschko, T. Black. Elastic crack growth in finite elements with minimal remeshing. *International journal for numerical methods in engineering*, 45(5):601–620, 1999.

[59] N. Moës, J. E. Dolbow, T. Belytschko. A finite element method for crack growth without remeshing. *International journal for numerical methods in engineering*, 46(1):131–150, 1999.

[60] G. Alfano, M. A. Crisfield. Finite element interface models for the delamination analysis of laminated composites: mechanical and computational issues. *International journal for numerical methods in engineering*, 50(7):1701–1736, 2001.

[61] G. I. Barenblatt. The mathematical theory of equilibrium cracks in brittle fracture. In *Advances in applied mechanics*, volume 7, pages 55–129. Elsevier, 1962.

[62] D. C. Noorman. Cohesive zone modelling in adhesively bonded joints: Analysis on crack propagation in adhe-sives and adherends. 2014.

[63] A. Hansbo and P. Hansbo. A finite element method for the simulation of strong and weak discontinuities in solid mechanics. *Computer methods in applied mechanics and engineering*, 193(33-35):3523–3540, 2004.

[64] J. H. Song, P. M. A. Areias, T. Belytschko. A method for dynamic crack and shear band propagation with phantom nodes. *International Journal for Numerical Methods in Engineering*, 67(6):868–893, 2006.

[65] S. Osher, J. A. Sethian. Fronts propagating with curvature-dependent speed: algorithms based on hamilton-jacobi formulations. *Journal of computational physics*, 79(1):12–49, 1988.

[66] D. Adalsteinsson, J. A. Sethian. A fast level set method for propagating interfaces. *Journal of computational physics*, 118(2):269–277, 1995.

[67] J. Lie, M. Lysaker, X. C. Tai. A binary level set model and some applications to mumford-shah image segmentation. *IEEE transactions on image processing*, 15(5):1171–1181, 2006.

[68] Matthew Pais. ABAQUS XFEM, 2009.

[69] B. Ekici. Effects of residual stress patterns on tbc systems. *Surface engineering*, 20(1):37–42, 2004.

[70] Q. I. Hong yu, L. Zhou, X. Yang. Measurement of young's modulus and poisson's ratio of thermal barrier coatings. *Chinese Journal of Aeronautics*, 18(2):180–184, 2005.

[71] J. Kondoh, H. Shiota, K. Kawachi, T. Nakatani. Yttria concentration dependence of tensile strength in yttria-stabilized zirconia. *Journal of alloys and compounds*, 365(1-2):253–258, 2004.

[72] G. Moskal. The porosity assessment of thermal barrier coatings obtained by aps method. *Journal of Achievements in Materials and Manufacturing Engineering*, 20(1-2):483–486, 2007.

[73] Ferdinand P. Beer, E. Russell Johnston, John T. DeWolf, and David F. Mazurek. *Mechanics of materials*. McGraw-Hill Education, 4 edition, 2012.

[74] I. B. Saad. Selecting material parameters in abaqus for cohesive elements defined in terms of traction-separation. *Dassault Systemes*.

[75] A. Turon, C. G. Davila, P. P. Camanho, J. Costa. An engineering solution for mesh size effects in the simulation of delamination using cohesive zone models. *Engineering fracture mechanics*, 74(10):1665–1682, 2007.

[76] G. Ghosh, C. Annavarapu, R.Duddu. A stabilized finite element formulation remedying traction oscillations in cohesive interface elements. In *Proceedings of the American Society for Composites—Thirty-third Technical Conference*, 2018.

[77] Co-simulation with xfem technology evaluates safety of hand grenade drop. *SIMULIA Realistic Simulation News*, page 6–7, Sep 2011.

[78] H. W. Wang, H. W. Ji, Y. Sun, H. Miao. Discussion on convergence issues in abaqus/standard while carrying out damage and fracture analysis. In *Advanced Materials Research*, volume 189, pages 2247–2250. Trans Tech Publ, 2011.